Universiteit van Amsterdam

Vrije Universiteit Amsterdam

MSc Physics and Astronomy

Gravitation, Astro-, and Particle Physics

Master Thesis

Simultaneous SMEFT interpretation of the signal and backgrounds in the $VH, H\rightarrow b\bar{b}$ analysis and ATLAS DSS during the start of LHC Run 3

Florian Haslbeck
13280368

July 2022
60 ECTS
September 2021 - July 2022

Examiner:
Dr. Tristan du Pree

Second examiner:
Dr. Flavia de Almeida Dias

Supervisor:
Dr. Geoffrey Gilles

Nikhef

National Institute for Subatomic Physics

Abstract

The differential cross-section measurement of associated Higgs boson production decaying to a pair of b-quarks ($VH, H \to b\bar{b}$) is sensitive to deviations with respect to the Standard Model (SM) predictions that can be interpreted as the effect of new physics which may exist beyond the LHC energy scale. This thesis presents for the first time a SM effective field theory (SMEFT) interpretation of the measurement that consistently considers the effective modifications to both the VH signal and two main backgrounds, diboson and V+heavy flavour jet production. Dimension-6 Wilson coefficients, to which the analysis was not sensitive before, are constrained significantly better by the novel combined interpretation. Furthermore, the thesis demonstrates that the new approach does not alter the constraints for coefficients to which the signal interpretation is particularly sensitive to. In addition, two examples of contributions to the ATLAS Detector Safety System during the recommissioning campaign for LHC Run 3 to record more collisions for unprecedented SM precision tests are described, namely the detector safety during the ATLAS beam pipe bake-out and the new control room ventilation panel.

Contents

1 Introduction

The most accurate description of matter to date is the Standard Model (SM) which describes matter to be composed of interacting elementary particles. Its predictions have been thoroughly tested experimentally and provide accurate descriptions for three out of the four known interactions, also referred to as forces, and the particles.

Despite the theory's remarkable descriptive precision for a wide range of measurements, it has become evident that the SM does not provide a comprehensive description of our universe. For example, about 80% of the universe's matter content consists of so called "dark matter", for which the SM is lacking a suitable description. Many theories exist that propose extensions to the model, suggesting the existence of new forces and particles in particular.

One powerful test of the SM is the ATLAS experiment at the Large Hadron Collider (LHC) at CERN. It records the collisions of protons which have been accelerated by the LHC to nearly the speed of light. To date, the LHC experiments have not found statistically significant signs of new physics and in absence of the discovery of new heavy particles, the possibility that new physics might only exist beyond the colliders energy reach must be considered seriously. Nevertheless, if any new particles interact with the SM particles, they will give rise to contributions that might be measured by ATLAS as subtle deviations with respect to the SM. In Spring 2022, the LHC restarted following an extensive refurbishment and maintenance period. This pause in operations was required to prepare the collider, the detectors and their infrastructure to record twice as much data as in prior runs at an even higher collision energy, allowing for even more precise tests of the SM.

The Higgs boson discovery is one recent success of the SM and thorough measurements are still needed to test its theoretically predicted properties. One interesting channel is the Higgs boson decay to a pair of b-quarks ($H\rightarrow b\bar{b}$) in association with a heavy vector boson (VH) because it allows the study of Higgs bosons that are produced with a very high transverse momentum, which are expected to be particularly sensitive to several new physics models.

One model-independent approach to interpret these measurements in terms of effective new couplings is the SM effective field theory (SMEFT), which interprets the SM as a low energy limit of a more complete theory at a higher energy scale. The existing SMEFT interpretations parameterise solely the measured signal to account for possible deviations caused by new physics, but ignore deviations to the background processes. However, the backgrounds can be modified by the same new physics that affect the signal, particularly in the $VH, H\rightarrow b\bar{b}$ channel. This thesis extends the SMEFT interpretation to include a parameterisation of two main backgrounds and investigates the impact on the constraints on effective couplings that the signal interpretation is sensitive to.

After introducing the theoretical foundations in Section 2 and the ATLAS detector in Section 3, the author's contributions to the ATLAS detector safety during the restart are described in Section 4, followed by a description of the novel combined SMEFT interpretation in Section 5. Section 6 summarises this thesis.

2 Theoretical foundations

2.1 The Standard Model

The Standard Model (SM) is a theoretical description of the hitherto known elementary particles and three out of the four known fundamental forces of our universe. The theory describes reality using fundamental quantum fields whose excitations are interpreted as particles that are categorised by their quantum numbers, for example their spin. Integer spin bosons mediate the forces between the fermions that have spin $= 1/2$. Fermions are divided into leptons and quarks and exist in three generations, for which the masses increase successively.

The interactions between the particles arise from the requirement of local gauge-invariance with respect to the non-Abelian gauge group SU(3)×SU(2)×U(1). The strong interaction is described to be mediated by eight massless gluons that couple to a quark's color charge. The electromagnetic force is mediated by one massless photon, that couples to the electromagnetic charge, the weak nuclear force by three massive vector bosons, two electrically charged W bosons and one neutral Z bosons, which couple to the weak isospin and the hypercharge. Bosons and fermions acquire their mass by their coupling to the Higgs field, whose excitation, the Higgs boson is the only scalar particle (spin $= 0$) of the theory and was the last predicted particle to be discovered by the ATLAS and CMS experiments at the LHC in 2012 [1, 2].

The SM is an incredible achievement of particle physics. It has been developed by decades of close collaborations of experimentalists, who discovered new particles, and theorists, who developed a comprehensive theoretical description and predicted new particles. Some of them, like the Higgs boson, were later discovered by experiments. However, despite the SM's accurate descriptions for many measurements, observational conundrums like the neutrino masses or dark matter and theoretical shortcomings, for example the lack of a theory of quantum gravity, suggest that the SM is incomplete and is not the final "theory of everything".

2.2 The Standard Model Effective Field Theory

To this day, the LHC and its experiments have revealed two important features of nature, first, the discovery of the Higgs boson that explains the particle masses and second, the apparent absence of additional elementary particles within the LHC's energy reach, which are for example motivated by super-symmetric theories. Numerous theories that try to extend the SM suggest new forces that manifest as heavy new particles. In the absence of resonances discovered at the LHC, they might, if present, be too heavy to be directly produced at the LHC. The Standard Model effective field theory (SMEFT) assumes that new physics at a scale Λ is nearly decoupled from the LHC energy scales $E \ll \Lambda$. Therefore, the SM is interpreted as a low-energy limit of a more fundamental theory at higher energy.

The SM Lagrangian describes the dynamics of the quantum fields. Together with the principle of least action, it is used to derive the equations of motion. Within the SMEFT framework, it is expanded systematically in dimensions of $(E, \nu)/\Lambda$, where ν is the vacuum expectation value of the Higgs field, without assuming any structure of the new physics:

$$\mathcal{L}_{\mathrm{SMEFT}} = \mathcal{L}_{\mathrm{SM}} + \sum_i \frac{c_i^{(5)}}{\Lambda_i}\mathcal{O}_i^{(5)} + \sum_i \frac{c_i^{(6)}}{\Lambda_i^2}\mathcal{O}_i^{(6)} + \sum_i \frac{c_i^{(7)}}{\Lambda_i^3}\mathcal{O}_i^{(7)} + \sum_i \frac{c_i^{(8)}}{\Lambda_i^4}\mathcal{O}_i^{(8)} + \dots \tag{1}$$

The effects of new physics are described by effective operators $\mathcal{O}_i^{(d)}$ of dimension d that are constructed from the SM fields and fulfill the same symmetry requirements as the SM and that are suppressed by Λ^{d-4} as the overall Lagrangian is of dimension 4. The effective coupling strength of each operator is expressed by the associated Wilson coefficient $c_i^{(d)}$, that can be constrained from data by probing the interactions with the SM fields. Measurements are only sensitive to the ratio (c_i/Λ_i), and the combination (c_i/Λ_i) is a priori unknown. For each operator an explicit scale Λ_i needs to be chosen, as the operators might describe new physics effects at different energy scales Λ_i. This thesis chooses a common suppression of $\Lambda = 1$ TeV.

Any minimal set of operators that allows for a general description of new physics is referred to as an operator basis. While the physics is basis-independent, the interpretation is not and some bases are better suited to interpret a measurement than others. Nonetheless, constraints on coefficients of one basis can be translated into constraints on coefficients in another basis. The number of minimal operators increases significantly with the considered mass dimensions, however, they are also suppressed by increasing powers of Λ. This thesis considers only dimension 6 operators taking some assumptions on the new physics into account:

dim = 5: These operators lead to neutrino masses that are measured to be very small. Hence, their energy scale Λ is expected to be far beyond LHC reach, and the operators are disregarded.

dim = 6: Given the limits measured for the proton decay, any operator introducing lepton and/or baryon number violation is expected to be strongly suppressed at the LHC and can thus be neglected. The remaining 2499 operators are reduced to 76 operators that are considered when assuming that new physics does not distinguish between three generations of the three fundamental quark and two lepton fields (global $U(3)^5$ flavour symmetry).

dim = 7: These operators are expected to be highly suppressed at the LHC as they violate lepton number conservation.

dim = 8: The dimension 8 operators are neglected because their contributions are suppressed by an additional Λ^2 with respect to dimension 6 operators.

The SMEFT approach is limited to probe new physics beyond a chosen energy scale Λ that couples to the SM fields including the SM Higgs field. Nonetheless, the approach is a powerful way to constrain the effects of new physics in a model independent way. The advantage of the approach is the combined interpretation of experimental data across measurements, and even across experiments at different colliders. The same Wilson coefficients can be simultaneously constrained from multiple processes. Thus far, existing analyses only consider modifications to the signal of the measurement and do not interpret the background in terms of effective couplings. However, some backgrounds are affected by the same operators as the signal. This thesis investigates for the first time the consistent interpretation of deviations both in the signal and background processes of the $VH, H \to b\bar{b}$ measurement to constrain a subset of dimension 6 Wilson coefficients.

2.3 Higgs boson production and decay modes at the LHC

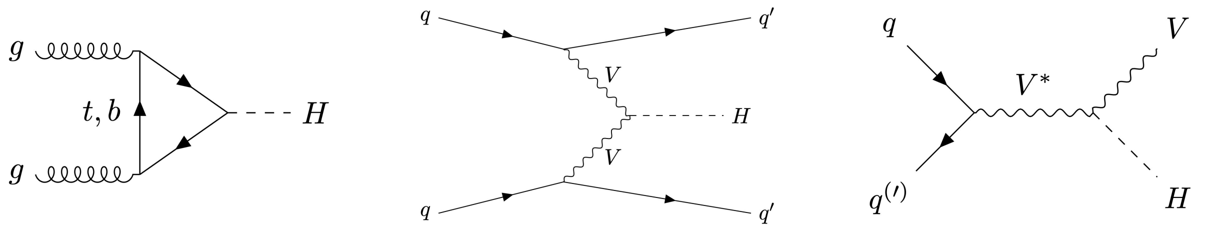

(a) Gluon-gluon fusion (ggF) (b) Vector boson fusion (VBF) (c) Associated production (VH)

Figure 2: Feynman diagrams for the three leading Higgs boson production channels at the LHC.

Figure 2 shows Feynman diagrams for the three leading Higgs boson production modes at the LHC. The proton momenta of the protons colliding at the LHC are carried by their constituents, the quarks and gluons. A single Higgs boson is most likely to be produced at a collision energy similar to the Higgs mass. At the LHC, with a centre of mass energy of several TeV, this is most likely from two massless gluons that fuse via an internal quark loop to a Higgs boson, referred to as gluon-gluon fusion (ggF). The second most likely production process is the radiation of two vector bosons from quarks that fuse to a Higgs boson, referred to as vector boson fusion (VBF). The third most dominant production channel is a Higgs boson that is radiated from an off-shell vector boson (VH), contributes to only a few percent of the total cross-section at $\sqrt{s} = 13\,\text{TeV}$. However, the leptonic decay of the vector boson provides a trigger signature and increases the signal over background ratio.

The Higgs bosons couplings is mass-dependent as consequently, consequently the branching fraction depends on the mass of the particles it decays into. The decay into two b-quarks ($H \to \bar{b}b$) is by far the most likely with a branching fraction of BR = 58% as it is the heaviest kinematically accessible final state. Decays to heavier states like two vector bosons only occur for off-shell vector bosons.

The Higgs boson has a very short lifetime and decays almost instantaneously. The total decay width has been calculated to be $\Gamma_H^{\text{total}} = 4.09 \pm 0.06\,\text{MeV}$ which is $\mathcal{O}(1000)$ smaller than its mass $m_H = 125.09\,\text{GeV}$ [3]. The narrow-width approximation states that off-shell contributions can be neglected and the production and decay calculated separately. The approximated cross-section σ is then given by the product of the on-shell production cross-section times the branching fraction:

$$\sigma(pp \to H \to X) \overset{\Gamma/m \to 0}{\approx} \sigma(pp \to H) \times \text{BR}(H \to X) = \sigma(pp \to H) \times \frac{\Gamma_H^X}{\Gamma_H^{\text{total}}}. \quad (2)$$

The same approximation is also used for the SMEFT approach. Considering only dimension 6 operators, the scatter amplitude $\mathcal{M}$ receives contributions from effective vertices that either modify SM vertices or introduce new ones, such as four-prong vertices. Furthermore, some operators redefine SM fields or change SM parameters. The production cross-section σ can then be approximated for the case of only one inserted SMEFT vertex each as

$$\sigma \propto |\mathcal{M}|^2 = |\mathcal{M}_{\text{SM}} + \sum_i \mathcal{M}_i^{(6)}|^2 \quad (3)$$

with the scatter amplitudes $\mathcal{M}_i^{(6)}$ introduced by the operators that are proportional to (c_i/Λ^2). The SMEFT cross-section σ_{SMEFT} is then given by the sum of the SM cross-section σ_{SM}, an interference term σ_{int} between the SM and the SMEFT scattering amplitudes that is suppressed by Λ^{-2} and a pure new physics cross-section term σ_{BSM} that is constructed only from the SMEFT amplitudes and is suppressed by Λ^{-4}:

$$\sigma_{\text{SMEFT}} = \sigma_{\text{SM}} + \sigma_{\text{int}} + \sigma_{\text{BSM}}. \tag{4}$$

For momentum-independent operators, the interference term σ_{int} is expected to be dominant with respect to σ_{BSM} given its smaller suppression. However, for operators that are sensitive to the energy transfer of the collision, this might not necessarily be the case if the energy transfer is not smaller than the new physics scale Λ. This behaviour can be estimated from the comparison of the contributions from σ_{int} and σ_{BSM}. However, the interpretation of σ_{BSM} is not trivial since it is missing other contributions that are also suppressed by Λ^{-4}. In particular, interference terms of SM amplitudes with dimension 6 operator amplitudes with two SMEFT-modified vertices as well as interference contributions from SM amplitudes with dimension 8 operator amplitudes with one SMEFT-modified vertex are missing.

2.4 Simplified Higgs Template Cross-Sections

The increasing LHC data set allows the measurement of differential cross-sections for the VH production channel. These measurements are especially interesting to constrain the effective coupling of SMEFT operators which introduce deviations that increase with the transferred momentum of the collision. The combinations of the obtained constraints require the measurements to be as detector-independent as possible. Therefore, theorists and experimentalists at different experiments agreed on exclusive phase space regions in which the effects are measured. The $VH, H{\to}b\bar{b}$ analyses use the Higgs Simplified Higgs Template Cross-Sections (STXS) framework [4] to measure the signal strength

$$\mu(pp{\to}V,H) = \frac{[\sigma(pp{\to}V,H)]_{\text{measured}}}{[\sigma(pp{\to}V,H)]_{\text{predicted}}} \tag{5}$$

in bins of the transverse momentum of the vector boson $p_T^V \in [75,150), [150,250), [250,400)$ and $[400,\infty)$ [GeV]. The lowest p_T^V bin is only measured for $ZH, H{\to}b\bar{b}$. The observable p_T^V is used as a proxy for p_T^H since the Higgs and the vector boson recoil against each other and the transverse momentum can be measured more precisely for the leptonic vector boson decay than for the hadronic Higgs boson decay. The bins are defined on generator-level p_T^V, and not on the reconstructed measurement of $p_T^{V,r}$ to be as experiment-independent as possible.

3 The ATLAS detector

The Large Hadron Collider (LHC) [6] at CERN is currently the most energetic particle accelerator and collider worldwide. It is designed to produce particles with masses up to the TeV scale, including the Higgs boson, and hence requires collisions at a high centre-of-mass energy. The 27 km-long circular machine is designed for proton-proton (pp) collisions at a peak centre-of-mass energy of 14 TeV. In addition, proton-lead-ion and lead-ion-lead-ion collisions are realised, too.

The ATLAS detector [5] is one of the two general-purpose LHC detectors. It is designed for a wide-ranging experimental program including the search for the - until 2012 - undiscovered Higgs boson, but also searches for light super-symmetric theories and other new physics phenomena. The detector consists of several sub-detectors that are placed in the cylindrical barrel region and inside two layered end-cap regions. The sub-detectors feature a forward-backward symmetry and provide an almost symmetric 4π solid angle coverage of the interaction point (IP). A cutaway illustration of ATLAS and its sub-detectors is shown in Figure 3.

The Figure furthermore shows the right-handed coordinate system with its origin at the IP which is used by the experiment. The axis x is defined by the direction from the IP to the center of the LHC ring, y is pointing upwards, z is parallel to the beam. In the transverse plane, cylindrical coordinates are used, with the radius r and the azimuthal angle ϕ around the z-axis. Quantities in this plane are denoted with the subscript $_T$. For pp collisions, the boost along the beam-axis is not known due to the unknown momentum fractions of the colliding partons. Therefore, the rapidity $y = \frac{1}{2}(\frac{E+p_z}{E-p_z})$ is used with E the particle's energy and p_z the momentum along the beam axis instead of the polar angle θ since differences in y are invariant under Lorentz boosts along the beam axis. In the ultra-relativistic limit ($m \approx 0$) the rapidity is approximated by the pseudo-rapidity $\eta = -\ln(\theta/2)$. The geometric distance between two particles is defined as $\Delta R = \sqrt{(\Delta\phi)^2 + (\Delta\eta)^2}$.

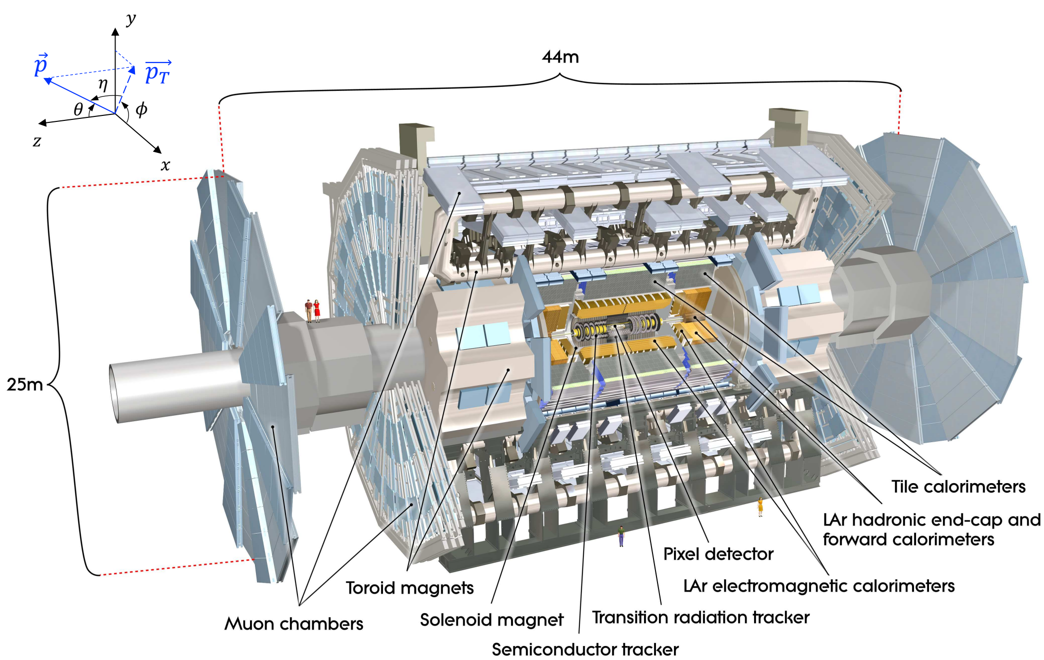

Figure 3: Cutaway illustration of the ATLAS detector. Modified from [5].

3.1 The sub-detectors

The ATLAS sub-detectors provide different measurements of the particles produced in the collisions. The Inner Detector (ID) is located inside a 2 T axial magnetic field generated by a thin superconducting solenoid and measures the trajectories and momenta of charged particles. The ID is enclosed by the electromagnetic and hadronic calorimeters that measure the energy of particles via electromagnetic or strong interactions. Lastly, the muon spectrometer (MS) is the outermost sub-detector and measures muon tracks and momenta and features an independent magnet system.

Inner Detector The ID measures the tracks of charged particles with a minimum transverse momentum p_T of 0.5 GeV with a resolution of $\frac{\sigma}{p_T} = 0.05\%\ p_T\ [\mathrm{GeV}] \oplus 1\%\ p_T$. Additionally, the sub-detector provides reconstruction of the primary, secondary and tertiary interaction vertex that originate from heavy-flavour hadron decay-chains, for example B hadrons. Its inner three layers consist of high-granularity silicon pixel detectors covering a pseudo-rapidity range $|\eta| < 2.5$. After Run 1 the Insertable B-Layer (IBL) [7] was added at R = 33 mm as the closest layer to the beampipe (R = 30 mm) to improve the impact parameter resolution in $(r - \phi)$ direction for low-p_T particles. Silicon microstrip detectors (SCT), arranged in four barrels and six disks, enclose the pixels for $|\eta| < 2.5$. Outside the SCT, there are straw-tube tracking detectors (TRT) covering $|\eta| < 2.0$. Their electron identification feature was lost during Run 1 due to irreparable gas leaks.

Calorimeters The two sampling calorimeter systems measure the particles' energy for $|\eta| < 4.0$. Additionally, given their segmentation, the systems provide directional information for the reconstruction of electrons, photons, jets and the missing transverse energy. Each system consists of alternating layers of active materials and passive absorbers, the total energy is then sampled from the active layer signals. The electromagnetic calorimeter (ECAL) measures the energy of particles that shower predominantly via the electromagnetic force. It is enclosed by the hadronic calorimeter (HCAL) which measures particles that shower predominantly via the strong force for $|\eta| < 4.9$. Particle showers are contained with minimal leakage into the Muon Spectrometer (MS). The ECAL high-granularity lead/liquid-argon (LAr) sampling calorimeters are divided in a barrel and two end-caps and cover $|\eta| < 3.2$ with an energy resolution of $\frac{\sigma_E}{E} = 10\%/\sqrt{E\,[\mathrm{GeV}]} \oplus 0.7\%$. The steel/scintillator-tile sampling HCAL detector architecture is adapted to the particle fluxes in each region, using steel/scintillator-tile in the barrel copper/LAr detector in the wheels and radiation harder copper/LAr and tungsten/LAr for the forward region that also provides electromagnetic calorimetry. The HCAL resolution decreases from $\frac{\sigma_E}{E} = 50\%/\sqrt{E\,[\mathrm{GeV}]} \oplus 3\%$ in the barrel to $\frac{\sigma_E}{E} = 100\%/\sqrt{E\,[\mathrm{GeV}]} \oplus 10\%$ in the forward region.

Muon spectrometer The MS measures muon momenta up to an energy of few TeV, and features dedicated triggering chambers. It is placed outermost since muons traverse all the other sub-detectors given their small ionisation loss and a short mean lifetime ($\tau \approx 2.2\,\mu$s). Most other particles are stopped at latest in the HCAL, thus, a MS track normally indicates a muon except for few neutrinos and very highly energetic showers that "punch through". The tracking ($|\eta| < 2.7$) and triggering ($|\eta| < 2.4$) chambers are immersed in a 4 T toroidal magnetic field which is generated by superconducting coils. The three layers of high-precision tracking chambers provide a relative momentum resolution of $\frac{\sigma}{p_T} = 10\%$ for a 1 TeV muon. Normally, the muon measurement is augmented with tracking information from the ID, which significantly improves the measurement for low-p_T muons. Separate sub-systems are adapted to the particle fluxes in the different regions. In the barrel, monitored drift tubes (MDTs) for precision measurements and resistive plate chambers (RPCs) for triggering are installed. In the forward region, the larger flux requires faster and radiation harder technologies. During the last long shutdown ("LS2") in preparation for the high-luminosity LHC, the small wheel featuring cathode strip chambers (CSCs) and thin triggering gap chamber (TGCs) were replaced by a new small wheel (NSW) [8] that features small-strip Thin Gap Chambers (sTGC) and micro-megas (MMG) chambers.

Luminosity measurement The Beam Condition Monitor (BCM) [9] at $z = 1.84\,\text{cm}$ supervises of the beam condition. Additionally, together with the LUCID detector [10] at $z = 17\,\text{m}$ and the Tile calorimeter, they provide luminosity measurements.

Trigger ATLAS uses a multi-level trigger and readout chain that selects interesting events for permanent storage to deal with the large event rate. The hardware-based Level-1 trigger identifies high-p_T-objects based on reduced calorimeter and muon information to form "Regions of interest" that are passed to the software-based High-Level trigger (HLT). The HLT further filters the events rusing full event information, which reduces the required storage rate from initial 40 MHz to 1.5 kHz. This corresponds to a data rate reduction from circa 60 TB/s to about 1.5 GB/s.

3.2 Services and infrastructure

ATLAS is the largest particle detector in the world and one of the most complex machines ever constructed. It is housed in an experimental cavern 85 m underground (UX15) that is connected to two service caverns (US15, USA15). An extensive and interdependent service infrastructure both underground and on the surface provides electricity and gas distribution, cryogenics for the magnet system and cooling to the detector and its subsystems. A comprehensive overview of the building naming convention is provided in Reference [11], surface building names start with an "S", underground building names with "U".

Electricity CERN is provided with electricity by the French power grid. In case of service disruptions a reduced supply is possible from the Swiss power network. The detector site "Point 1" is supplied with 66 kV which is transformed down to 18 kV supply on the surface. Secondary transformers convert this further down to 400 V and distribute the power to the equipment on the surface and underground. The regular power of critical elements is backed up by the Uninterruptible Power Supply (UPS) for 10 minutes, which is in some cases backed up by diesel generators and by the UPS safety network from the CERN Meyrin campus.

Water ATLAS uses the Swiss water network for the production of "Mixed" (15 °C) and "Chilled" (5 °C) water in electrical chillers on the surface (SUX1). The primary circuits are cooled via evaporation in cooling towers. The mixed and chilled water circuits are closed loops that are coupled to the heat exchangers of underground cooling stations in the service caverns.

Cooling The cooling stations and rack cooling circuits use closed water circuits which are coupled to the primary loops with heat exchangers. Critical racks feature a by-pass to tap-water cooling in case of a cooling circuit failure. The Tile and LAr calorimeter, the vacuum pumps, cable cooling and the MS use mono-phase cooling stations with water as the coolant. Two-phase evaporative cooling plants are used to cool the ID with C_3F_8 and the IBL with CO_2.

Cryogenics The cryogenic system cools the superconducting magnet systems. Liquid helium (4.5 K) is used for the cold mass of the magnets. The thermal shield is cooled down to about 60 K with gaseous helium.

Ventilation The environmental requirements inside the cavern are an ambient temperature of $25 \pm 3\,^{\circ}\mathrm{C}$ and a relative humidity in the range of 25 to 60%. Air conditioning units use the chilled water circuits to cool down selected surface buildings and the underground caverns. Cold air ($17\,^{\circ}\mathrm{C}$) enters the caverns at the level of the cavern floor. The warm air is extracted at the ceiling with about $24\,^{\circ}\mathrm{C}$ [12], cooled down and re-enters the cavern at the bottom. The ventilation system ensures that undesirable local temperature differences are avoided. In particular, the air temperature difference between the two sides of a muon chamber must stay below $3\,^{\circ}\mathrm{C}$ with a maximal air speed of 0.5 m/s to avoid inducing vibrations in the MDTs [13].

3.3 Safety and control systems

The safety of the personnel, the environment and the detector equipment and infrastructure are assured at any time, during data-taking, access and maintenance periods. The various subsystems require different level of supervision depending on their safety relevance for the system. The ATLAS alarm severity levels cover Level-1 and Level-2, corresponding to serious risk to the equipment, and Level-3, including dangers to persons, which automatically triggers an intervention by the CERN fire brigade.

The smoke detection system features environmental detection with sniffing pipes mounted close to the ceiling, and smoke detectors inside the racks. The sensors are connected to the smoke central (SFDIN) which is wired to the Detector Safety System (DSS). Flammable gas, oxygen deficiency and carbon-dioxide detectors are installed in the experimental and service cavern connected to the gas central (SGGAZ). The CERN Radiation and Environment Monitoring Unified Supervision (REMUS) [14] monitors the ambient dose equivalent [15], measures the induced radioactivity and the prompt radiation and issues alarms if critical limits were exceeded. Sensing wires on the ground provide large area leak monitoring in the cooling circuitry hardware that might result in infiltration causing hardware failure.

3.3.1 Detector Safety System

DSS [16] protects the experimental equipment and infrastructure. Upon detecting operational problems and abnormal and potentially dangerous situations, DSS takes predefined and hardwired "actions" to automatically bring the affected parts back into a safe state. DSS consists of an autonomous and redundant front-end and a supervising back-end. The topmost priority for its design is the high degree of availability and reliability. DSS is UPS powered.

The front-end features Programmable Logic Controllers (PLC) are configured to automatically take predefined protective actions whenever required. The PLCs organized by their supervised subsystems in seven Detector Safety Units (DSU) are connected by optical fibers. The back-end provides status displays and limited online reconfiguration capabilities of the PLCs. The DSUs operate on a positive safety logic based on a 24 V high signal, meaning that an event is defined as the flip from +24 V to 0 V. An alarm is triggered if the signal is kept low for a period longer than a minimum time required ("persistency", measured in seconds). This logic allows the trigger of an alarm even in the event of loss of power. The DSU outputs are connected with opto-couplers to the interlocks of the other systems which bring the system back into a safe state. The DSU outputs also operate on a positive safety logic to automatically interlock the equipment in the case of global power loss.

Expert system The complexity and extent of the ATLAS experiment and its infrastructure require in-depth knowledge in many different areas when planning an intervention or when reacting to unexpected situations. The experiment's knowledge base is mostly documented in the CERN's Engineering Data Management Service (EDMS) [18], however, the information is not easily accessible and comprehensible as it is often categorized with insufficient meta-data and in different formats. To facilitate and accelerate the gathering of expert knowledge and problem solving, the ATLAS Technical Coordination Expert System (ATCES) [19] has been developed to show interdependencies between systems and predict the impact of an intervention. This includes simulation tools that allow users to simulate the behaviour of the various systems for a given scenario, or tools that provides the user a list of potential causes for a list of DSS alarms. This allows the handling of error messages without the need of contacting a plethora of experts first.

To this day, the ATCES provides a visual description of ATLAS and its infrastructure including gas, cooling, cryogenics, ventilation, electricity distribution and detector safety systems, and their interaction with sub-detector systems and magnets to a multi-disciplinary team of experts. An example for a visual representation and simulation tool is given in Figure 4. It shows an abstract representation of the safety systems, including the switches a user can click to emulate the behaviour with the corresponding system switched off using the object-oriented and deterministic

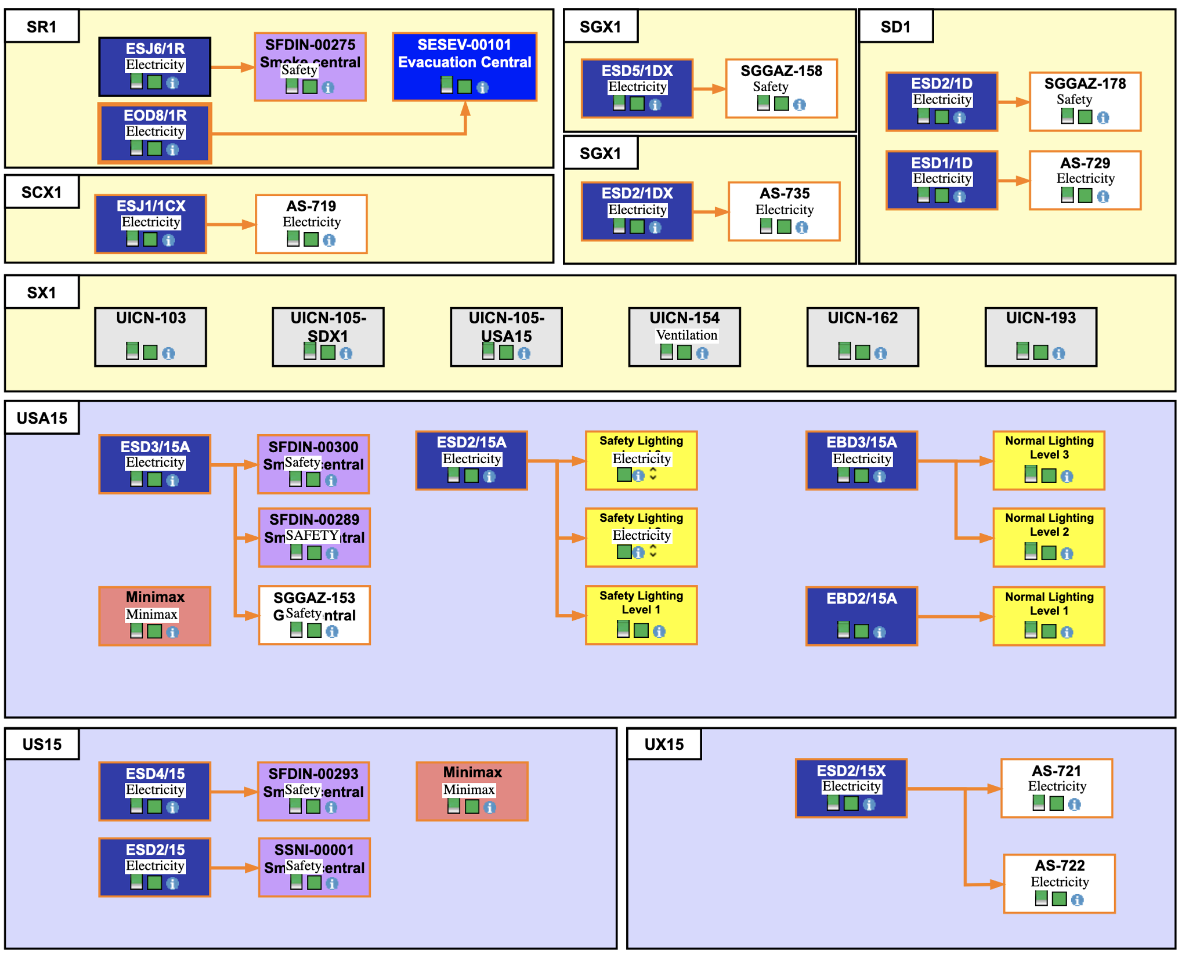

Figure 4: Visual representation of the safety systems provided by ATCES [17].

data-base and rules. The systems, each represented by a box, are grouped by their physical location, beige for surface buildings, shaded blue for underground locations. Dark blue represents electrical switchboards, grey gas systems, purple smoke central, salmon smoke detector detectors, yellow lighting, green cooling stations and white boxes illustrate racks and general systems like DSS Digital inputs ("DI") and actions ("O"). The borders and arrows indicate power in black (regular) and orange (UPS power). Red arrows indicate control. Each box features a switch on the left, that can be used interactively by the user to simulate a switch off of the system, the status is shown in the middle.

3.3.2 Detector Control System

Detector Control System (DCS) [20] provides supervision of the individual sub-detector systems and the general infrastructure to maintain its correct operational state. The system provides operator commands, reading, processing and archiving of the detector's operational parameters which in turn enables error detection and resolving. In addition, DCS is connected to external control systems such as the LHC controls and is synchronised with the data acquisition system. Critical states of the machine are associated with DCS alarms that are classified by severity.

4 DSS during the start of LHC Run 3

For the last three years, the LHC machine and its experiments underwent an extensive consolidation program and have been upgraded for the next run ("Run 3"), which will deliver higher luminosity at higher collision energy. For ATLAS, the main upgrades encompassed the installation of the NSW that replaces the radiation damaged small wheel, upgrades to the LAr calorimeter and the trigger and data acquisition system. The refurbished detector is expected to record more collisions than it did in two previous runs combined.

The following section provides two examples of safety interventions performed by the author to prepare ATLAS for Run 3. The stay at CERN was generously supported by the Volkert van der Willigen Grant for GRAPPA students. For the re-commissioning of the detector, the author conceived and implemented a new control room panel and standardised the communication with the ventilation operators and DSS. In addition, he participated in the risk-analysis for the safety-critical beam pipe evacuation procedure and developed mitigation measurements.

4.1 Detector safety for the 2022 beam pipe bake-out

The control of the vacuum during beam circulation is essential to minimize collisions with residual particles that otherwise degrade the beam and collision quality. Secondary electrons and ionised residual gas emitted in the collisions at high proton bunch intensities might release entrapped gas from the beam pipe walls. Close to the collision points, a vacuum of better than 10^{-11} mbar is required to achieve clean proton-proton collisions and the required 100 hour beam lifetime.

Beam pipe vacuum In most LHC beam pipe sections the cold bores (1.9 K) act as cryo pumps and remove residual contamination and are are shielded from synchrotron radiation, residual ions, and secondary electrons by beam screen shields (5-20 K). However, this system does not achieve the required vacuum quality in the warm interaction regions, for example around the ATLAS IP, where the pumping power of the six ion pumps is insufficient. Therefore, the pumps are combined with a non-evaporable getter coating (NEG) (2 μm sputtered coating of Ti-Zr-V) of about 90 % of the ATLAS interaction region [21, 22, 23]. NEG combines a very high residual particle pumping rate with a low ion desorption and secondary electron emission yield. To realize its high pumping rate, the coating is activated by heating it above 200 °C which releases the entrapped gases from the material ("bake-out"). The system must be clean before the activation to not immediately saturate again. The activation process cannot be repeated any number of times as the pumping properties deteriorate every bake-out cycle [24]. Therefore, the NEG activation procedure is only performed after a major vacuum loss to atmospheric pressure, and has been so far only performed at the start of Run 1 in 2008 and the start of Run 2 in 2014.

The ATLAS beam pipe Figure 6 shows a schematic diagram of side A of the beam pipe, a comprehensive reference is given in Reference [25]. The system is divided in seven elements connected in series that extend about 21 m in both directions before connecting to the LHC machine sector. The element name corresponds to the name of the surrounding system, for example VI for Vacuum-Inner Detector. The VA is enclosed by LAr end-cap, VT by the toroid end-cap, VJ by the forward shielding vacuum. Lastly, the TAS element is enclosed by the Front Quadrupole Absorbers. The VI chamber consists is of a beryllium beam pipe welded to a aluminium pipe at each end. The outer surface is permanently equipped with Kapton-foil bake-out heaters. The other elements comprises the stainless steel beam pipe.

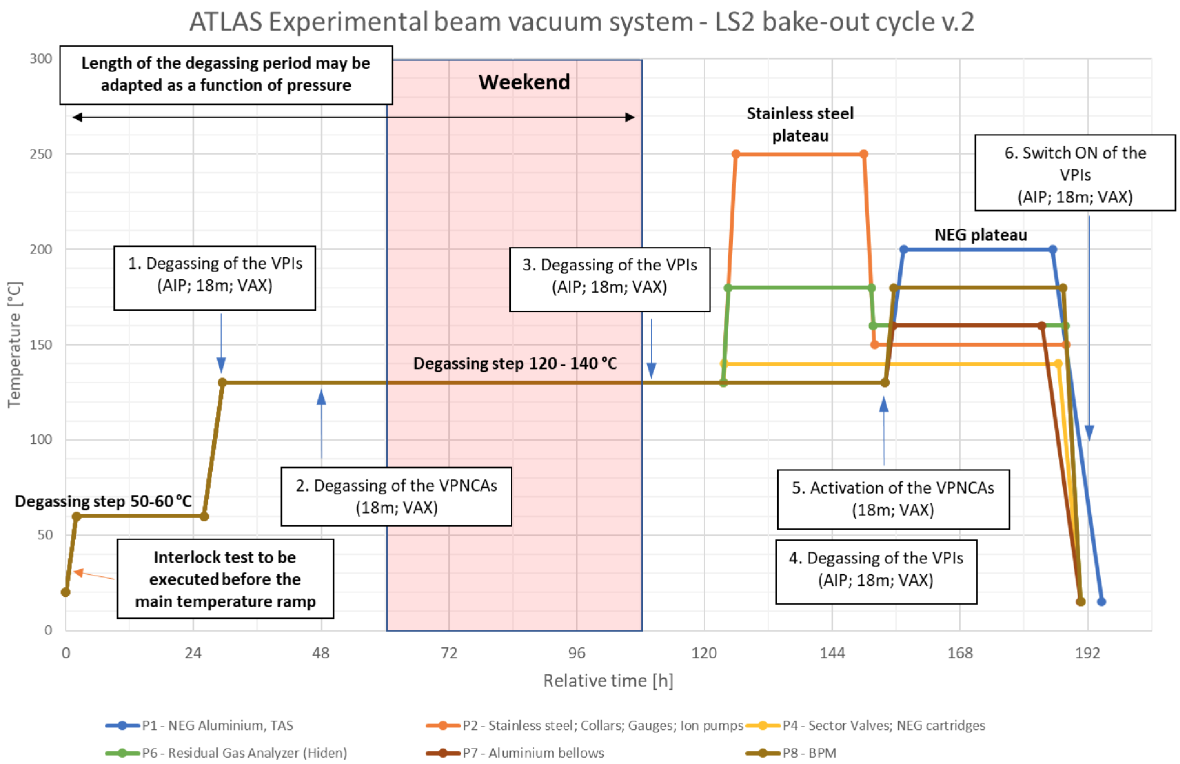

Figure 5: Schematic of the bake-out procedure showing the different temperature levels for the various components as a function of the relative time. Taken from [26].

Bake-out temperature profile The first degassing step is reached at 50-60 °C for about 24 hours for all systems. The first ramp to the low temperature step allows the verification of the functionality of the interlock signals which are discussed below. Next, the system is brought to a medium temperature plateau of 120-140 °C. Once this stage is reached, the procedure cannot be interlocked without risking severe damage to the beampipe as the interlocked heater then do not provide temperature control anymore. After three days on the plateau, the stainless steel parts are brought to 250 °C for 24 hours before they are cooled down to 150 °C for another day. The NEG is activated for one day at 200 °C after four days on the medium temperature plateau. In a last step, all components are brought back to room temperature in a controlled manner. Figure 5 shows a detailed temperature profile for the different beam pipe components.

Risk analysis *The following describes the risk analysis of the relevant components, infrastructure and interlock systems by the DSS team including the author in collaboration with the Technical Coordination and vacuum experts as well as experts for the sub-detectors affected by this intervention.*

The bake-out procedure is one of the single most critical interventions on the ATLAS machine, with the potential of severely damaging detector components like the IBL or the beam pipe. The main challenge is that during the bake-out safe temperature values must be maintained on all of the ATLAS detector elements, while still achieving the very high temperatures on the beam pipe sections required to activate the NEG coatings. Otherwise, severe damage or performance degradation to components mounted closed to the beam pipe can occur.

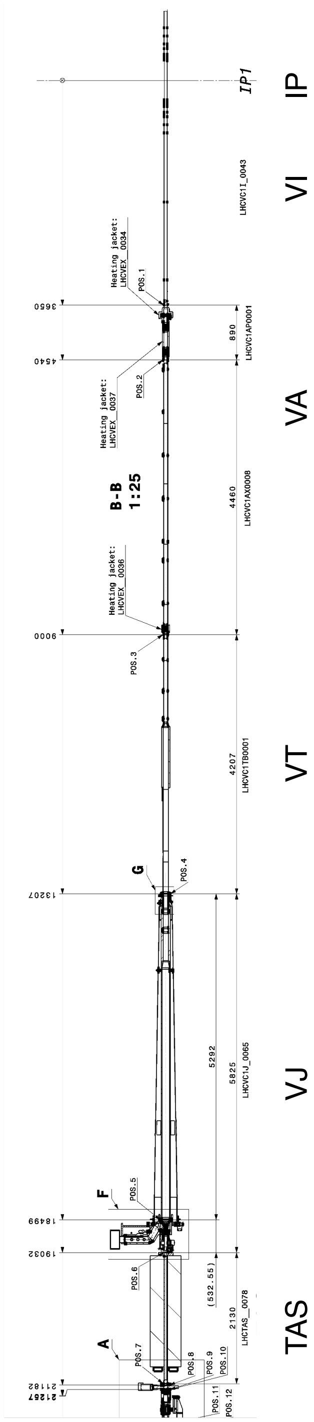

Figure 6: Schematic diagram of the side A beam pipe [27].

Several systems are identified as areas of concern during the preparation of the procedure:

- The element at highest risk is the beam pipe itself as the thermal gradient on the seals for the vacuum pipe flanges is limited to $\pm 20\,°$C/hour for warm-up and cool-down. If exceeded, the excess stress induced on the seals might get permanently damaged and the vacuum lost. Even after repairs and a repeated bake-out procedure, the seals might not be tight enough and cause a worse vacuum for the upcoming run. In any case, this scenario causes a significant time loss and delays Run 3. The thermal gradient limitation imposes a restriction on the temperatures for which an interlock will not cause permanent damage as the interlocked heaters will cool down without external control since all power has been cut. Therefore, the interlock signal and procedure is tested for very low temperatures at about 30 °C. For higher temperatures an interlock should be avoided as long as possible.

- The IBL is one of the components at highest risk given its distance of 3-4 mm away from the outer beam pipe. For temperatures at about 35 °C, the adhesive glue used to attach the modules to the staves starts dissolving. Tests with a mock-up showed that if a loss of cooling occurred in the high temperature ($> 200\,°$C) interval, the staves will reach 30 °C within 5 to 6 minutes, while the beam pipe would take more than 10 minutes before reaching safe temperatures. Therefore, a dedicated bake-out mode is defined for the IBL CO_2 cooling plants. Both plants are running in series and the operating temperature set to -20 °C, with the dew point adjusted to -30 °C accordingly. In case both plants fail, an additional backup is provided by the automatic IBL blow-off system, which flushes the IBL with bottled CO_2 via the same transfer line and provide cooling for up to four hours. The cooling experts concluded recovery time of the two plants exceeds two to three days and thus requiring a bake-out restart. As an additional safety measure, the IBL module interlock temperature is lowered from 30 °C to 10 °C.

- The maximum temperature allowed for the inner wall of the LAr calorimeter cryogenics at $z = 3$ m is 60 °C before permanent damage to the super-insulation inside the cryostat might occur. Therefore, it is cooled by one of two redundant chillers during the intervention. An additional cooling circuit is connected to the fire-brigade water circuit. However, the manual switch-over between the two circuits requires an early error detection.

- The LUCID detector at $z = 17\,\text{m}$ must not exceed $50\,°\text{C}$ to avoid damage to the PMTs. Damage to the services might occur for temperatures above $85\,°\text{C}$. LUCID is cooled primarily by compressed air, with two redundant cooling systems, chilled water, and chilled water from the Muon cooling loops. An extensive temperature supervision is provided by the 18 LUCID temperature sensors.

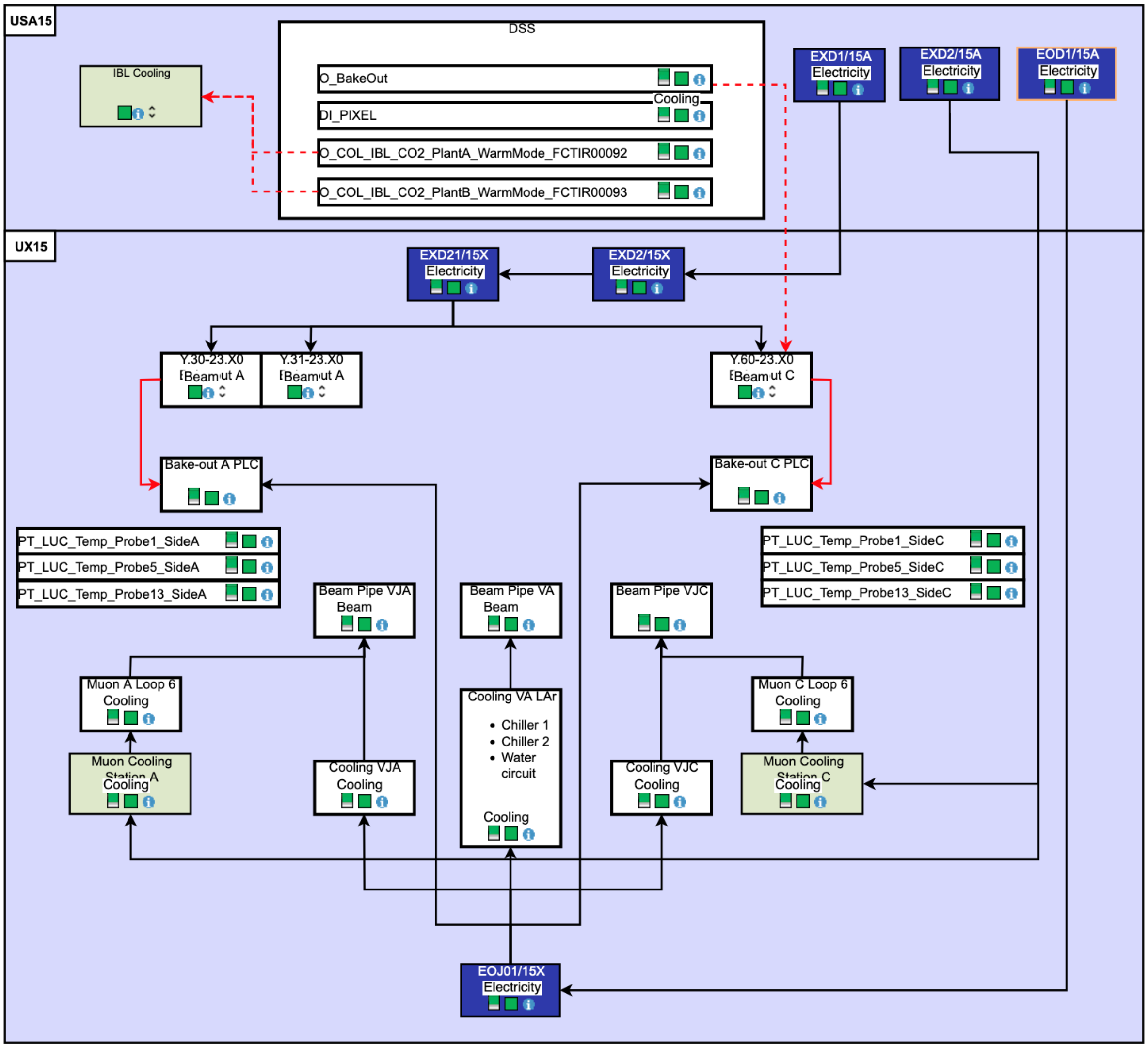

Figure 7: Schematic illustration of the bake-out infrastructure provided by ATCES [28]

DSS changes for the bake-out *The following paragraphs give an overview of the DSS mitigation measures conceived and implemented by the DSS team for the bake-out. A comprehensive engineering reference is provided in Reference [29].*

During the entire bake-out procedure, DSS assures the safety of the personnel, the environment and the detector equipment and infrastructure. The Alarm Action Matrix (AAM) [30] specifies the actions to return the detector to a safe state triggered by the DSS alarms and defines their delays. In consideration of the risks posed to the equipment, a dedicated bake-out AAM [17] is agreed upon the safety team, detector experts and the ATLAS management. Hereby, the foremost priority is the safety of the personnel while mitigating the risks outlined above. The default AAM, given in the Appendix in Table 5, considers inputs from cooling systems, environmental smoke detection, sniffer system, detector temperature monitoring, power distribution failure, flooding, and emergency actions. In a first step is is adapted to the infrastructure in place during the bake-out using the AAM from the 2014 bake-out, and is updated to represent the 2022 configuration. The AAM is studied extensively to identify direct and indirect impacts and interlocks to the bake-out procedure, particularly with the help of the ATCES description of detector. Figure 7 shows the visual representation of the bake-out infrastructure developed in ATCES. Once the risks are identified, mitigation measures are discussed with the relevant experts and the ATLAS technical management, in particular with the pixel and vacuum experts, and implemented.

The 2022 bake-out AAM has inputs from the following systems: Cooling stations (beam pipe chillers (VJA, VJC), IBL CO_2, rack cooling (USA15, US15)), environmental smoke detection (UX15, US15, USA15 CV room, USA15 Level 1 and 2 rack rooms, and USA15 Level 3), and the simultaneous smoke detection in two places in USA15, sniffer smoke detection (inner area, pixel PP2, EIL_SW), rack smoke detection (heater racks, pixel racks, and muon racks), temperature monitoring on LUCID side A and C, UPS failure of EOD2/15, EOD2/15A, ESS107/15, water leak detection under the IBL CO_2 cooling plant and the emergency stop buttons. Multiple entries have direct impact the bake-out such as the "red button" in the ATLAS control room. Moreover, several entries with indirect impact on the procedure are identified and considered, too.

In addition, any interventions impacting vital services is severely restricted during the most high-temperature period during which the detector is at the highest risk, as well as the access to the cavern by anyone not necessary for the bake-out. While this limits the time available to complete other interventions, for example the RPC gas leak repairs, the risk of (accidentally) triggered DSS alarms and consequently interlocks of the bake-out procedure and the potential consequences of such, outweigh the benefit of extra days for other interventions.

The majority of AAM changes address the risk of potential false alarms which have drastic consequences when occurring during the bake-out by temporarily deactivating their actions to prevent an bake-out interlock. The DSS alarms are kept operational to inform the operators of the potentially critical state. The improved bake-out matrix is given in Table 1. The AAM changes, their impact and their reasoning is described in depth in Reference [29]. A short overview is given below:

- Redefinition of the LUCID cooling alarm: The alarm trigger condition now considers also the possibility of a failure of the relevant muon cooling loop ("Muon loop 6") in addition to a failure of the entire muon cooling station which stops all Muon system cooling loops. The new logic is more reliable and a more accurate representation of the system, and is shown in Figure 7.

- DCS provides critical monitoring and control capabilities during the bake-out procedure. Therefore the actions interlocking the racks that host the DCS crates in case of smoke detection in the neighbouring rack are disabled. The racks still have rack-level smoke detection, thus the impact of this measure is small. Additionally, the rack containing the Pixel temperature monitor is backed up by UPS, the other equipment is turned off. The interlock to the normal power of racks hosting the IBL control racks is disabled to avoid loss of control for this system.

- The IBL cooling operates in a special bake-out mode as the loss of cooling power would be critical to the system. The warm mode is designed for detector commissioning and is not considered a safe operation mode. Hence, the DSS actions setting the cooling plants into the warm mode are disabled. Moreover, any actions associated to reaching the over-temperature threshold in the ID's Pixel B layer or Pixel disks are disabled to keep the cooling circuits running, since the IBL will act as a thermal shield to the pixel detector while the beam pipe cools down.

- Sniffer alarms indicate a smoke event which can be critical to the detector. Therefore, the associated actions usually interlock the rack in which the sniffer is mounted. Some alarms can interlock the bake-out, for example when the cooling stations or the bake-out heater racks (EXD203/15X) are affected. In the past, several false alarms were observed for the sniffer system that were potentially by dust absorbed by the system. These events were of short duration, hence the alarm persistency is increased from 1 s to 10 s. In the case of a real smoke event, there is additional detection provided by the environmental smoke detection for which the persistency is not changed. Furthermore, the sniffer alarms are still visible to the operators and allow a follow-up. Nevertheless, this measure gives a delayed response in case of a real smoke event which bears the risk of a potentially slower operator response and power down of the electronics causing the smoke. Applying similar reasoning, the actions associated with the sniffer alarms in the central trench underneath the detector are inhibited as a real fire event would be sensed by the additional smoke sensors in the experimental cavern.

- The detection of flammable gas leads to an immediate shutdown of the electrical components in the affected area. Normally, flammable gas is prohibited in the cavern, however it is sometimes used for maintenance during manual interventions. For the duration of the bake-out, such interventions are forbidden given the drastic consequences for the detector associated with the corresponding alarms. With no flammable gas present in the cavern the coincidence of two alarms is considered a false alarm. Thus, the actions of the coincidence of two or more Level-3 alarms of flammable gas alarms in the NSW sector are disabled as they interlock the IBL cooling.

- The chance of a significant flooding event at any given time in ATLAS is very small, yet, such an event has severe consequences for the detector (and so have the actions for the associated alarms). To avoid the actions of false flooding alarms, which have occurred in the past when excess or cleaning water was spilled on the sensors, the actions of the cavern flooding alarms are disabled for the duration of the bake-out. The alarms are kept as warning.

Before the start of the bake-out, the full bake-out signal chain is tested for systems which have not been tested since the last bake-out in 2014, namely the input to DSS, DSS alarms and their actions. The DSS team was on-call during the entire operation and at least one member of the DSS team was present during the bi-daily meetings to discuss the progress and the next steps while following the mandatory COVID-19 safety precautions. The bake-out procedure went as planned and the vacuum group confirmed the final vacuum reached to be better than the required 10^{-11} mbar. The recorded temperature trends of the beam pipe bake-out heaters is shown in Figure 31 in the Appendix. The official documentation by the Pixel experts and the vacuum group is in preparation and is not been released yet.

Bake-Out-New	O_COL_BeamPipe_VJA_CoolingSwitch	O_COL_BeamPipe_VJC_CoolingSwitch	O_COL_IBL_CO2_PlantA_WarmMode_FCTIR00092	O_COL_IBL_CO2_PlantA_WaterInterlock_FCK00135	O_COL_IBL_CO2_PlantB_WarmMode_FCTIR00093	O_COL_IBL_CO2_PlantB_WaterInterlock_FCK00136	O_COL_IBL_CO2_Vacuum_PumpInterlock_FCTIR0009	O_COL_IDE_PlantFCTIR00038_STOP	O_COL_IDE_PlantFCTIR00038_Standby	O_INF_BakeOut_Interlock_Y6023X0	O_INF_PIX_IBL_Power_Y2407A2	O_INF_PIX_Power_Y0414S2	O_INF_PIX_Power_Y1114A2	O_INF_PIX_Power_Y1314A2	O_INF_PIX_Power_Y1514A2	O_INF_Power_EXD203
AL_COL_BeamPipe_VA_ChillerFailure										0						
AL_COL_BeamPipe_VJA_ChillerFailure	0															
AL_COL_BeamPipe_VJA_CoolingNotRunning										0						
AL_COL_BeamPipe_VJC_ChillerFailure		0														
AL_COL_BeamPipe_VJC_CoolingNotRunning										0						
AL_COL_Cables_CoolingFailure																
AL_COL_IBL_CO2_CoolingNotReady										0						
AL_COL_IBL_CO2_CoolingNotRunning										0						
AL_COL_IBL_CO2_PlantA_NOTinBakeOutMode										0						
AL_COL_IBL_CO2_PlantB_NOTinBakeOutMode										0						
AL_Emergency_ATLAS_OFF									0	0		0		0		10
AL_INF_BakeOut_EmergencyStop										0						
AL_INF_Power_US15_EOD2_UPSFailure									0							
AL_INF_Power_US15_ESS107_UPSonBattery									0							
AL_INF_Power_USA15_EOD2_UPSFailure									0							
AL_INF_Power_USA15_UPSonBattery									0							
AL_INF_RackCoolingFailure_US15												600				
AL_INF_RackCoolingFailure_USA15														600		
AL_INF_Smoke_US15_2ofLevels0_1_3									0			300				
AL_INF_Smoke_US15_Level2_Ceiling									0			300				
AL_INF_Smoke_US15_Level2_Floor									0			300				
AL_INF_Smoke_USA15L1_CVRoom								0								
AL_INF_Smoke_USA15L1_RackRoomSideC									0							
AL_INF_Smoke_USA15L2_RackRoom									0					300		
AL_INF_Smoke_USA15L3_CVArea										0						
AL_INF_Smoke_USA15_2Areas								360	0	0				300		
AL_INF_Smoke_UX15							300		0	0						10
AL_INF_US15_Flooding																
AL_INF_USA15andUX15_Flooding																
AL_INF_WaterLeak_IBL_CO2Cooling_PlantA				0												
AL_INF_WaterLeak_IBL_CO2Cooling_PlantB						0										
AL_LUC_TempTooHigh_SideA										0						
AL_LUC_TempTooHigh_SideC										0						
AL_MAG_BT_VesselVacuumFailure									0							
AL_MAG_ECTA_VesselVacuumFailure									0							
AL_MAG_ECTC_VesselVacuumFailure									0							
AL_PIX_IBL_Temperature_Interlock										0						
AL_PIX_Temperature_Interlock																
AL_SN2_Smoke_InnerDetectorA									0	0						
AL_SN2_Smoke_InnerDetectorC									0	0						
AL_SN3_FG_EIL4_SW_2Alarms																
AL_SN3_Smoke_BWA_and_BWC									0	0						10
AL_SN3_Smoke_CentralTrench																
AL_SN3_Smoke_InnerArea_and_BWA									0	0						10
AL_SN3_Smoke_InnerArea_and_BWC									0	0						10
AL_SN3_Smoke_InnerArea_and_MuonBarrel									0	0						10
AL_SN3_Smoke_InnerDetector									0	0						
AL_SN3_Smoke_MUN_MuonBarrel_InnerArea									0							
AL_SN3_Smoke_MacroArea_BWA_2alarms									0	0						10
AL_SN3_Smoke_MacroArea_BWC_2alarms									0	0						10
AL_SN3_Smoke_MacroArea_InnerArea									0							
AL_SN3_Smoke_MacroArea_InnerArea_2alarms									0	0						10
AL_SN3_Smoke_MacroArea_MuonBarrel									0							
AL_SN3_Smoke_MacroArea_MuonBarrel_2alarms									0	0						10
AL_SN3_Smoke_MuonBarrel_and_BWA									0	0						10
AL_SN3_Smoke_MuonBarrel_and_BWC									0	0						10
AL_SN3_Smoke_PixelBoxes_PP2																
AL_Smoke_IDE_Y2721A2									0							
AL_Smoke_IDE_Y2821A1									0							
AL_Smoke_MUN_Y3723X0																10
AL_Smoke_MUN_Y3823X0																10
AL_Smoke_MUN_Y5023X0																10
AL_Smoke_MUN_Y5123X0																10
AL_Smoke_MUN_Y5823X0																10
AL_Smoke_PIX_Y0314S2																
AL_Smoke_PIX_Y0414S2												0				
AL_Smoke_PIX_Y1314A2														0		
AL_Smoke_PIX_Y1414A2																
AL_Smoke_PIX_Y1514A2																

Table 1: Improved bake-out AAM showing the alarms ("AL") and the associated action ("O"), with the delay in seconds.

4.2 Ventilation panel

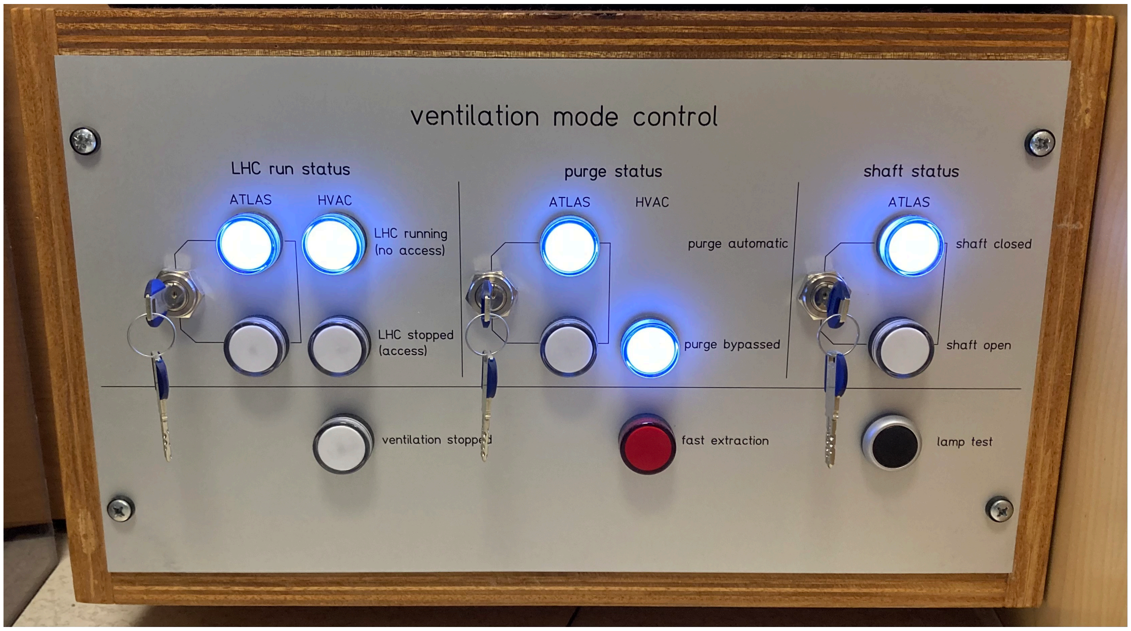

Figure 8: The new ventilation panel.

The Shift Leader in Matter of Safety (SLIMOS) is the main responsible in the ATLAS control room (ACR) for the safety organisation, foremost the safety of the personnel, and the safe operation of the detector. They monitor and handle the safety, status and alarms of the detector and its infrastructure, control the access, and coordinate interventions and emergencies on the experimental site. In addition to the DSS and DCS interfaces, a hardware panel is used for the manual interaction between a person and the DSS, such as the operation of the emergency ATLAS off button, the Material and Personal Access Devices (MAD, PAD) or the handling of patrols keys[1]. The SLIMOS mandate is defined in detail in Reference [11].

The mandate encompasses the assurance of the correct cavern ventilation mode. An incorrect ventilation mode might result in radiation poisoning of personnel entering the cavern or damage to the detector by incorrect depressurization of the cavern. ATLAS and CMS decided during Run 2 that their respective hardware panels should be extended by the possibility to change ventilation mode in a common standard and the reliability of the communication between the control room operators and the ventilation experts must be improved, in particular, a connection to the DSS was deemed essential and the communication via telephone was deemed insufficient.

Ventilation modes ATLAS features multiple ventilation modes:

- In run condition (*no access*), the shafts are closed and the experiment uses a closed loop ventilation system for the underground caverns. To limit the contamination in case of a radiation leak, the experimental cavern (UX15) is over-pressurised with 15 Pa with respect to the LHC machine tunnel. The service caverns (USA15, US15) are also over-pressurised with 15 Pa with respect to UX15 for the same reason.

[1] A patrol is the (final) inspection verifying that no person is in the interlocked areas before beam injection.

- In *access* mode, fresh air is circulated in the cavern and the shafts are open. Normally, to switch from the *no access* to the *access* mode, the over-pressure is filtered and released to the environment, and the cavern air is completely purged with fresh air before the personnel enters the cavern.
- For short term access, for example during a Technical Stop, the purge procedure can be *bypassed* to save time, if REMUS does not measure harmful radiation levels. The caverns are kept pressurized and the ventilation loops remain closed.
- The *fast extraction* mode mitigates the risk of asphyxiation due to a leak in the liquid argon volume. The mode is an automatic emergency procedure and is triggered by the oxygen deficiency sensors. It increases the extraction of the heavy gas in three trenches in the cavern floor from $5000\,\mathrm{m}^3/\mathrm{h}$ to $32000\,\mathrm{m}^3/\mathrm{h}$ [5, 31].

The following paragraphs describe the new communication system developed and assembled by the author, in particular the signals to be exchanged and the hardware implementation. The new system has been successfully installed, tested and it is now in operation for Run 3. A comprehensive engineering documentation is provided in Reference [32].

In preparation for Run 3, the communication between the SLIMOS and the ventilation (EN-CV) operators is standardised featuring a new hardware interface panel in the ATLAS control room (ACR). The SLIMOS requests are sent from the panel and appear directly on the supervision program of the EN-CV piquet, that then performs the necessary actions. In addition, both, the requested mode as well as the ventilation status are fed into DSS, which was missing before. The new communication standard does not remove the need for an operator intervention, but it increases the reliability of the system and enhances the safety of the system and DSS. A view of the new panel is presented in Figure 8. It contains three key switches to request mode changes, the requests are further indicated by LEDs. Additional LEDs indicate the mode the the machine is currently in. Furthermore, a button to test the functioning of the LEDs without triggering any action during the annual safety maintenance is included, too. The entire SLIMOS hardware panel is shown in the Appendix in Figure 34.

The new system comprises two new hardware parts, the panel located in the control room, and dedicated electronics for the signal distribution between ACR and EN-CV and the duplication to DSS, named Ventilation Copy Box (VCB). The latter is housed in a newly installed switchboard in SUX1. Figure 9 gives a schematic overview of the new system that shows the direction of the signals exchanged. The electronic circuits for the switch board and the ventilation panel are provided in the Appendix in Figure 32 and 33, respectively.

Operating the ventilation panel To request a ventilation mode, the SLIMOS turns the associated key into the desired position. The requested mode is visually confirmed by an LED, in addition, the key gives a haptic feedback with a “click”. Table 2 lists the request signals that can be issued by the SLIMOS including a short description and the DIs signal that is sent to the EN-CV. On the ACR and DSS side, all signals are active low, but the EN-CV system requires an active high logic for the purge bypass signal. The *shaft open* signal is not a ventilation mode request, but prevents the ventilation system from pressurizing the open cavern can cause damage.

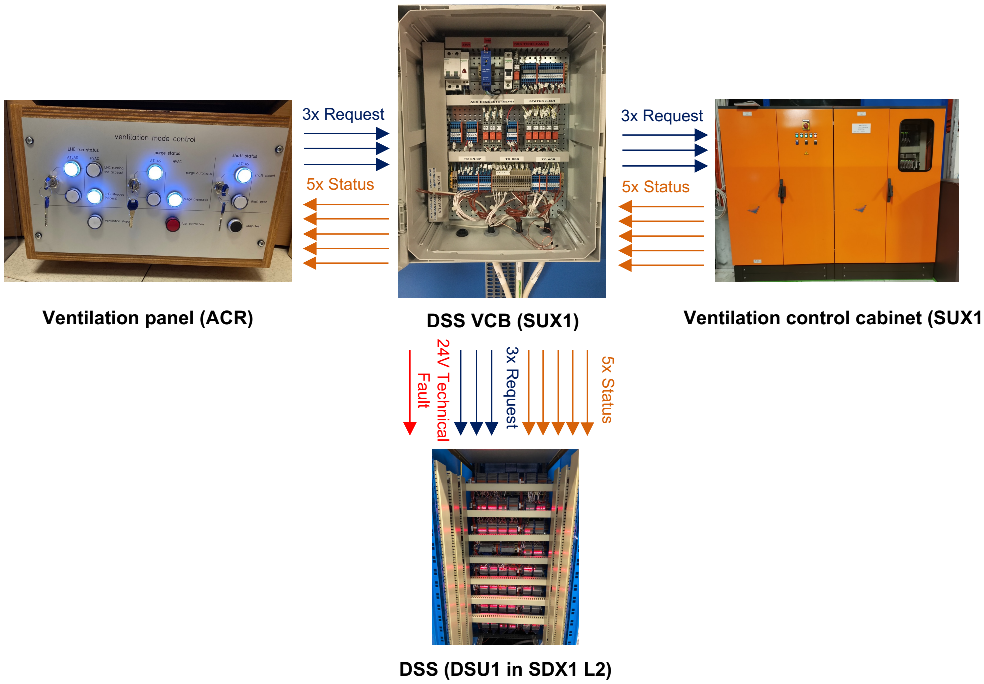

Figure 9: VCB System layout illustrating the exchanged signals as arrows.

The machine's ventilation mode status signal is issued from EN-CV and indicated by LEDs on the panel. Table 3 lists the EN-CV statuses and provides short descriptions. Furthermore, it shows the corresponding LED colour on the ventilation panel and the associated signal value of the EN-CV Digital Output (DO). Note, that there is no one-to-one correspondence between the requested and issued statuses. In particular, the EN-CV issues two separate signals to indicate the access condition. Furthermore, the *purge bypass* uses an active high signal logic contrary to the other signals which are active low. The states *Ventilation stop* and *Fast extraction* correspond to abnormal conditions, which are triggered by EN-CV. The *Fast extraction* mode corresponds to an emergency situation and is therefore indicated with a red LED. In addition to the panel LEDs. DSS Digital Inputs (DI) are used to make the mode available within DSS and trigger alarms.

Connection to DSS Each EN-CV status and ACR request has a corresponding DSS DI that is connected to the DSU1. Table 4 lists the DSS alarms, corresponding to an abnormal condition like a technical fault, a forced purge bypass, a stop of the ventilation or fast extraction. The alarms are triggered immediately upon fulfilling their alarm conditions reception of their DI-based conditions. One alarm indicates the incompatibility of simultaneous EN-CV statuses *Access* and *No access* for longer than five seconds. The request of this state is prevented by the key switch. A power loss to the VCB and the panel is signaled by the technical fault alarm which is used to mask the other alarms as they are triggered automatically by the active low logic.

Electronics Figure 10 displays the VCB signal handling schematics. Each system is grouped inside a black box, the cable functions are colour labeled. The systems are connected with shielded cables that have been routed by the cable team and reach from the ACR to the VCB (140m), from the VCB to the DSU (100m) and from the VCB to the EN-CV system (10m). The signal exchange, duplication and logic inversion must be very reliable and the three circuits, DSS, EN-CV and the

Signal name / opposite state	Description	EN-CV DI signal
Access /	Depressurise caverns and purge with fresh air.	low
No access	Pressurized caverns and closed loop ventilation.	high
Purge bypass /	Keep caverns pressurized and the ventilation closed loop ventilation during *access* for short interventions.	*high*
Automatic	Automatic cavern depressurisation and purge with fresh air for long-term *access*.	*low*
Shaft open	Prevent the pressurization of the caverns.	low
Shaft closed	Caverns are sealed and can be pressurized.	high

Table 2: ACR request signals that are issued with the key in the panel.

Signal name / opposite state	Description	LED colour	EN-CV DO signal
Access	Depressurize caverns. Purge with fresh air. Mutually exclusive with *No access*.	white	low
No access	Pressurized caverns. Closed loop circulation. Mutually exclusive with *Access*.	white	low
Purge bypass /	Keep cavern pressurized and closed loops during *access* for short interventions.	white	*high*
Automatic	Automatic cavern depressurisation and purge with fresh air for long-term *access*.	-	*low*
Ventilation stop	Ventilation is stopped.	white	low
Fast extraction	Emergency gas extraction in the trenches.	red	low

Table 3: EN-CV status signals issued as EN-CV DOs.

panel are electrically isolated with opto-couplers from another. The electronics of the VCB uses electromagnetic double pole single throw relays to match the different signal values required by the different systems, the signals are either high (24 VDC) or low (0 V). A separate relay is used for each ventilation status and each ACR request (with the above explained exception of *Access* / *No Access*). The request relays are controlled by a ACR key loop, which opens and closes the DSS and EN-CV loop. The status relays are controlled by the EN-CV loops and open and close the DSS and ACR LED loops. For simplified maintenance, the default status corresponds to the relay circuit being closed, which is indicated by the LED integrated in the relay. The 230 VAC power supply of the switch board is transformed down to 24 VDC which also powers the panel. Both, the 230 VAC and 24 VDC circuits are protected with circuit breakers. An additional relay is controlled by the internal 24 VDC supply and is connected to a DSS to issue a technical fault alarm when the power supply is faulty. The lamp test circuit is also powered from the switchboard and is connected to the LED test pins.

Alarm AL_VEN_{...}	DSS DI_VEN_{...}	Description
PurgeBypass	Purge_ACR	ACR operator requested purge bypass.
Stop	Stop_UIAN119	EN-CV stopped the ventilation.
FastExtraction	Extraction_UIAN119	EN-CV initiated fast extraction.
InvalidAccessConditions	Access_UIAN119 **and** NoAccess_UIAN119	The EN-CV is in an invalid access configuration.
VCB_TechnicalFault	TechnicalFault_VCB	Technical Fault. VCB and panel power loss

Table 4: DSS alarms and DI alarm condition. UIAN119 is part of the EN-CV system.

Assembly The system was assembled and installed before the beam commissioning tests in March 2022 and the DIs and alarms were created in the DSS AAM. A full system test with EN-CV was performed in April. The new system is in operation in ATLAS for Run 3. During the commissioning it was found that the combined inrush currents trips the DC circuit breaker. The breaker is now jumped and will be replaced during the next Technical Stop.Due to time constraints given by the Run 3 start up and the availability of electrical expert during the COVID-19 pandemic, the system has not yet been connected to UPS. This intervention is also planned for the next technical stop of ATLAS.

4.3 Conclusion on the contributions to the ATLAS detector safety

This section provided two examples of safety interventions performed that are necessary to recommission ATLAS for Run 3. The most critical intervention, the bake-out, has been performed successfully with no damage to the detector. The new SLIMOS hardware ventilation panel is installed in operation for Run 3.

In addition to the two examples given, the author assisted in the installation and commissioning of novel carbon-nanotube based water leak sensors [33], which will complement the current-in-use water sensing cables. The new paper-like sensor material extends the leak monitoring to complex two- and three-dimensional geometries. Moreover, the low cost material and readout units enable the monitoring with a finer granularity. For example, the sensor can be directly wrapped around cooling pipe joints inside a rack. Furthermore, the author contributed to enhancements to the ATCES, in particular to the most probable cause (MPC) tool [34]. The MPC tool provides the operator a set of possible causes that might have caused the current error even for incomplete detector information. Ongoing improvements to this tool include improved graph processing, using additional, non-DSS information and multivariate analysis techniques.

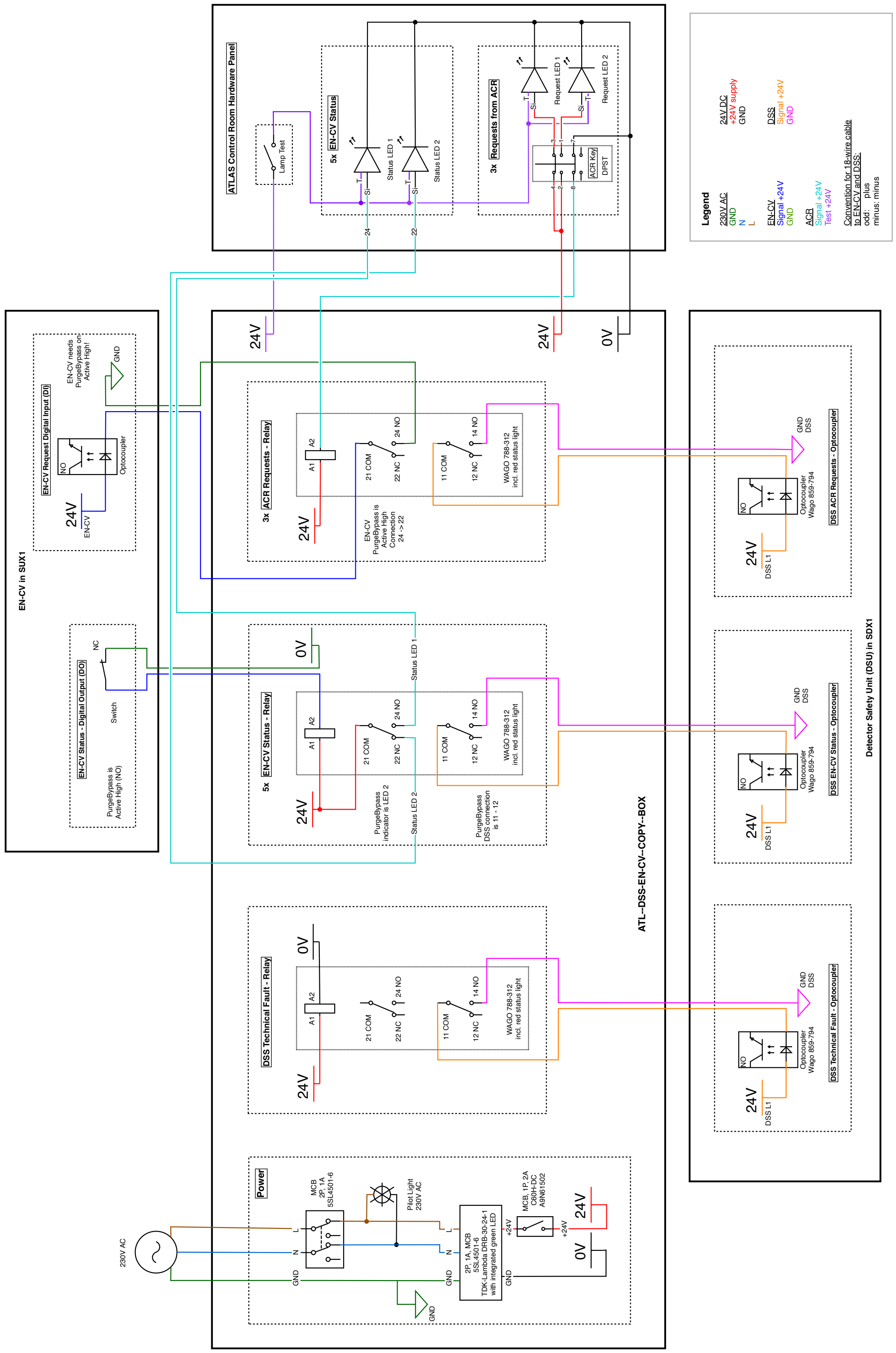

Figure 10: Schematic hardware and electronics diagram of the signal duplication and logic inversion for the EN-CV hardware panel. The diagram shows the schematic connections between the control room hardware panel, the ventilation control cabinet (EN-CV) located in SUX1, the duplication box (VCB) and the Detector Safety Unit in SDX1. NO / NC : Normally Open / Closed, COM : common, Si : Signal, T : Test, DPST : Double Pole Single Throw.

5 SMEFT interpretation of associated Higgs boson production

Some new physics models hypothesise that their effects, measured as deviations from the SM prediction, grow with the collision's momentum transfer. Consequently, differential cross-section measurements of the Higgs boson over a wide range of its transverse momentum p_T^H, especially for $p_T^H \gtrsim 400\,\text{GeV}$, might be particularly sensitive to these effects [35], and can be used to constrain effective couplings that are enhanced with increasing p_T^H. Thus far, the SMEFT interpretation of the $VH, H \to b\bar{b}$ measurement solely considers modifications to the signal process. This thesis features the first consistent SMEFT interpretation of the $VH, H \to b\bar{b}$ signal and two backgrounds to constrain dimension-6 Wilson coefficients.

5.1 The $VH, H \to b\bar{b}$ analysis

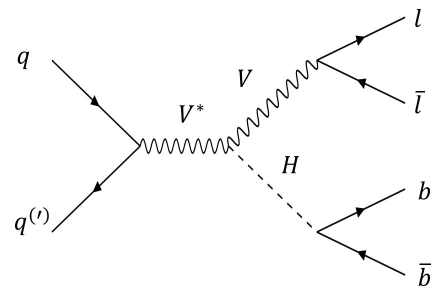

Figure 11: Feynman diagram of the $VH, H \to b\bar{b}$ signal .

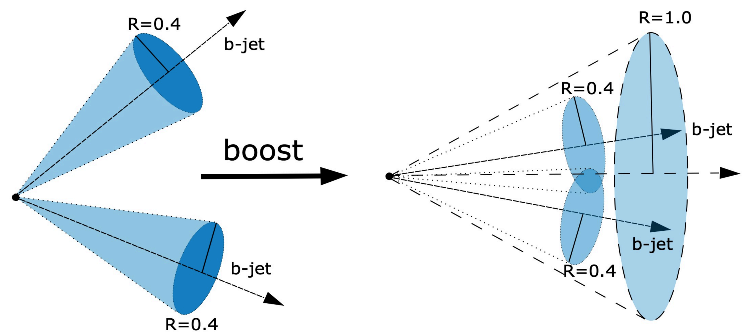

Figure 12: Sketch of the resolved (left) and boosted (right) $H \to b\bar{b}$ reconstruction. Taken from Reference [36].

While only contributing about 4% to the total Higgs boson production cross-section [37], the VH production has proven to be particularly interesting for studying high-p_T Higgs bosons. In particular, VH production allows to study the most prominent Higgs boson decay into a pair of b-quarks ($H \to b\bar{b}$). The b-quarks from the Higgs boson decay will further hadronise and form jets in the detector. This decay channel faces an enormous background from QCD multi-jet production for ggF and VBF production. In VH production, leptons from the vector boson decay are used for efficient triggering and to reduce these backgrounds. Figure 11 shows a leading order Feynman diagram for the $VH, H \to b\bar{b}$ signal with two quarks in the initial state, and the leptonic V decay. The analysis uses the vector boson transverse momentum p_T^V in lieu of p_T^H since the charged leptons (electrons and muons) can be measured more precisely than the b-jets.

The measurement employs two separate reconstruction techniques for the Higgs boson candidate shown in Figure 12, that are optimised for different Higgs boson transverse momenta. The resolved analysis strategy [38] reconstructs the Higgs boson decay by two separate jets with radius $\text{R} = 0.4$. The efficiency of this approach decreases significantly for high-p_T^H, as the distance between the two jets ΔR_{bb} decreases inversely with p_T^H ($\Delta R_{b,b} \sim 2m_H/p_T^H$) and the two b-jets cannot be reconstructed individually for high p_T^H. Thus, the boosted $VH, H \to b\bar{b}$ analysis [39] reconstructs the Higgs boson decay with one large jet ($\text{R} = 1.0$) that contains two smaller b-jets.

Several processes share a similar detector signature with the signal and need to be considered as backgrounds. Processes with the same final state are referred to as irreducible. Figure 13a

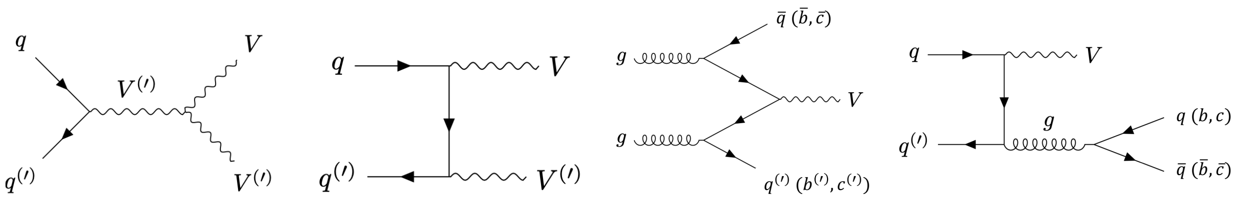

(a) Diboson (VZ) production. (b) V+heavy flavour (V+hf).

Figure 13: Two times leading order Feynman diagrams for VZ and V+hf production.

shows two times leading order Feynman diagrams for two examples, diboson production (VZ), for which the Z boson decays into a pair of b-quarks, and a vector boson produced in association with at least two heavy flavour jets (V+hf). The diboson process has a larger cross-section than the signal and a similar kinematic given that the Z boson is only slightly lighter than the Higgs boson. Consequently, this process can be used as a cross-check of the analysis strategy. The V+hf process has an even larger cross-section than VZ, however, the b-quarks originate from gluons. Irreducible backgrounds, like top-quark pair ($t\bar{t}$), single top and QCD multi-jet production, often have also significantly larger cross-sections than the signal. They pass the signal selection criteria because of detector inefficiencies like limited detector coverage or reconstruction inefficiencies. Figure 14 shows reconstructed large-R jet mass distribution representing the Higgs candidate mass from the boosted analysis and demonstrates the different backgrounds that are drawn in different colors. The differential $VH, H\to b\bar{b}$ cross-sections after background subtraction measured by the boosted, resolved and combined analysis are shown in Figure 15, illustrating the different measurement precision over the p_T^V range.

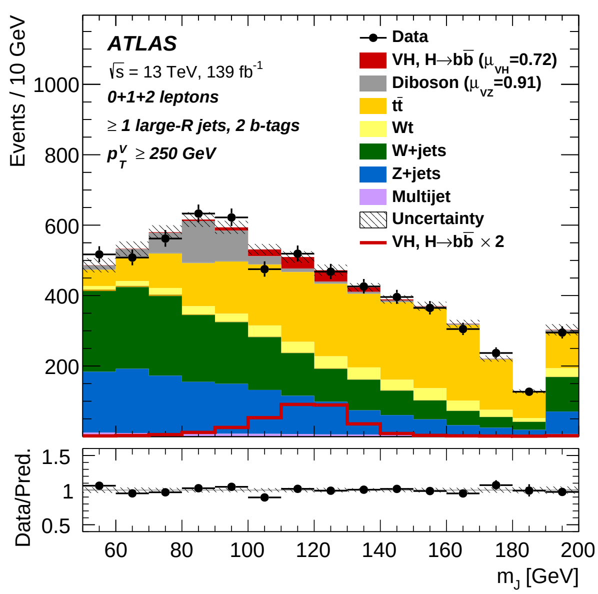

Figure 14: Higgs candidate mass distribution m_J measured by the boosted analysis [39].

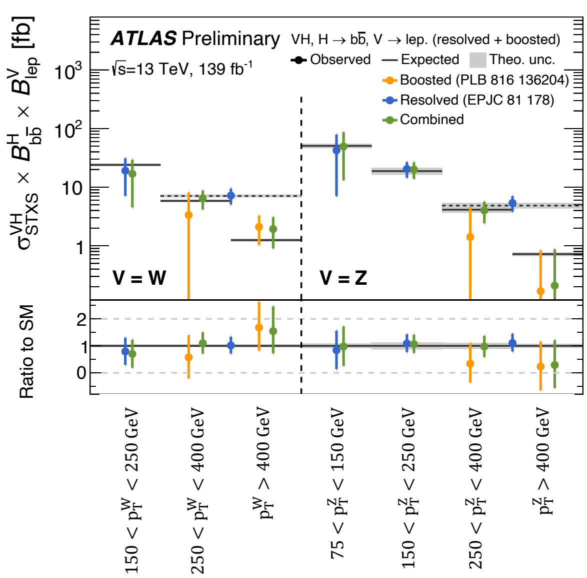

Figure 15: $VH, V\to$lep., $H\to b\bar{b}$ cross-sections measured by the boosted, resolved and combined analysis. Modified from [40].

5.2 SMEFT modifications to signal and background

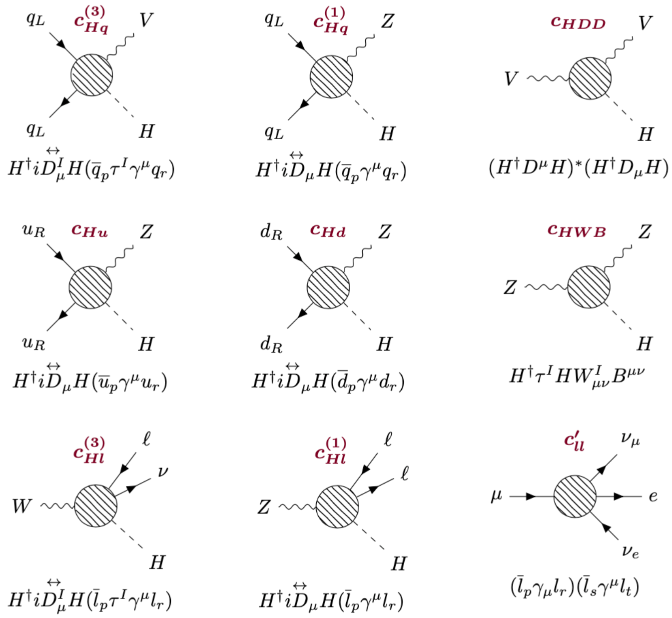

Operator	WH	ZH	WZ	ZZ	$Wb\bar{b}$	$Zb\bar{b}$
$\mathcal{O}_{Hq}^{(3)}$	✓	✓	✓	✓	✓	✓
$\mathcal{O}_{Hq}^{(1)}$		✓	✓	✓		✓
$\mathcal{O}_{Hu}$		✓	✓			✓
$\mathcal{O}_{Hd}$		✓	✓	✓		✓
$\mathcal{O}_{HWB}$		✓	✓	✓		✓
$\mathcal{O}'_{ll}$	✓	✓	✓	✓	✓	✓
$\mathcal{O}_{Hl}^{(3)}$	✓	✓	✓	✓	✓	✓
$\mathcal{O}_{HDD}$	✓	✓	✓	✓		✓
$\mathcal{O}_{Hl}^{(1)}$		✓	✓	✓		✓

Figure 16: Selected SMEFT operators and example vertices. Modified from Reference [36]. The table shows the processes affected by the operators by at least one vertex.

This thesis uses the Warsaw basis [41] of dimension-6 operators to interpret the measurements in the SMEFT framework. The study is restricted to operators affecting VH production and the two irreducible backgrounds, diboson VZ and V+heavy flavour jets. The impact on the constraint when considering the Higgs boson decay is shown to be negligible, and only the VH production is studied. For the two backgrounds, the SMEFT vertices affecting the vector boson decays are considered as well, including the hadronic Z boson decay. As elaborated in Section 2, the set of operators under consideration is greatly reduced by considering only baryon- and lepton-number conserving operators and imposing a global $U(3)^5$ flavour symmetry. Since p_T^V is an CP-even observable, only CP-even operators are considered. Lastly, only operators which affect the $pp \to V(\to \text{leptons})H$ by more than 1‰ for $c = 1$ are considered.

Figure 16 gives the operators' definition and shows one example SMEFT vertex for each operator. Additionally, the Table shows the processes affected by each operator, stressing the importance of a consistent interpretation to constrain the effective couplings. Generally, operators can modify three-prong vertices or introduce four-prong vertices, which are not part of the SM. Each operator has different effects on the cross-sections of the considered processes. The effects can, to some extend, be inferred from the operator structure. Reference [42] provides a detailed derivation. The operator effects either scale the cross-section constantly with $\sim v^2/\Lambda^2$, with ν the vacuum expectation value or scale in dependence of the energy transfer E of the process $\sim E^2/\Lambda^2$. For example, operators containing a covariant derivative D_μ might show a p_T-dependence due to the partial derivative acting on the wave function. The Higgs doublet $H \sim \frac{1}{\sqrt{2}}\binom{0}{v+h}$ contains the vacuum expectation value v and the Higgs field h. Thus, operators containing H can introduce a coupling to the Higgs boson, and can, given the term ν, modify vertices without the Higgs boson, too. For example, for ZH the operator $\mathcal{O}_{Hq}^{(3)}$ introduces a four-prong vertex with two quarks, a Z and a Higgs boson. Moreover, the modifications are momentum enhanced and the deviations increase with $(p_T^{V,t})^2$. At the same time, $\mathcal{O}_{Hq}^{(3)}$ modifies the quark-quark-Z boson coupling, for example in VH or ZZ production but also in the $Z\to b\bar{b}$ decay. The different effects are used to constrain the effective coupling across processes. Some operators distinguish between up and down-type quarks, for example $\mathcal{O}_{Hu}$ and $\mathcal{O}_{Hd}$. $\mathcal{O}_{Hd}$ affects $Z\to b\bar{b}$ in WZ. The process is not affected by $\mathcal{O}_{Hu}$ as the incoming quarks are of up and down-type. Others lead to re-definitions of fields and have effects constant over p_T^V. For example, c'_{ll} leads to a modification of the Fermi constant, hence affecting any weak decay, and can therefore be constrained from all considered processes.

5.3 Cross-section measurements

The boosted $VH, H\to b\bar{b}$ analysis measured the first differential cross-section measurement within the STXS framework exclusively for p_T^H>400 GeV. Given the higher detector resolution for leptonic signatures, the measurement considers the vector boson p_T^V, that recoils against the Higgs boson, in place of the large-R jet p_T reconstructing the hadronic Higgs boson decay.

5.3.1 Simultaneous STXS measurement of VH and VZ

The VZ process is used as cross-check for the $VH, H\to b\bar{b}$ analysis given their similar topologies and the Z boson peak that is used to test the analysis strategy. Since experimental sensitivity for ZZ is about twice as good as for ZH, the same analysis tools are used to measure the VZ cross-sections in the same generator level p_T^V bins as the boosted Higgs STXS framework. The measurement is described in Reference [43]. The VZ processes are distinguished in WZ and ZZ production. Since the same final state as the VH signal is measured, one Z boson is required to decay to a pair of b quarks, the other vector boson decays leptonically. The binned maximum likelihood fit of the m_J distribution extracts the corresponding eight cross-sections simultaneously in the same two p_T^V bins as the boosted $VH, H\to b\bar{b}$ measurement. The fit uses the full Run 2 dataset, at a center-of-mass energy of $\sqrt{s} = 13$ TeV, corresponding to an integrated luminosity of 139 fb^{-1}.

The fit result is shown in Figure 17. The signal strengths agree with the SM in all bins. The WH and WZ bins are measured with approximately equal precision. The ZZ bins are measured almost twice as well as the ZH bins. The diboson uncertainties range from 60-90% and originate equally from statistical and systematic uncertainties. The measurement reports correlations of 10-20% between the measured signal strengths given given the overlap of the Higgs and Z boson mass peak due to the limited detector resolution. The correlation between the VH bins does not change for the simultaneous fit with VZ. The VH bins are mostly uncorrelated, except for the high p_T^V bin, for which the hadronic τ decay from $W\to\tau\nu, H$ is mis-interpreted as a 0-lepton $Z\to\nu\nu, H$ event. The same effect is also observed for the high $p_T^{V,r}$ bins in WZ and ZZ. The highest correlation ($\approx 20\,\%$) is observed between ZZ and ZH for the two low p_T^V bins. A similar behaviour is seen for the high p_T^V bins.

5.3.2 Simultaneous Asimov measurement of VH, VZ and V+heavy flavour

Ultimately, the study aims study the impact on the constraints over the full p_T^V range. Yet, no STXS measurement of the combined boosted + resolved measurement including the backgrounds exists so far. Therefore, in a first step, an Asimov measurement over the full p_T^V range measured on reconstruction level is used as this thesis does not observe significant differences between constraints obtained from χ^2-fits to signal strengths measurements of VH+VZ binned at reconstructed $p_T^{V,r}$ instead of generator level p_T^V, when using in both cases the generator-level parametrisation. The

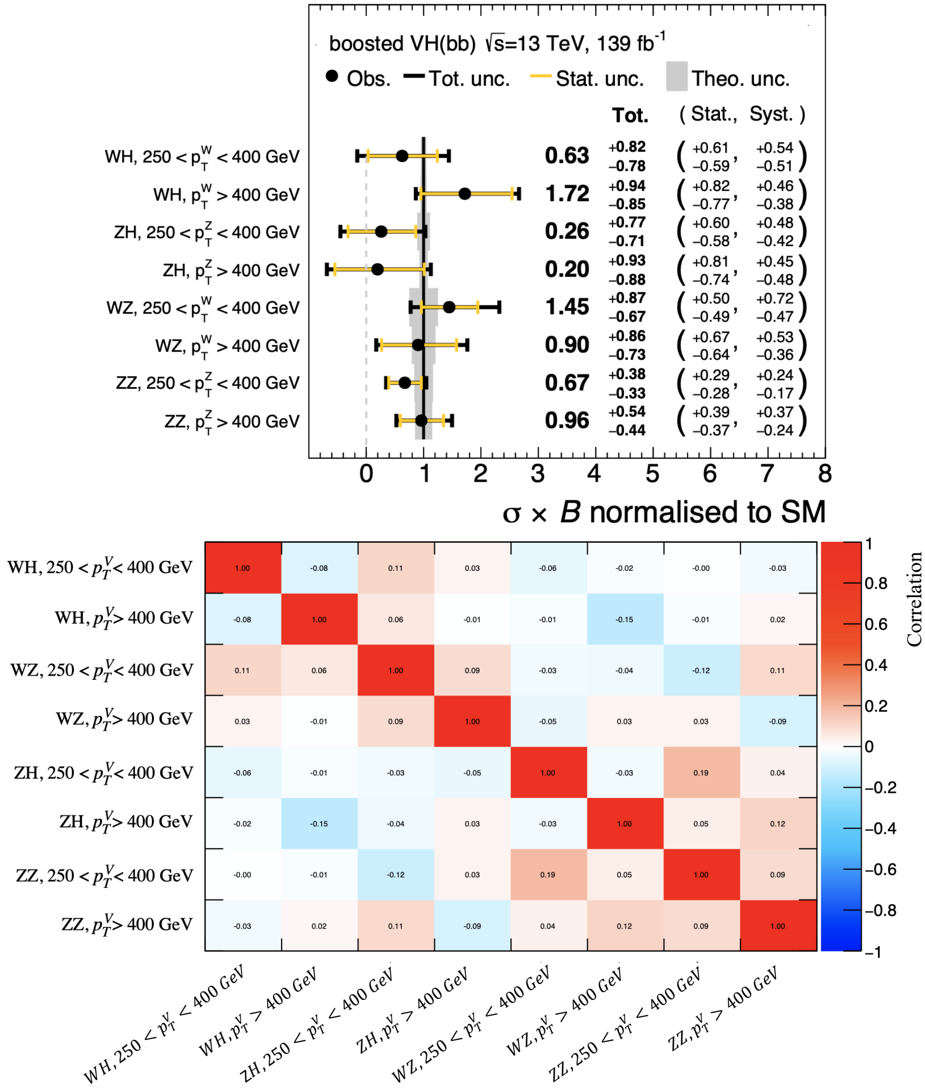

Figure 17: Simultaneously measured VH and VZ normalised cross-sections and their correlations in bins of p_T^V. Modified from Reference [43].

Asimov data simulates the SM and allows to obtain the expected confidence intervals (CI) under the SM hypothesis, the signal strengths are consequently all unity. In explicit, using a generator level parametrisation in both fits, the constraints differ $< 3\,\%$ for the linear parametrisation and $< 5\,\%$ when additionally considering quadratic terms. No separate parametrisation on reconstruction level is therefore obtained. The values are listed in the Appendix in Table 13 and shown in Figure 37. Therefore, a simultaneous signal strength measurement of VH, VZ and V+hf at reconstruction level over the full $p_T^{V,r}$ range is used. The bins mimic the STXS bins $p_T^{V,r} \in \{[75, 150), [150, 250), [250, 400), [400, \infty)\}$ [GeV], the lowest bin is measured for ZH, ZZ and Z+hf only. Figure 18 shows the expected CIs and the correlations based on Asimov data provided by the $VH, H \to b\bar{b}$ analysis team for the simultaneously measured signal strengths of VH, VZ and V+hf. The V+hf signal strengths are expected to be measured about ten times more precisely than the other processes and are correlated with the VH and VZ bins as the processes have the same final state.

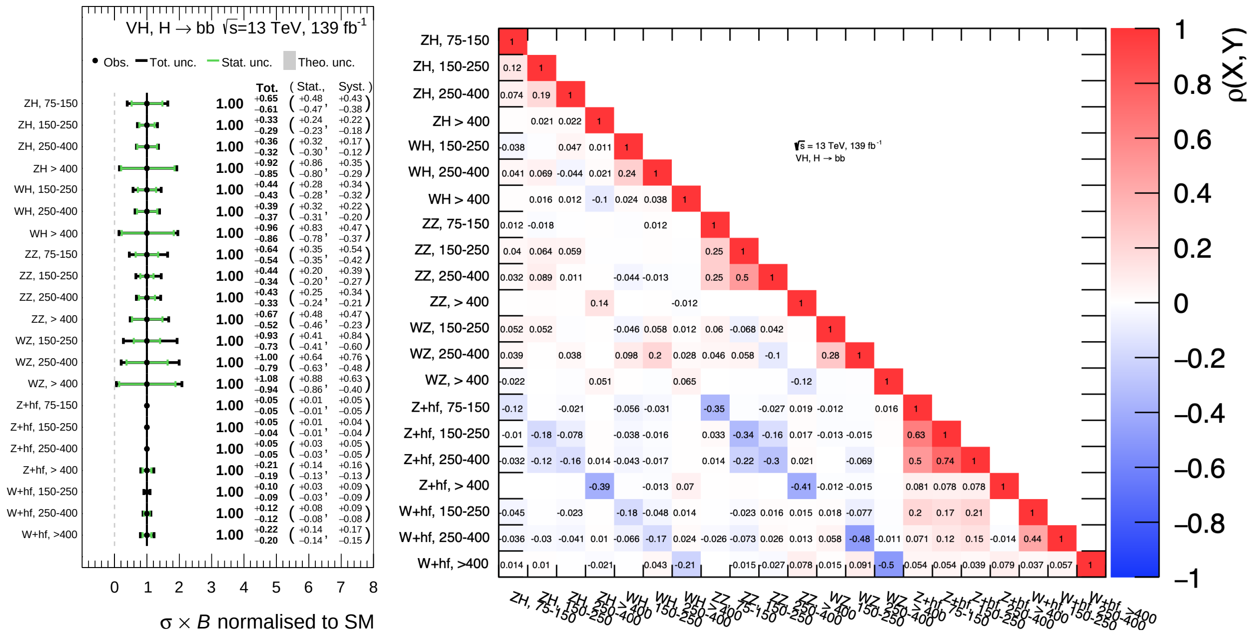

Figure 18: Simultaneously measured VH, VZ and V+hf signal strengths (left) and correlation matrix (right) in $p_T^{V,r}$ bins for Asimov data. Provided by the $VH, H \to b\bar{b}$ analysis team.

5.4 Technical Setup

The technical setup of the simultaneous SMEFT interpretation follows the boosted $VH, H \to b\bar{b}$ analysis [39]. The three cross-section terms in Equation 4 are simulated separately at leading order (LO) in QCD and QED using MadGraph 5 [44] with the SMEFTsim package [45] and the $\{m_W, m_Z, G_F\}$ scheme of electroweak input parameters. Showering and hadronisation of the objects are simulated with Pythia 8 [46]. The events are binned at generator level using the Rivet software [47] and are studied without consideration of detector effects.

The simulation starts with two protons in the initial state, except for the ZH process, for which only the quark-quark initiated production is considered since the calculations are LO in QCD. Contributions to the gluon-gluon ZH production are only introduced by next-to-next-to leading order contributions for dimension-6 SMEFT operators and are expected to be very small. Consequently, they are disregarded for this thesis. The VH process is simulated without the Higgs boson decay, but requiring a leptonic W or Z boson decay. For the diboson process, one Z boson is simulated to decay to a pair of b-quarks. The second vector boson decays leptonically. The V+hf process is simulated with one massive vector boson plus two b-quarks. The MadGraph commands are listed in Table 7 in the Appendix.

The average cross-sections per operator and their relative size with respect to the SM are investigated for the different processes. They are listed in Table 8 in the Appendix. The absolute cross-sections for the different processes have been cross-checked with the $VH, H \to b\bar{b}$ analysis. For VH, the relative cross-section difference with respect to the SM for the operators is found to be generally of the order of few percent. The largest deviations ($\approx 20\,\%$) is caused by $\mathcal{O}_{Hq}^{(3)}$. The relative deviations for the diboson and the $V+b\bar{b}$ processes are of $\mathcal{O}(1\%)$.

5.5 Parameterisation

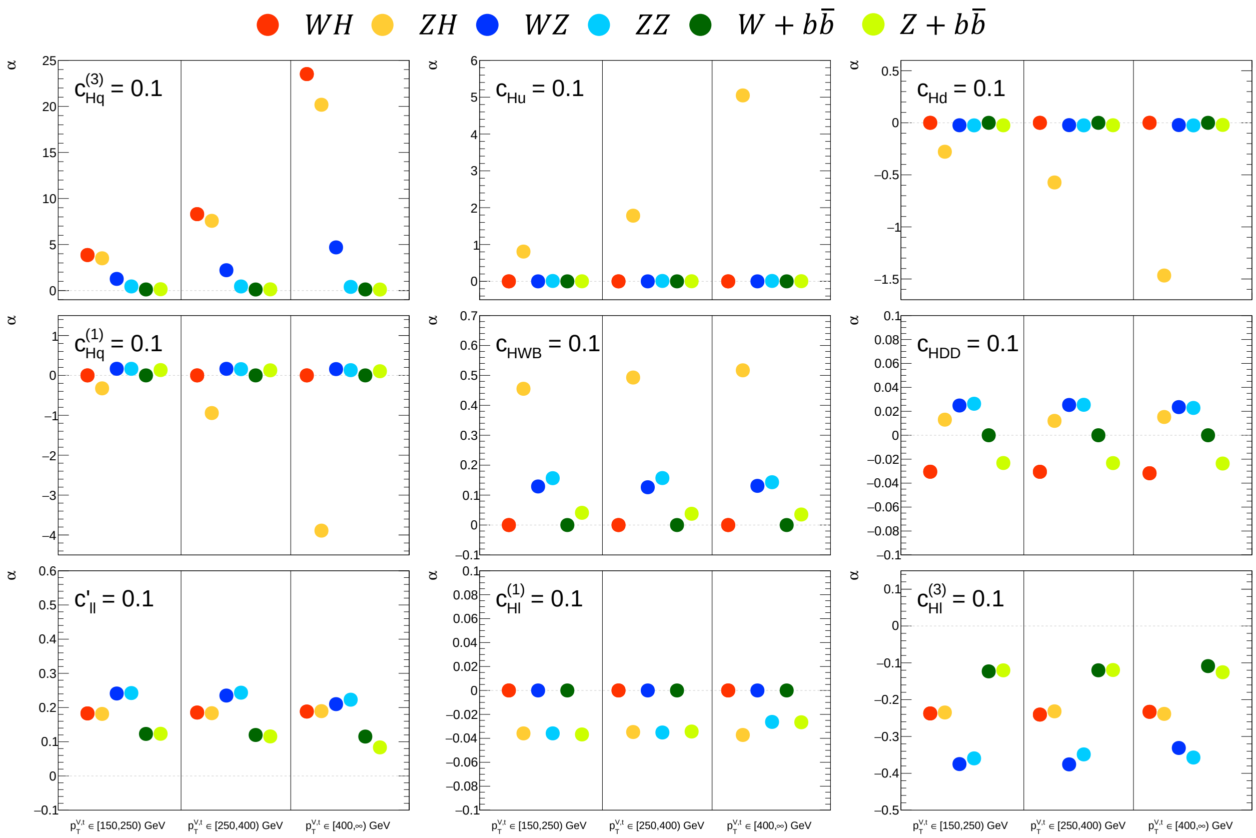

Figure 19: Linear parameter α_i obtained for $c_i = 0.1$ for three generator level bins $p_T^V \in \{[150, 250), [250, 400), [400, \infty)\}$ [GeV] with 200000 simulated events.

The sensitivity for an effective coupling is determined by the size of the effect of the corresponding operator on the SM prediction and the measurement precision. For small effective couplings, the cross-section deviations are expected to scale linearly with the Wilson coefficient c_i [48]. Hence, rewriting equations 3 and 4, the effective modifications caused by SMEFT operator $\mathcal{O}_i$ with respect to the SM cross-section can be parameterised for a fixed value of c_i:

$$\frac{\sigma_{\text{int}}}{\sigma_{\text{SM}}} \sim \frac{\sum_i 2\text{Re}\left(\mathcal{M}_{\text{SM}}^* \mathcal{M}_i^{(6)}\right)}{|\mathcal{M}_{\text{SM}}|^2} \sim \sum_i \alpha_i\, c_i \tag{6}$$

$$\frac{\sigma_{\text{BSM}}}{\sigma_{\text{SM}}} \sim \frac{\sum_{i,j} \left(\mathcal{M}_i^{(6)}\right)^* \mathcal{M}_j^{(6)}}{|\mathcal{M}_{\text{SM}}|^2} \sim \sum_{i,j} \beta_{ij}\; c_i\, c_j \tag{7}$$

The parameter α_i expresses the "linear" effect to the SM interference term of one operator $\mathcal{O}_i$ that is suppressed with Λ^{-2}. The "quadratic" parameter $\beta_{i,j}$ expresses either the effect to the Λ^{-4} suppressed contributions from one operator or the interference between two operators, which is also suppressed by Λ^{-4}. Consequently, a Wilson coefficient can be only constrained from bins which have a non-zero parameterisation. For this thesis, the parameters α and β are obtained per operator for 200000 Monte Carlo events per process which are binned in five transverse momentum

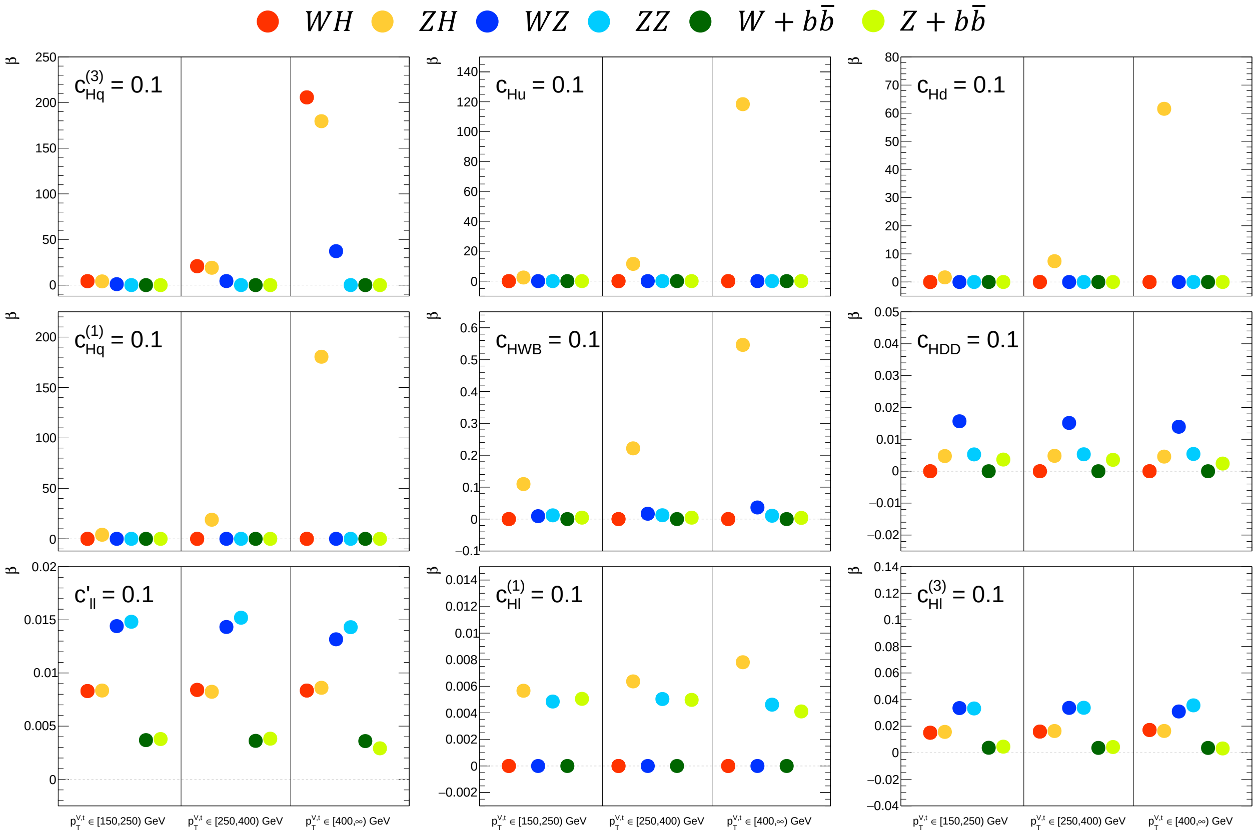

Figure 20: Quadratic parameter β_{ii} obtained for $c_i = 0.1$ for three generator level bins $p_T^V \in \{[150, 250), [250, 400), [400, \infty)\}$ [GeV] with 200000 simulated events.

bins ($p_T^V \in [75, 150), [150, 250), [250, 400)[400, \infty)$ [GeV]) on generator level. The choice of $c_i = 0.1$ assumes the modifications to be in the linear regime. For constraints that are much larger than $\mathcal{O}(0.1)$, this assumption might not hold true anymore, and the measurements is referred to as "insensitive" to this coupling.

Figure 19 and 20 show the parameters α and β per operator in the three highest p_T^V bins. The values are shown in red tones for the VH signal, in blue tones for VZ and in green tones for $V{+}b\bar{b}$. The operators introduce positive and negative interference effects on the cross-sections that scale differently with p_T^V, varying between the processes and the operators. Some operators do not modify all processes. For example, $\mathcal{O}_{Hu}$ does not affect the WH, WZ and $W{+}b\bar{b}$ processes because it only affects vertices with two up-type quarks. Consequently, the effective coupling c_{Hu} cannot be parameterised in these bins.

The VH process is particularly sensitive for $c_{Hq}^{(3)}$, c_{Hu}, c_{Hd} and $c_{Hq}^{(1)}$. The plots show that their modifications are p_T enhanced, and increase with $(p_T^V)^2$. The modifications from the $\mathcal{O}_{HWB}$ increase linearly with the transferred momentum of the VH process, albeit at a lower scale. The other four operators scale the VH cross-section as their effects are approximately constant over p_T^V. The plots furthermore show that the interference effects introduced to the diboson and $V{+}b\bar{b}$ cross-sections are smaller for p_T^V-dependent operators, and of about the same size for the others. For c_{HDD}, c'_{ll} and $c_{Hl}^{(3)}$, the effects are even larger for VZ than for VH. This is partially due to operators modifying the hadronic Z decays. Apart from the quadratically increasing interference for the $\mathcal{O}_{Hq}^{(3)}$ operator, all deviations of the diboson process are approximately constant over p_T. The operators affect the $V{+}b\bar{b}$ cross-sections the least. Nevertheless, sensitivity improvements are expected given the high precision of the signal strength measurement.

5.6 Fit model

The aim of this study is the extension of the SMEFT parametrisation to some backgrounds and the test of the impact the novel parametrisation on the constraints of Wilson coefficients. This thesis presents this novel approach with a χ^2-fit model. The model simplifies the errors estimate for the measured signal strengths $\hat{\sigma}$ to be Gaussian and uses the average of the upper and lower uncertainty estimate $\Delta\hat{\sigma} = (\Delta\sigma_{\text{upper}} + \Delta\sigma_{\text{lower}})/2$. The correlation between any two bins is given by $V_{i,j} = \rho_{i,j}\Delta\sigma_i\Delta\sigma_j$, where $\rho_{i,j}$ is the correlation coefficient and is taken from the measurement. With the vector $\vec{x} = (\hat{\sigma}_i, \hat{\sigma}_j, \dots)^T$, the χ^2-fit function is given by

$$\chi^2(\vec{c}) = \frac{1}{2}\,\big(\,\vec{x} - \vec{\mu}(\vec{c})\,\big)^T\; V^{-1}\;\big(\,\vec{x} - \vec{\mu}(\vec{c})\,\big) \tag{8}$$

The vector $\vec{\mu}(\vec{c})$ expresses the signal strength per bin as a function of the Wilson coefficients $\vec{c}$, that are minimised for. The parametrisation changes depending on the contributions that are considered:

$$\begin{array}{lrcl}
\text{Linear} & \vec{\mu}(c_1) & = & \big(1+\alpha_i c_1\ ,\ 1+\alpha_j c_1\ ,\ \dots\big)^T \\
\text{Linear + quadratic} & \vec{\mu}(c_1) & = & \big(1+\alpha_i c_1+\beta_i c_1^2\ ,\ 1+\alpha_j c_1+\beta_j c_1^2\ ,\ \dots\big)^T \\
\text{Linear correlation} & \vec{\mu}(c_1,c_2) & = & \big(1+\alpha_{1\,i} c_1+\alpha_{2\,i} c_2\ ,\ 1+\alpha_{1\,j} c_1+\alpha_{2\,j} c_2\ ,\ \dots\big)^T \\
\text{Linear + quadratic} & \vec{\mu}(c_1,c_2) & = & \big(1+\alpha_{1\,i} c_1+\beta_{1\,i} c_1^2+\alpha_{2\,i} c_2+\beta_{2\,i} c_2^2+\beta_{1,2\,,i} c_1\,c_2\ , \\
\text{correlation} & & & \ 1+\alpha_{1\,j} c_1+\beta_{1\,j} c_1^2+\alpha_{2\,j} c_2+\beta_{2\,j} c_2^2+\beta_{1,2\,,j} c_1\,c_2\ ,\ \dots\big)^T
\end{array}$$

The 68% (1σ) and 95% (2σ) confidence intervals (CI) are obtained from scans around the best fit values. The 68% level in the 1D case is obtained by evaluating the expression $\chi^2(c){-}\chi^2_{min}{\approx}\,0.49$, and ≈ 1.92 for the 95% limit. For the combined constraint, the equation is evaluated to $\chi^2(c_1,c_2){-}\chi^2_{min}{\approx}\,1.15$ for the 68% and ≈ 3.0 for the 95% confidence interval.

5.7 Simultaneous fit to VH and VZ at high p_T^V

The previous section illustrated the effects of some dimension-6 SMEFT operators on the VH, VZ and $V{+}b\bar{b}$ cross-sections. This sections presents the constraints on some operators affecting the Higgs-production obtained from a simultaneous fit of the VH and VZ signal strengths measured in $p_T^V{\in}[250,400),[400,\infty)$ [GeV].

The fit model is cross-checked by comparing the χ^2-CIs from a fit to the VH signal strengths published by the boosted analysis to the likelihood fit CIs published therein. The CIs are similar for both, the linear and quadratic case, which validates the χ^2-fit as a suitable proof-of-concept. The values are listed in the Appendix in Tables 9 and 10. The most significant differences between the two models are observed for the the quadratic case due to second minima that split the CI differently for c'_{ll} and $c_{Hl}^{(3)}$. The difference could result from both the different statistical treatment and small differences in the parametrisation. The VH χ^2-fit serves as a baseline to which the other fits are compared to. Naturally, the next step is to repeat the study by a full likelihood fit and include systematic uncertainties to validate the χ^2-model.

5.7.1 Confidence intervals for VH VZ

The following section presents the 1D and 2D CIs obtained from simultaneous fits of the VH and VZ signal strengths measured in generator level bins $p_T^V \in [250, 400), [400, \infty)$ GeV. The results are compared to a fit of solely the VH bins.

1D confidence intervals

Figure 21 shows the 1D χ^2-scans for one Wilson coefficient at a time, while the others are set to zero. Violet lines show the result for the linear parametrisation, green lines the linear + quadratic parametrisation. Dashed lines show the fit to the VH signal only, solid lines show the simultaneous fit to VH and VZ. Gray dashed lines indicate $\chi^2 - \chi^2_{min}$ corresponding to the 1σ and 2σ intervals. The fit results including the relative difference of the VH+VZ CI sizes with respect to the VH

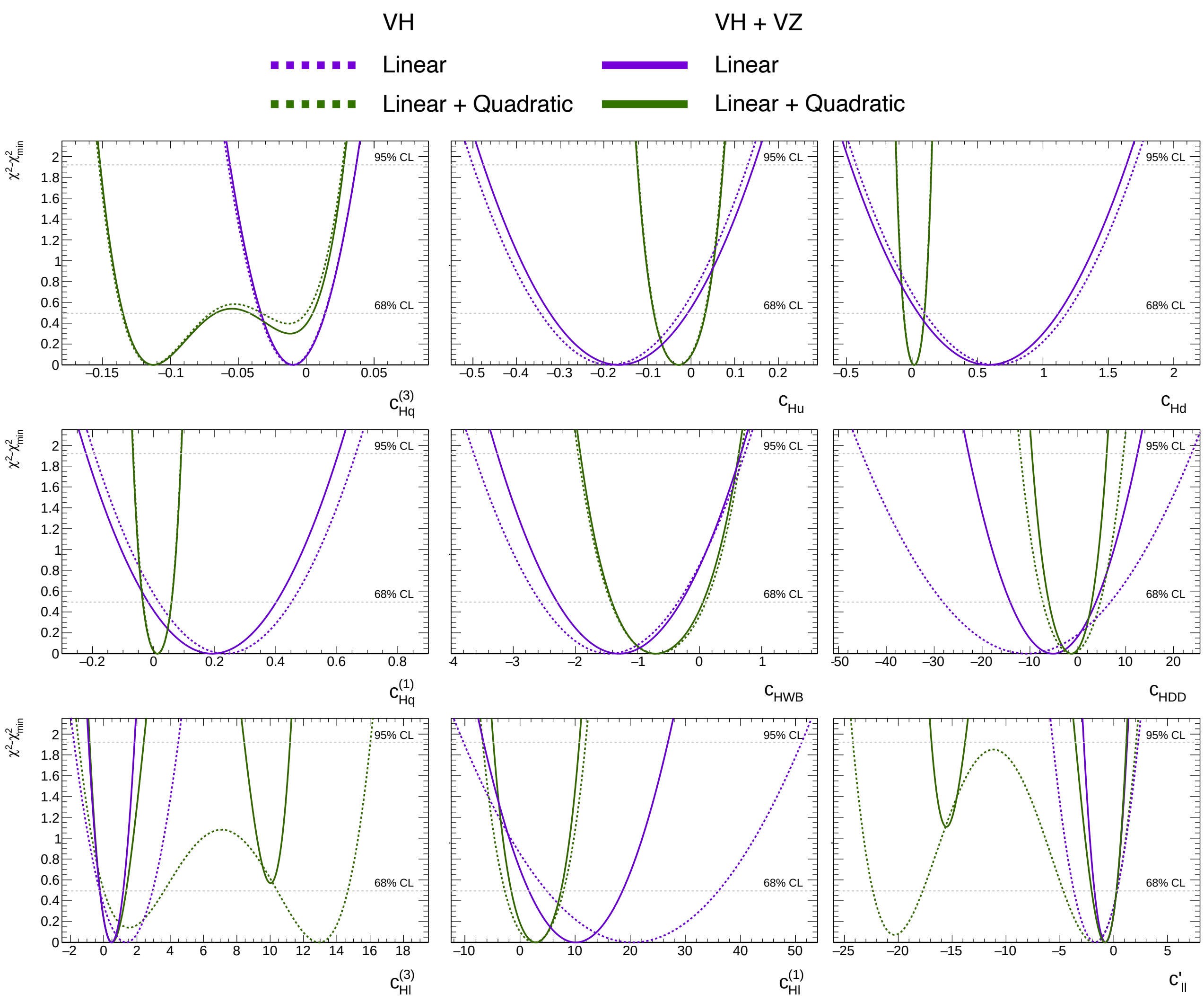

Figure 21: χ^2-scans for fits to VH (dashed) and VH+VZ (solid) signal strengths measured in $p_T^V \in [250, 400), [400, \infty)$ [GeV] bins for the linear (violet) and the linear+quadratic parametrisation in green. The dashed gray lines indicate the $\Delta\chi^2$ values corresponding to the 68% and 95% CIs.

baseline are listed in the Appendix in Tables 11 and 12.

All constraints are in agreement with the SM prediction (c_i=0) for both parametrisations and both fits. Including the diboson backgrounds moves the best fit values closer to zero and shrinks the CIs. Five operators, namely c_{Hu}, c_{Hd}, $c_{Hq}^{(1)}$, $c_{Hl}^{(1)}$ and c_{HWB}, do not affect the WH process. The simultaneous interpretation of VH+VZ therefore increases the number bins by three, and doubles them for the other operators. The significant differences observed between the linear parametrisation and the linear + quadratic parametrisation are also observed for the combined VH+VZ fit. Similarly to the VH fit, secondary local minima are observed for the operators $\mathcal{O}_{Hq}^{(3)}$, $\mathcal{O}_{Hl}^{(3)}$ and c'_{ll}. As explained in Section 2, the incompleteness of the quadratic terms complicates the interpretation of the linear + quadratic contributions.

The effective couplings of operators that cause p_T-enhanced modifications are constrained significantly better from a fit to the VH signal than operators that do not. For the former type of operators, in particular $c_{Hq}^{(3)}$, c_{Hu}, c_{Hd}, c_{HDD} and c_{HWB}, the best fit values and the CIs for the linear and the linear + quadratic parametrisation do not change when the diboson production is parameterised because VZ is significantly less affected by these operators than VH. The single exception is $c_{Hq}^{(3)}$. Its linear + quadratic 68% CI shrinks by about 20%, because the the second local minimum close to $c_{Hq}^{(3)} = 0$ become more prominent for a combined interpretation of VH+VZ. In general, $c_{Hq}^{(3)}$ is constrained best since it introduces the largest deviation to the p_T spectra.

The constraints on other effective couplings are significantly improved when modifications to the diboson are considered, too. As it has been shown in Figures 19 and 20, the modifications of the VZ cross-sections for c_{HDD}, $c_{Hl}^{(3)}$, c'_{ll} and $c_{Hl}^{(1)}$ are affected similarly to VH. This translates into an improvement of the linear constraints by about 50%. For the linear + quadratic case, the CI for $c_{Hl}^{(3)}$ and c'_{ll} shrink by about 80%, for c_{HDD} and $c_{Hl}^{(1)}$ by about 20%. The second minima seen for c'_{ll} and $c_{Hl}^{(3)}$ when considering the quadratic terms are excluded at 1σ level when including the VZ into the fit, the 95% CI are split into two separate CIs.

Figure 22 shows an overview of the CIs for the linear (left) and linear + quadratic (right) parametri-

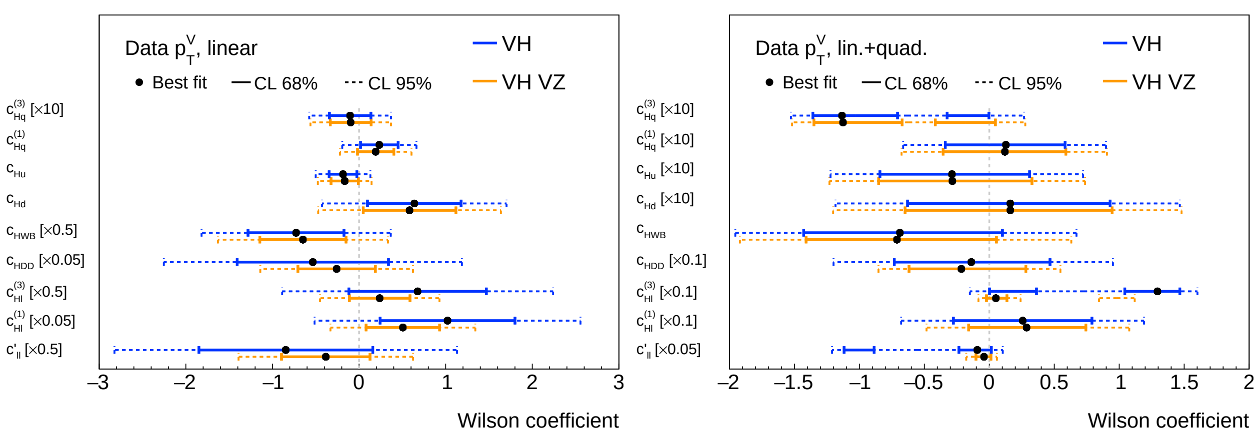

Figure 22: χ^2-CIs for the linear (left) and linear+quadratic (right) parametrisation for VH (blue) and VH+VZ (orange).

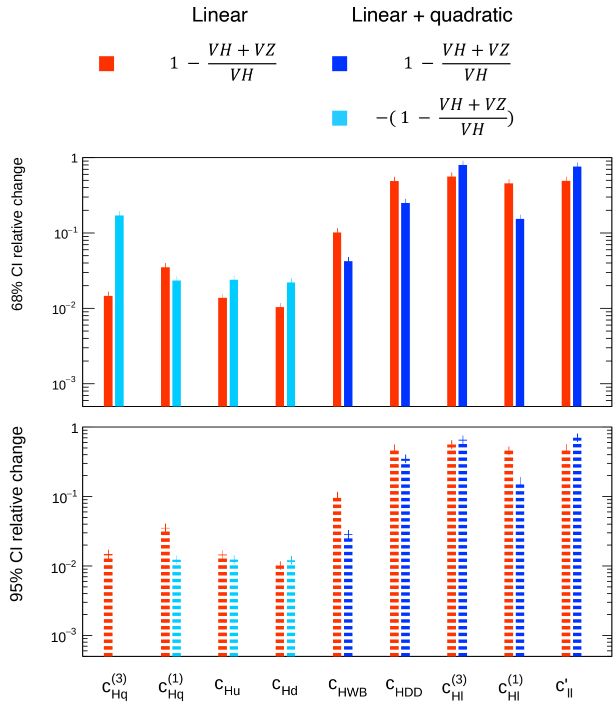

Figure 23: Relative change of the χ^2 CIs.

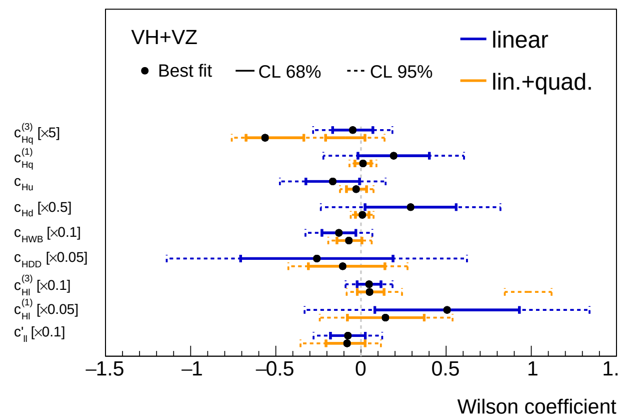

Figure 24: χ^2 CIs result for a linear and linear+quadratic parametrisation for $VH{+}VZ$.

sation for VH (blue) and $VH{+}VZ$ (orange), the values are tabulated in the Appendix in Tables 11 and 12. The relative change of the the confidence intervals in shown in Figure 23 for both parametrisations. In summary, the constraints for Wilson coefficients that the $VH, H{\to}b\bar{b}$ analysis is sensitive to most do not change significantly when considering modifications to the diboson process. The effective couplings are constrained within $\mathcal{O}(0.1)$. The novel approach improves however significantly the constraints for Wilson coefficients the signal interpretation is not sensitive to. The measurement becomes sensitive to some coefficients when $VH{+}VZ$ are fitted simultaneously as the linear CIs shrink by up to 50% and up to 70% when additionally considering quadratic contributions. Figure 24 shows the significant difference between the linear and linear + quadratic parametrisation that is observed for the VH and $VH{+}VZ$ fits.

2D confidence intervals

The 1D scans of individual operators assume the other operators to be zero. Obtaining limits without this assumption requires a simultaneous high-dimensional fit to all operators in consideration. This is impossible given the limited amount of bins available. The $VH, H{\to}b\bar{b}$ analysis observed large correlations between pairs of simultaneously fitted operators. Given the improvement described for the 1D scans, the following section investigates the effect of including the diboson background to 2D scans of two operators at once, while the other coefficients are fixed to zero. All pairs of two post-fit Wilson coefficients are found to be in agreement with the SM prediction within the 68% confidence contour.

Figure 25 provides three examples of operator pairs that have been fitted with the linear (left) and linear + quadratic parametrisation (right). The VH confidence contours are drawn in orange, $VH{+}VZ$ in blue. In general, the correlation plots reveal similar features as the 1D scans. For

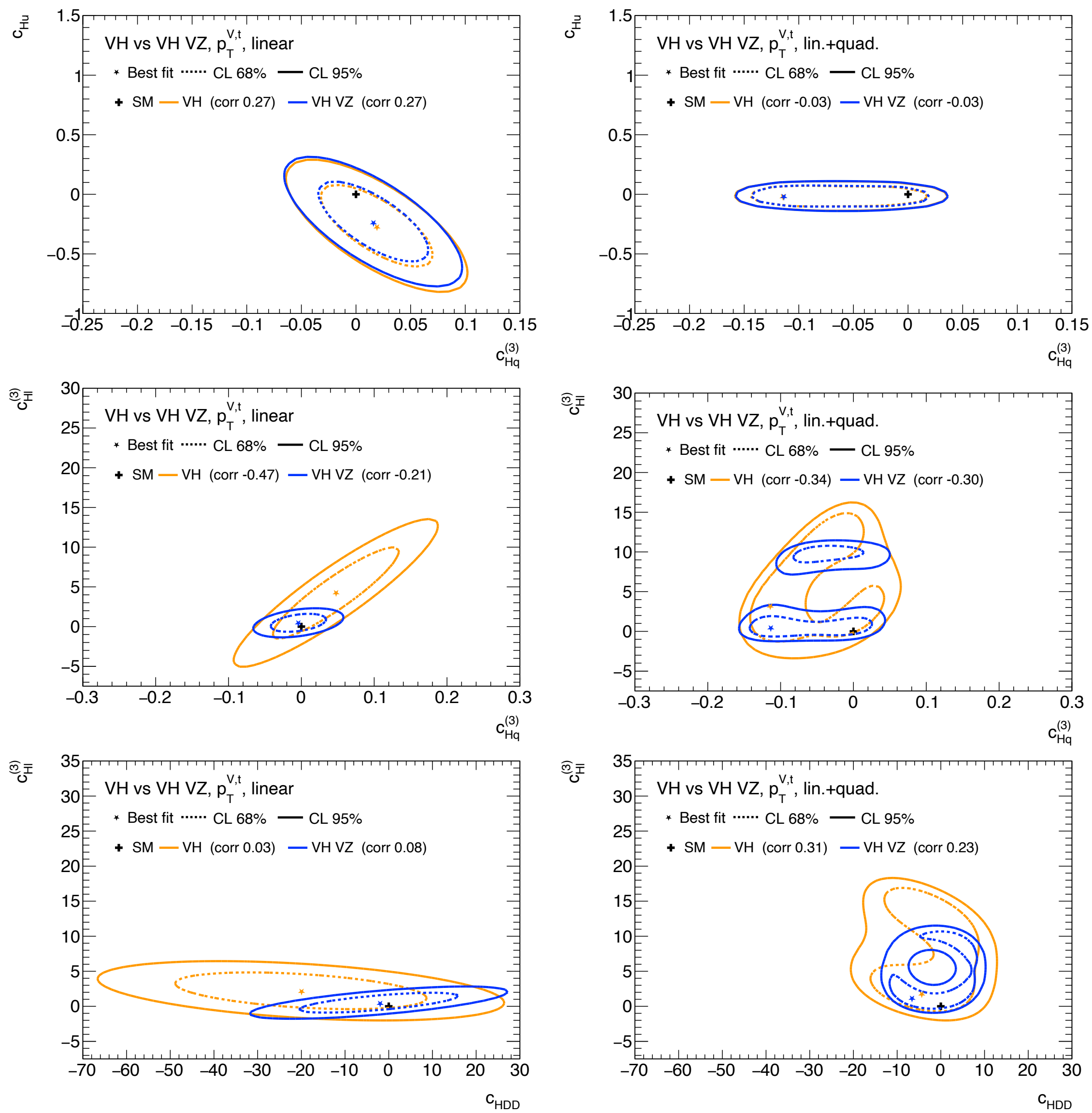

Figure 25: Confidence contours for the simultaneous fit of two operators for VH (orange) and $VH{+}VZ$ (blue) for the linear (left) and linear + quadratic (right) parametrisation models.

several coefficients, the 2D CIs are larger than the 1D CIs, highlighting the importance of a careful treatment of the correlations. As for the 1D case, significant differences between the linear and linear + quadratic parametrisations are observed. For example, $c_{Hq}^{(3)}$ and c_{Hu} have been constrained the most by VH given their p_T-enhanced modifications to this process. Similar to the 1D scans, including VZ neither does improve the 2D constraints significantly, nor resolves the degeneracy when considering quadratic contributions. Nonetheless, the quadratic contributions de-correlate the two coefficients, and shift $c_{Hq}^{(3)}$ to a negative value. Including the VZ process does not only improve the constraints in the 1D $c_{Hl}^{(3)}$ fit, but also improve the 2D CIs for $c_{Hl}^{(3)}$ and $c_{Hq}^{(3)}$. The simultaneous fit reduces the 2D CIs significantly and halves the correlation coefficient between the two coefficients. Furthermore, the best fit is significantly closer to the SM prediction. The $VH{+}VZ$ fit constrains the two minima in $c_{Hl}^{(3)}$ in two distinct CIs that are flat in the $c_{Hq}^{(3)}$ direction, rather which which improves the constraint significantly, but does not change the best fit value. The linear 2D CIs for c_{HDD} and $c_{Hl}^{(3)}$ are larger than the respective 1D directions, despite the small correlation between the couplings. The $VH{+}VZ$ CI shrink significantly and change the correlation with respect to VH. Moreover, the best fit value are closer to the SM prediction. For both fits, the CIs double in $c_{Hl}^{(3)}$ and half in c_{HDD} when considering the quadratic contributions. The second local minimum for $c_{Hl}^{(3)}$ leads to a ring-shaped 95% $VH{+}VZ$ contour which excludes $c_{HDD} \approx -3$ and $c_{Hl}^{(3)} \approx -5$, demonstrating once again the impact of correlations on the constraints.

5.7.2 Shape effects for VZ

SMEFT operators can affect the vector boson production and decay, and cause slight modifications not only to the p_T^V spectrum that is used to constrain the effective couplings, but also potentially to other observables, particularly p_T^V, $\Delta R_{b,b}$, E_T^{miss}, m_{bb} and m_{ll}. The log-likelihood (LLH) fit performed by the $VH, H{\to}b\bar{b}$ analysis extracted the Wilson coefficient by scaling the measured m_J distribution. The fit assumes that the spectrum and the kinematics per STXS bin are still SM-like despite the modifications by the SMEFT operators. The assumption has been verified for the VH processes. The largest deviation, caused by $\mathcal{O}_{Hq}^{(3)}$, impacted the CI by less than 20% [36]. This thesis verifies the SM-like kinematics additionally for the VZ process by comparing the SM prediction to shapes scaled to $c_i = c_{\text{best fit}} {\pm} 1\sigma$ for the linear parametrisation for two STXS bins $p_T^V {\in} \{[250, 400), [400, \infty)\}$ [GeV]. The study uses simulated events that include the vector boson to τ-lepton decay at generator level. It does not consider any reconstruction inefficiencies. No significant changes were observed that would require a finer p_T^V binning.

The VZ p_T^V spectra are SM-like for any operator, and any deviation is within agreement with the SM given the statistical uncertainty. As seen from the parametrisation, the deviations are significantly smaller than observed for the VH spectra. As an example, Figure 26a presents the p_T^V spectra for WZ for $c_{Hq}^{(3)}$: $c_{\text{best fit}} \pm 1\sigma = (0.004, -0.042)$ in orange and blue, respectively. They are compared to the SM prediction drawn in black. The VZ spectra are falling and, as expected from the parametrisation, the deviations caused by $\mathcal{O}_{Hq}^{(3)}$ are enhanced with $\sim (p_T^V)^2$, which is especially well visible in the high p_T^V bin on the right.

The resolved $VH, H{\to}b\bar{b}$ analysis uses ΔR_{bb} to separate signal and background and is an important variable for the boosted measurement, too. Operators that affect the Lorentz boost of the $Z{\to}b\bar{b}$ decay might therefore not be constrained properly if the ΔR_{bb} spectra were modified significantly. The spectra are SM-like for all operators, peaking at small values and falling sharply to zero at $\Delta R_{b,b} \approx 4$. Given the larger boost, the peak shifts to smaller ΔR_{bb} values with higher p_T^V. For example, Figure 26b shows the systematic shifts to larger radii for $c_{Hq}^{(3)}$ for WZ, corresponding to a smaller transferred momentum as it is observed in the p_T^V spectra. The deviations are in agreement with the SM and even smaller for the ZZ spectra given the process' smaller parametrisation, validating the assumption SM-like kinematics of the LLH fit.

No significant deviations are found for the $Z, W{\to}l\nu, Z$ and $Z, Z{\to}\nu\nu$ E_T^{miss} spectra, two examples for $c_{Hq}^{(3)}$ are shown in Figure 26c. The spectra are highly p_T^V dependent as the neutrino(s) carry fractions of the bosons momentum. The WZ E_T^{miss} spectrum rises until the lowest possible p_T^V and falls towards the highest. For the $Z, Z{\to}\nu\nu$ decay, the p_T^Z is carried by the two neutrinos that are indirectly measured in the E_T^{miss} spectrum, any entries lower than the minimum p_T^V arise mainly

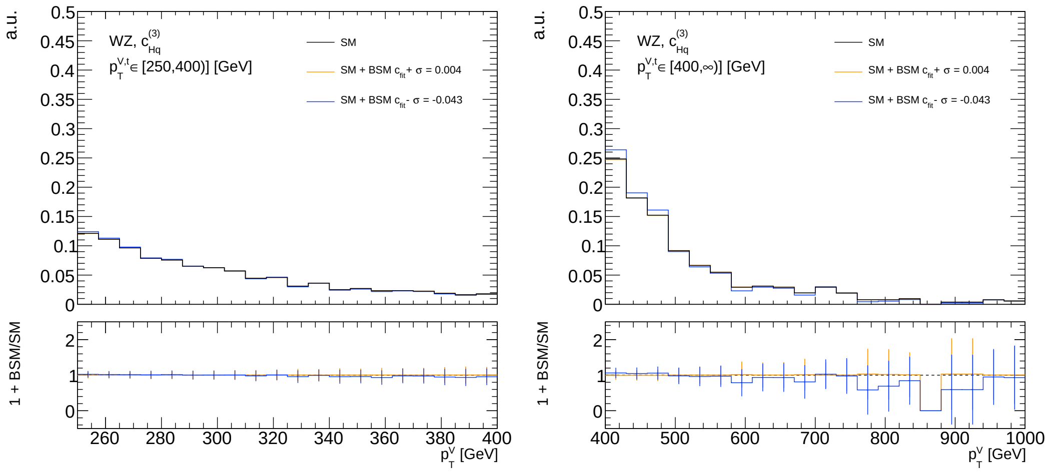

(a) $p_T^{W,t}$ for WZ for $p_T^{V,t} \in \{[250,400)$ (left) , $[400,\infty)$ (right)$\}$ [GeV]

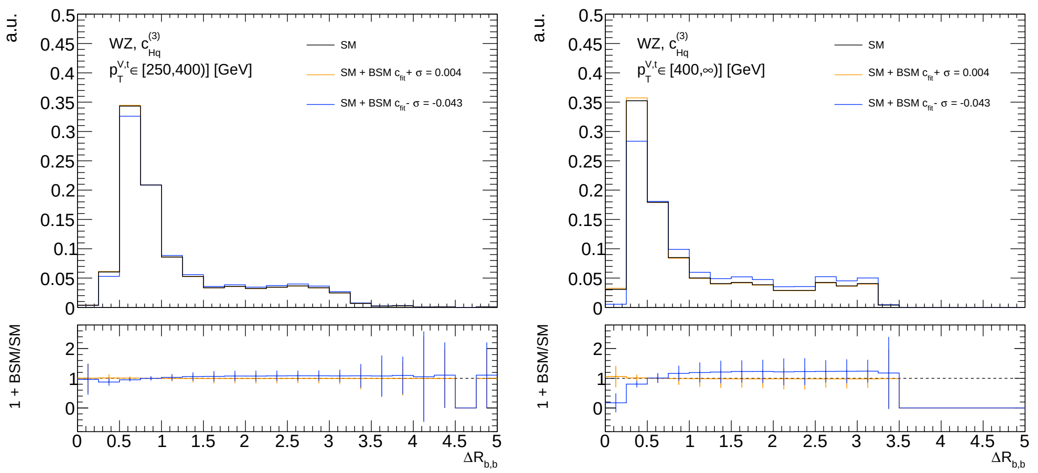

(b) ΔR_{bb} for WZ for $p_T^{V,t} \in \{[250,400)$ (left) , $[400,\infty)$ (right)$\}$ [GeV]

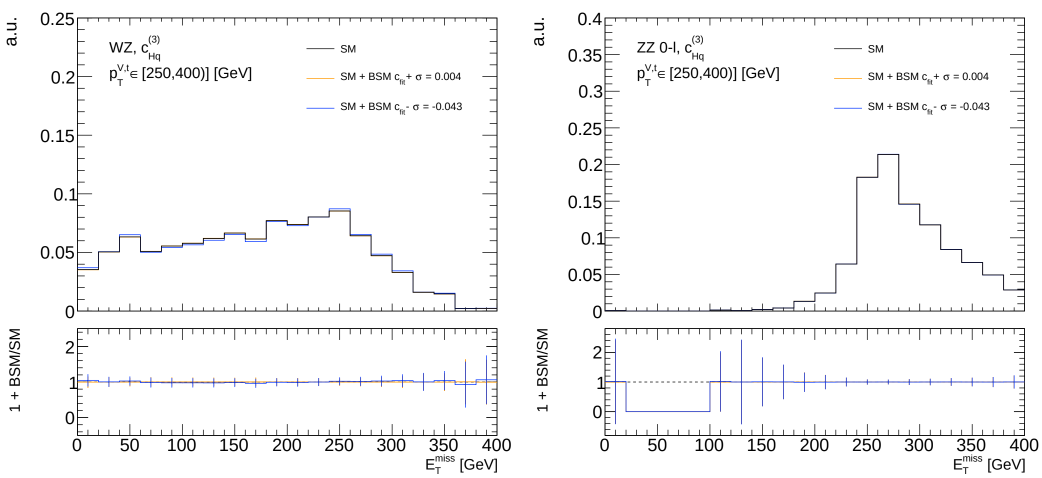

(c) $E_T^{\rm miss}$for $p_T^{V,t} \in \{[250,400)\}$ [GeV] for WZ (left) and ZZ 0-lepton (right).

Figure 26: $c_{Hq}^{(3)} = c_{\text{best fit}} \pm 1\sigma$ spectra for the linear parametrisation.

from semi-leptonic B-hadron decays, or one neutrino outside the experiments acceptance.

The invariant mass spectra of the b-quarks and the charged leptons from the Z boson decays ($Z \to b\bar{b}, Z \to l^+ l^-$) are independent from p_T^V as the decays occur at the energy scale of $m_Z \approx 90\,\text{GeV}$. No significant or systematic deviations of the observables with respect to the SM predictions are observed for any operators for any process.

5.8 Simultaneous fit to VH, VZ and V+heavy flavour

The V+heavy flavour (V+hf) process is an additional irreducible background to the signal. Given the high measurement precision of the signal strengths for the process ($\mathcal{O}(10)$ better than for VH and VZ), even minuscule deviations introduced by dimension-6 operators can lead to significant improvements of the constraints. The following section is based on the Asimov SM expectation for the VH, VZ and V+hf signal strengths that are measured in reconstructed $p_T^{V,r} \in [75, 150), [150, 250), [250, 400), [400, \infty)$ [GeV] bins matching the STXS bins of the combined $VH, H \to b\bar{b}$ analysis. Given the $\text{U}(3)^5$ flavor assumption, the parametrisation for V+hf is obtained with MC samples that simulate two b-quarks instead of at least two heavy flavour jets, and the notation $V+b\bar{b}$ is used instead.

5.8.1 Expected confidence intervals

Expected 1D confidence intervals

Figure 27 shows the expected linear and linear + quadratic 68% and 95% CIs for the new simultaneous interpretation of VH, VZ and $V+b\bar{b}$ in orange and the VH baseline in blue. The fits including only one background are separately shown in violet for VH+VZ and VH+V+$b\bar{b}$ in green to demonstrate the impact of each process. Solid lines show the 68% CI, dashed the 95% CIs. The corresponding χ^2 scans and the fit results are given in the Appendix in Figure 38 and Tables 14 and 15, respectively.

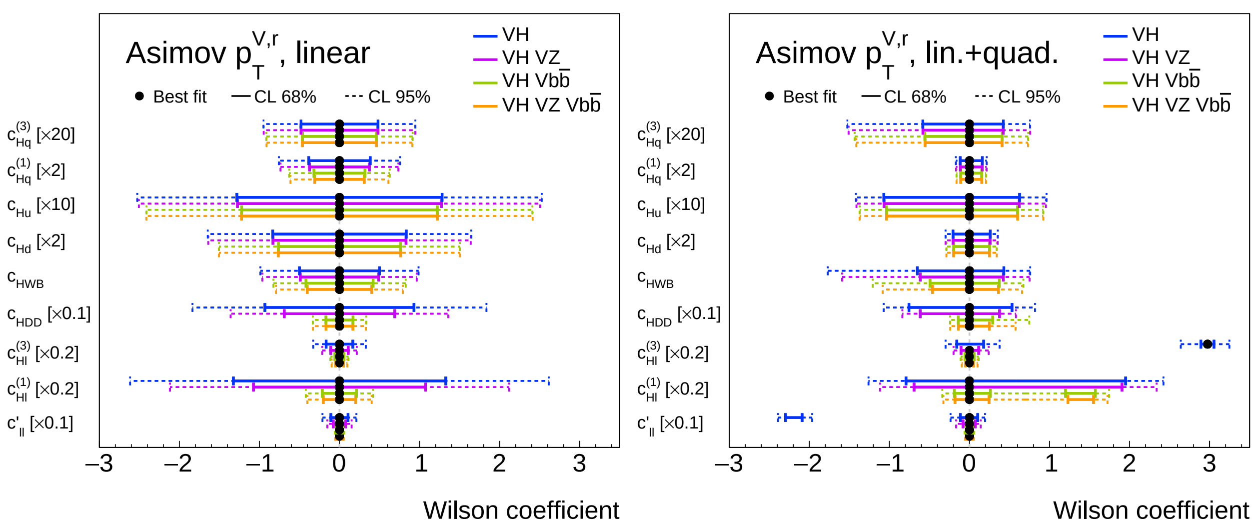

Figure 27: Expected CIs for the linear (left) and linear+quadratic (right) parametrisation.

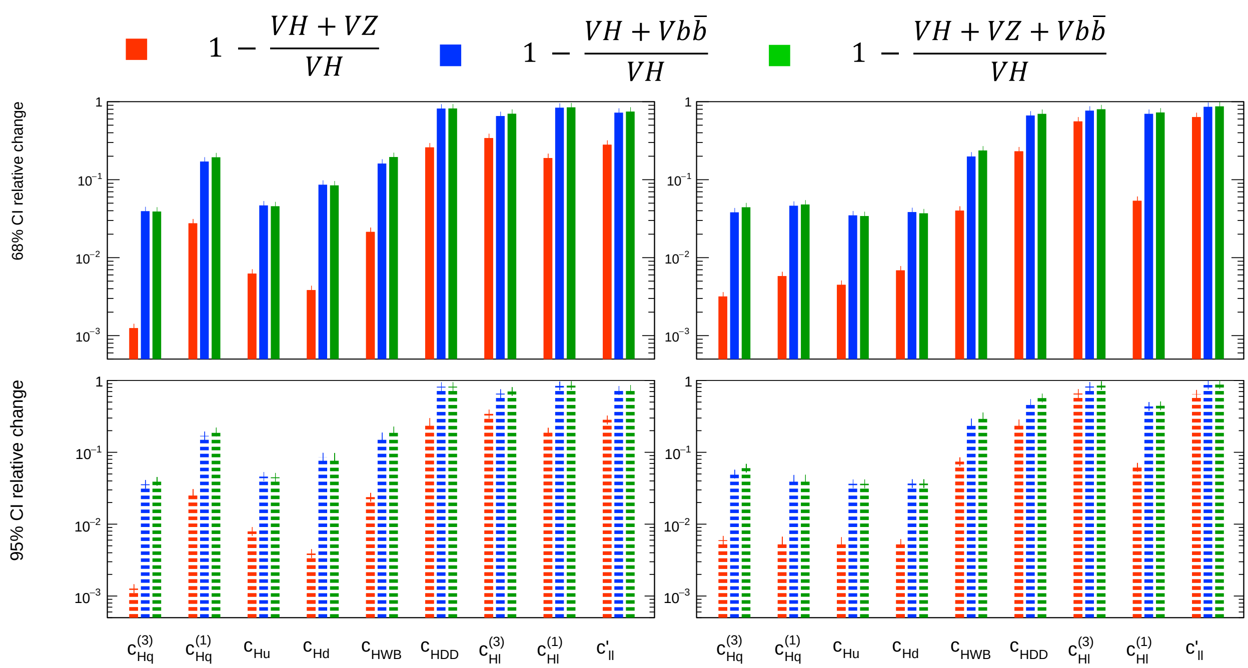

(a) Linear parametrisation

(b) linear + quadratic parametrisation

Figure 28: Relative change of the χ^2-CIs for the combined interpretation for Asimov data.

Given the aforementioned precision and the equivalent modifications caused by dimension-6 SMEFT operators, the $V{+}b\bar{b}$ parametrisation leads to a larger expected improvement than VZ, as it is well visible in Figure 28. The plot shows the relative improvement of the CIs with respect to VH in percent for the linear (left) and linear + quadratic parametrisation (right). Red shows the improvement from $VH{+}VZ$, blue $VH{+}V{+}b\bar{b}$ and green $VH{+}VZ{+}V{+}b\bar{b}$. Notably, the simultaneous constraint of all processes is dominated by the $V{+}b\bar{b}$ parametrisation. Like in the case of the diboson process, not all operators affect $V{+}b\bar{b}$. For example $\mathcal{O}_{Hd}$ and $\mathcal{O}_{Hu}$, that do not affect $W{+}b\bar{b}$ since they only affect vertices with two up- or down-type quarks and a massive vector boson. Including both backgrounds to the fit gives 68% and 95% CIs that are smaller than one, with the exception of $c_{Hl}^{(1)}$ and c_{HDD} which are constrained to $\mathcal{O}(1)$.

Neither the VZ nor the $V{+}b\bar{b}$ background parametrisation are expected from the SM data to improve the constraints for $c_{Hq}^{(3)}$, c_{Hu} since their constraints are dominated from the $(p_T^V)^2$-enhanced VH modifications. The same reasoning applies to $c_{Hq}^{(1)}$ and c_{Hd} with regard to the diboson background. Yet, including $V{+}b\bar{b}$ improves the expected linear CIs by $\mathcal{O}(10\%)$. The fits demonstrate that also the consideration of $V{+}b\bar{b}$ does not alter the constraints on coefficients the $VH, H{\to}b\bar{b}$ is sensitive to. $\mathcal{O}_{HWB}$ causes p_T^V-dependent modifications to WH. For both parametrisations, the fit to both signal and the two backgrounds shrink the constraints by about 20%.

As mentioned before, $\mathcal{O}_{HDD}$, $\mathcal{O}_{Hl}^{(3)}$, $\mathcal{O}_{Hl}^{(1)}$ and c'_{ll} scale the cross-sections for all considered processes constantly over p_T^V, the corresponding coupling are less constrained than the other operators. The inclusion of the $V{+}b\bar{b}$ process into the fit improves their expected limits by 70-85% in the linear case and by about 50-90% in the linear + quadratic case. The Asimov data demonstrate that the constraints for operators the measurement is not sensitive to can be significantly improved for a

consistent parametrisation of the signal and backgrounds in terms of effective couplings.
Figure 29 shows the significant difference between the CIs for the interpretation of VH, VZ and $V{+}b\bar{b}$ for the linear (blue) and linear + quadratic parametrisation (orange). The difference is significantly larger for operators that cause $(p_T^V)^2$ enhanced modifications. Only for $c_{Hl}^{(1)}$, a degenerated CI is expected from the SM data. The same reasoning as for the $VH{+}VZ$ fits applies.

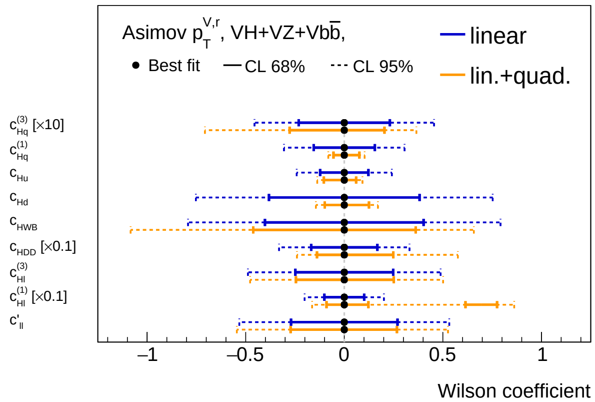

Figure 29: Expected χ^2 CIs for a linear and linear + quadratic parametrisation for $VH{+}VZ{+}V{+}b\bar{b}$.

Expected 2D confidence limits

Given the improvements seen for the one-dimensional background interpretation, particularly $V{+}b\bar{b}$, the 2D constraints of coefficient pairs and their correlations are also expected to be improved for most Wilson coefficients. As expected for an Asimov dataset, all operator pairs are in agreement with the SM prediction within the 68% confidence contour. Figure 30 shows three examples for the expected 2D CIs for operators pairs for the combined fit of $VH{+}VZ{+}V{+}b\bar{b}$ (blue) with respect to VH (orange) for the linear (left) and linear + quadratic parametrisation (right). While the background interpretation does not improve the 2D CIs for c_{Hu} and $c_{Hq}^{(3)}$, the novel approach is expected to shrink the 2D CI for $c_{Hl}^{(3)}$ and $c_{Hq}^{(3)}$ significantly and to nearly de-correlate the coefficients. For the linear + quadratic parametrisation, the $c_{Hl}^{(3)}$ degeneracy is expected to be removed. Similar improvements are also expected in the example of c_{HDD} and $c_{Hl}^{(3)}$.

5.8.2 Expected shape effects

The assumption of SM-like kinematics per STXS bin is also investigated for the $V{+}b\bar{b}$ processes in generator bins $p_T^{V,t} \in \{[75,150),[150,250),[250,400),[400,\infty)\}$ [GeV] for constraints obtained from a fit to VH, VZ and V+hf signal strengths estimated with Asimov data. The processes $W{\to}l\nu, {+}b\bar{b}$, $Z{\to}l^+l^-, {+}b\bar{b}$ and $Z{\to}\nu\nu, {+}b\bar{b}$ are studied separately. For none of the p_T^V, ΔR_{bb}, E_T^{miss}, m_{bb} and m_{ll} spectra any significant or systematic deviations are expected.

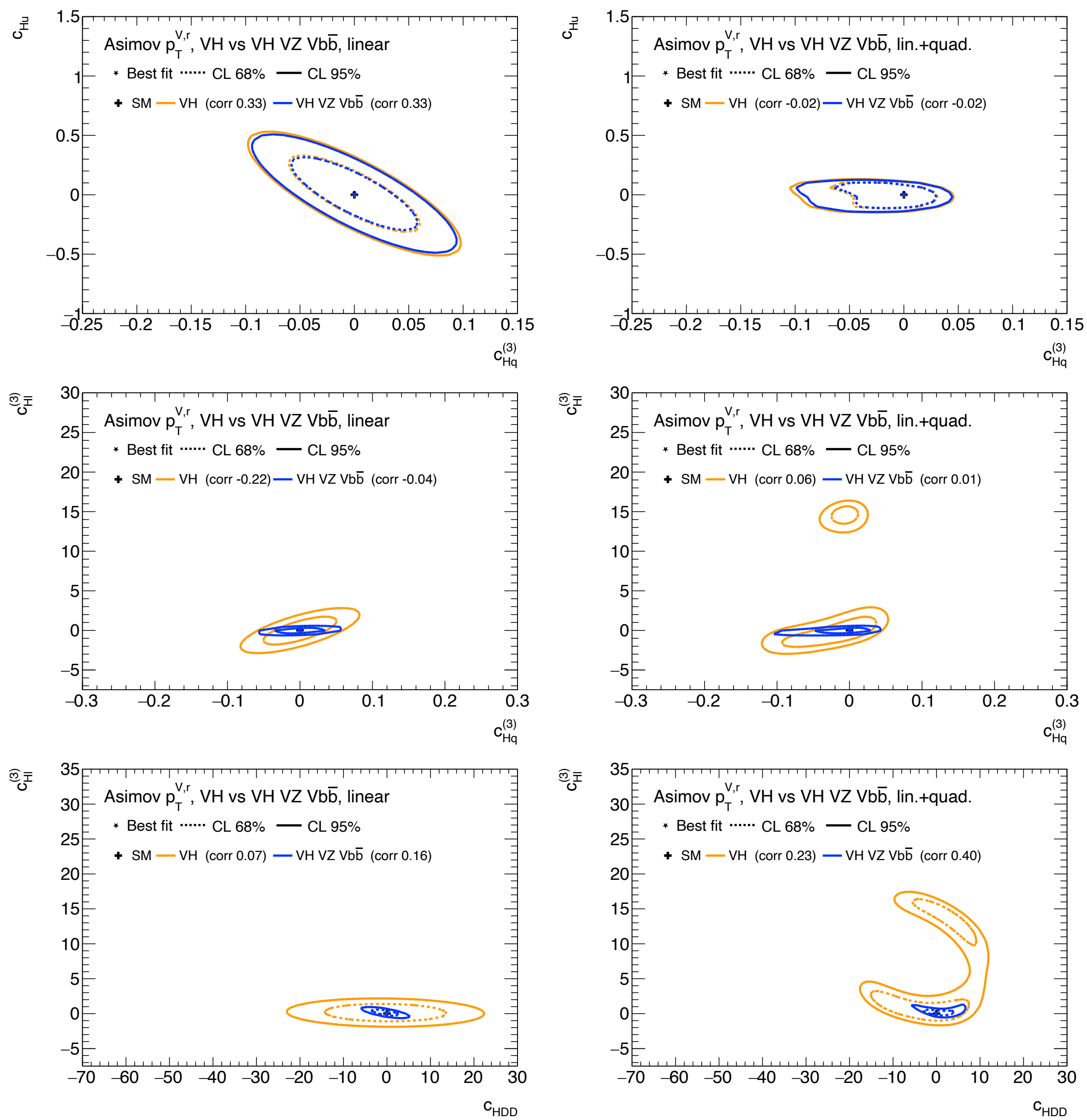

Figure 30: Confidence contours for the simultaneous fit of two operators for VH (orange) and $VH{+}VZ{+}V{+}b\bar{b}$ (blue) for the linear (left) and linear + quadratic (right) parametrisation.

5.9 Conclusion and outlook for the novel interpretation

This section presented a novel parametrisation of the diboson and V+heavy flavour backgrounds for the $VH, H\to b\bar{b}$ measurement within the SMEFT framework. It demonstrated that the spectra of several observables binned in transverse momentum of the vector boson for the VZ and $V+b\bar{b}$ process are not altered significantly from the SM prediction for $c_i = c_{\text{best fit}}\pm 1\sigma$. The effect of an operator per p_T^V bin can therefore be approximated as a normalisation effect, yet future studies should take potential shape effects into account. The simultaneous fit of the parameterised signal and background signal strengths to data does not impact the constraints on effective couplings that the measurement is sensitive to, for example $c_{Hq}^{(3)}$ and c_{Hu}, but improves the constraints significantly for couplings that were constrained less, like $c_{Hl}^{(1)}$or c'_{ll}. This is the case for operators that cause modifications to the SM cross-sections that are constant over p_T^V. No significant deviations with respect to the SM were observed, contrary, the best fit values of the effective coupling strengths tend to become closer to zero, corresponding to the SM prediction. The significant difference between the linear and linear + quadratic parametrisation were also seen for the improved SMEFT interpretation, considering the quadratic contributions to the VZ and $V+b\bar{b}$ processes reduced degeneracy. Furthermore, the background parametrisation is shown to alter the correlation between pairs of operators and reduce the 2D confidence contours. The next step is a full likelihood fit considering all systematics to validate the χ^2-fit approach. Moreover, the SMEFT effects on the backgrounds should be simulated on reconstruction level including a full detector simulation. The proof-of-concept neglected modifications to the Higgs boson decay as they were shown to not contribute significantly by the $VH, H\to b\bar{b}$ analysis, however they should be considered in future studies for completeness.

This thesis presents the novel approach of constraining Wilson coefficients for the $VH, H\to b\bar{b}$ measurement through a simultaneous interpretation of the VH signal and two backgrounds with the same final state. The work is intended as a proof-of-concept and is thus far from providing a fully comprehensive treatment of the new approach. The following considerations should be taken account for future studies additionally:

5.9.1 Other backgrounds

The study was started by considering irreducible backgrounds. The next step is to extend the interpretation to additional the backgrounds, for example backgrounds that involve a top-quark, namely the $t\bar{t}$ production and single top-quark production. Both processes have a significant larger cross-section than the signal. However, the typical SMEFT interpretation of processes involving top quarks assume that given its large mass, the top-quark might couple differently to new physics. Thus, these interpretations do not assume the same global $\mathrm{SU}(3)^5$ symmetry, hypothesising equal coupling of new physics to all quark and lepton generations, and therefore require different operators than constrained in this thesis. Additionally, the interpretation should be extended to the QCD multi-jet background.

5.9.2 p_T^V binning

The combined $VH, H\to b\bar{b}$ analysis demonstrated that the effective couplings can be constrained better by measuring the signal strength in as many bins as possible. The same behaviour is expected for the simulatenous interpretation of the two irreducible backgrounds. The increased data set allows for a successively finer binning. For example, the Higgs STXS framework foresees a split of the p_T^V bins in zero jets, one jets and two or more jets. A preliminary study on the effects on the additional binning in jet multiplicity is ongoing.

5.9.3 Difference between linear and linear + quadratic parametrisation

A significant difference between the the confidence intervals for the linear and the linear + quadratic parametrisation is observed for both, a fit to VH, but also for an interpretation of two backgrounds, VH+VZ and VH+VZ+ V+hf. The differences can occur for a multitude of reasons as explained in Section 2. They might hint to a breakdown of the SMEFT approach, as the Lagrangian expansion is expected to only work reasonably for sufficiently small deviations. This might not be the case for operators that introduce p_T^V-enhanced deviations. Furthermore, its is not known if the dimension 8 operators are sufficiently suppressed with respect to the dimension-6, since the energy scale of the new physics might be different. Thus far, it is not possible to construct and constrain a complete set of operators whose contributions to the cross-section are suppressed with Λ^{-4}.

5.9.4 Ongoing combination efforts

The considered Wilson coefficients have been constrained across measurements before [49]. Ongoing efforts constrain the effective couplings from multiple measurements of the Higgs boson in different production and decay modes but also with electroweak precision measurements, top and diboson measurements. So far, the combination solely parameterises the signal of each measurement in terms of new physics. This study showed showed the effects from consistently parameterising the signal and the (main) backgrounds for the $VH, H \to b\bar{b}$ measurements. The effects can be further correlated among different measurements and improve the combined interpretations by constraining the effective coupling of an operator in any process that is affected by it, since one measurement signal is another one's background.

6 Summary

The Standard Model (SM) predictions for elementary particles and their interactions on small scales are thoroughly tested with high precision up to high energies. The most recent success of the theory was the discovery of the Higgs boson in 2012 by two experiments at the LHC, ATLAS and CMS.

Nonetheless, observational mysteries like dark matter demonstrate that the SM is not a complete "theory of everything." In the absence of the discovery of new particles with the ATLAS 139 fb^{-1} Run 2 data set at $\sqrt{s} = 13\,\mathrm{TeV}$, indirect measurement techniques for new physics have been employed. The SMEFT approach interprets the SM Lagrangian as a low energy manifestation of a more complete theory at a higher energy scale. This model-independent approach allows the constraint of the coupling strength of effective, low-energy interactions of a new theory at high energy, without requiring assumptions on its detailed structure.

This thesis studied a SMEFT interpretation of the $VH, H\to b\bar{b}$ analysis which measures Higgs bosons decaying into b-quark pairs that are produced in association with a leptonically decaying vector boson (V=W, Z). The published $VH, H\to b\bar{b}$ analysis featured a SMEFT interpretation of the measurement. The interpretation was however restricted to a parameterisation of only the signal as a function of the effective coupling strengths of dimension 6 SMEFT operators, referred to as Wilson coefficients, and neglected the effect of the same operators on the backgrounds of the analysis. For the first time, this thesis parameterises two main backgrounds, diboson (VZ) and V in association with two b-quarks (V+$b\bar{b}$) production. The constraints on the Wilson coefficients are extracted from a simultaneous fit of the signal strengths of VH, VZ and V+hf binned by the vector boson transverse momentum p_T^V.

This thesis showed that for operators to which the VH signal is particular sensitive, the constraints on the Wilson coefficients do not get significantly altered when considering the VZ and V+$b\bar{b}$ parametrisation. In addition, the inclusion of SMEFT effects on the backgrounds allows to significantly improve the constraints of additional Wilson coefficients to which the measurement was not sensitive before.

An extensive refurbishment campaign recommissioned ATLAS for LHC Run 3 to record more collisions with higher precision and at a higher collision energy in the coming years. The thesis describes safety-critical contributions to the delicate beam-pipe evacuation procedure and the standardisation of the cavern ventilation system across the ATLAS and CMS experiment. The increasing dataset will allow to increase the measurement precision of many analyses. Therefore, the SMEFT interpretations will reach precision levels at which a proper SMEFT parametrisation of the backgrounds cannot be neglected anymore. The consistent treatment of signal and background interpretation will be especially important for the combination of several measurements as the effects are correlated across different processes.

References

[1] G. Aad et al. "Observation of a new particle in the search for the Standard Model Higgs boson with the ATLAS detector at the LHC". In: *Physics Letters B* 716.1 (Sept. 2012), pp. 1–29. ISSN: 0370-2693. DOI: 10.1016/j.physletb.2012.08.020. URL: http://dx.doi.org/10.1016/j.physletb.2012.08.020.

[2] S. Chatrchyan et al. "Observation of a new boson at a mass of 125 GeV with the CMS experiment at the LHC". In: *Physics Letters B* 716.1 (Sept. 2012), pp. 30–61. ISSN: 0370-2693. DOI: 10.1016/j.physletb.2012.08.021. URL: http://dx.doi.org/10.1016/j.physletb.2012.08.021.

[3] D. de Florian et al. *Handbook of LHC Higgs Cross Sections: 4. Deciphering the Nature of the Higgs Sector*. CERN Yellow Reports: Monographs. 869 pages, 295 figures, 248 tables and 1645 citations. Working Group web page: https://twiki.cern.ch/twiki/bin/view/LHCPhysics/LHCHXSWG. Geneva: CERN, Oct. 2016. DOI: 10.23731/CYRM-2017-002. URL: https://cds.cern.ch/record/2227475.

[4] Nicolas Berger et al. *Simplified Template Cross Sections - Stage 1.1*. 2019. DOI: 10.48550/ARXIV.1906.02754. URL: https://arxiv.org/abs/1906.02754.

[5] The ATLAS Collaboration. "The ATLAS Experiment at the CERN Large Hadron Collider". In: *Journal of Instrumentation* 3.08 (Aug. 2008), S08003–S08003. DOI: 10.1088/1748-0221/3/08/s08003. URL: https://doi.org/10.1088/1748-0221/3/08/s08003.

[6] Lyndon Evans and Philip Bryant. "LHC Machine". In: *Journal of Instrumentation* 3.08 (Aug. 2008), S08001–S08001. DOI: 10.1088/1748-0221/3/08/s08001. URL: https://doi.org/10.1088/1748-0221/3/08/s08001.

[7] M Capeans et al. *ATLAS Insertable B-Layer Technical Design Report*. Tech. rep. Sept. 2010. URL: https://cds.cern.ch/record/1291633.

[8] T Kawamoto et al. *New Small Wheel Technical Design Report*. Tech. rep. ATLAS New Small Wheel Technical Design Report. June 2013. URL: https://cds.cern.ch/record/1552862.

[9] M. Mikuž et al. "Diamond pad detector telescope for beam conditions and luminosity monitoring in ATLAS". In: *Nuclear Instruments and Methods in Physics Research Section A: Accelerators, Spectrometers, Detectors and Associated Equipment* 579.2 (2007). Proceedings of the 6th "Hiroshima" Symposium on the Development and Application of Semiconductor Detectors, pp. 788–794. ISSN: 0168-9002. DOI: https://doi.org/10.1016/j.nima.2007.05.297. URL: https://www.sciencedirect.com/science/article/pii/S0168900207011849.

[10] G. Avoni et al. "The new LUCID-2 detector for luminosity measurement and monitoring in ATLAS". In: *Journal of Instrumentation* 13.07 (July 2018), P07017–P07017. DOI: 10.1088/1748-0221/13/07/p07017. URL: https://doi.org/10.1088/1748-0221/13/07/p07017.

[11] Rachel Avramidou and Laetitia Bardo. *SLIMOS Handbook*. CERN Internal. 2019. URL: https://edms.cern.ch/document/1890896/1.2.

[12] The ATLAS Collaboration. *ATLAS detector and physics performance: Technical Design Report, 1*. Technical design report. ATLAS. Geneva: CERN, 1999. URL: https://cds.cern.ch/record/391176.

[13] Emma Vigo Castellvi. *Study of the ventilation at ATLAS cavern UX15. Air velocity and temperature around the muon chambers*. CERN Internal. 2000. URL: https://cds.cern.ch/record/476676/files/st-2000-063.pdf.

[14] Adrien Ledeul et al. "REMUS: The new CERN Radiation and Environment Monitoring Unified Supervision". In: (2015), TUD3O03. 4 p. DOI: 10.18429/JACoW-ICALEPCS2015-TUD3O03. URL: https://cds.cern.ch/record/2213488.

[15] ICRP. "The 2007 Recommendations of the International Commission on Radiological Protection." In: *Annals of the IRCP* 103 (2007). URL: https://journals.sagepub.com/doi/pdf/10.1177/ANIB_37_2-4.

[16] O Beltramello et al. "The Detector Safety System of the ATLAS experiment". In: *Journal of Instrumentation* 4.09 (Sept. 2009), P09012–P09012. DOI: 10.1088/1748-0221/4/09/p09012. URL: https://doi.org/10.1088/1748-0221/4/09/p09012.

[17] The ATLAS Collaboration. *Screenshot of the ATCES safety diagram*. Accessed 25 March 2022. CERN Internal. URL: https://atlas-expert-system.web.cern.ch/login/simulator.php?page=safety&uid=ESD2_1D&lang=en.

[18] Aleksandra Wardzinska et al. "The Evolution of CERN EDMS". In: *J. Phys.: Conf. Ser.* 664 (2015), 032032. 8 p. DOI: 10.1088/1742-6596/664/3/032032. URL: https://cds.cern.ch/record/2134549.

[19] Ignacio Asensi Tortajada et al. *ATLAS technical coordination expert system*. Tech. rep. Geneva: CERN, Nov. 2018. DOI: 10.1051/epjconf/201921405035. URL: https://cds.cern.ch/record/2648869.

[20] A Barriuso Poy et al. "The detector control system of the ATLAS experiment". In: *Journal of Instrumentation* 3.05 (May 2008), P05006–P05006. DOI: 10.1088/1748-0221/3/05/p05006. URL: https://doi.org/10.1088/1748-0221/3/05/p05006.

[21] S Karppinen et al. "Design of Beampipes for LHC Experiments". In: *Vacuum* 64 (July 2003), 476–473. 12 p. URL: https://cds.cern.ch/record/631307.

[22] Giuseppe Bregliozzi. "Neon Venting of Activated NEG Beam Pipes in the CERN LHC Long Straight Sections without Losing Vacuum Performance". In: *Particle Accelerator Conference (PAC 09)*. 2010, MO6RFP006.

[23] Oswald Gröbner. "LHC vacuum system". In: (1999). DOI: 10.5170/CERN-1999-005.291. URL: https://cds.cern.ch/record/455985.

[24] P. Manini and E. Maccallini. *NEG pumps: Sorption mechanisms and applications*. 2020. DOI: 10.48550/ARXIV.2006.01537. URL: https://arxiv.org/abs/2006.01537.

[25] R Veness. *ATLAS BEAM VACUUM SYSTEM INTERFACES*. Tech. rep. Geneva: CERN, Apr. 2008. URL: https://cds.cern.ch/record/1095479.

[26] Josef Sestak. *Bake-out procedure, ATLAS readiness review for Beam pipe bake-out*. https://indico.cern.ch/event/1098883/contributions/4623770/attachments/2369663/4051455/Readiness_review_for_Beam_pipe_bake-out_20220112_v0_pptx_cpdf.pdf. 12 January 2022, CERN Internal. Accessed: 1 May 2022. 2022.

[27] The ATLAS Collaboration. *ATLAS Vacuum layout Q1/Q1*. https://edms.cern.ch/document/943475. CERN EDMS 943475. Accessed 20 January 2022. 2014.

[28] The ATLAS Collaboration. *Screenshot of the ATCES bakeout diagram*. Accessed 17 May 2022. CERN Internal. URL: https://atlas-expert-system.web.cern.ch/login/simulator.php?page=bakeOut&uid=Cooling_BakeOut_VA&lang=en.

[29] Florian Haslbeck et al. *Detector safety during the bake-out process of the beam pipe, ATC-TY-EY-0895*. https://edms.cern.ch/document/2680608/. CERN Internal. Accessed: 1 May 2022. 2022.

[30] Sascha Schmeling et al. "The detector safety system for LHC experiments". In: *IEEE Trans. Nucl. Sci.* 51 (2004), pp. 521–525. DOI: 10.1109/TNS.2004.828631. URL: https://cds.cern.ch/record/816785.

[31] The ATLAS Collaboration. *Thermal analysis of the ambient air around a particle detector*. Tech. rep. Geneva: CERN, Jan. 2003. URL: https://cds.cern.ch/record/621748.

[32] Florian Haslbeck et al. *Ventilation panel in ATLAS*. CERN Internal. 2022. URL: https://edms.cern.ch/document/2684305/1.

[33] Sheila M Goodman et al. "Scalable manufacturing of fibrous nanocomposites for multifunctional liquid sensing". In: *Nano Today* 40 (2021), 101270. 8 p. DOI: 10.1016/j.nantod.2021.101270. URL: https://cds.cern.ch/record/2783178.

[34] Ignacio Asensi Tortajada. "Design and Development of Safety and Control Systems in ATLAS". Presented 09 Nov 2021. Sept. 2021. URL: https://cds.cern.ch/record/2791748.

[35] Ken Mimasu, Verónica Sanz, and Ciaran Williams. "Higher order QCD predictions for associated Higgs production with anomalous couplings to gauge bosons". In: *Journal of High Energy Physics* 2016.8 (Aug. 2016). DOI: 10.1007/jhep08(2016)039. URL: https://doi.org/10.1007%2Fjhep08%282016%29039.

[36] Brian Moser. "The Beauty and the Boost: a Higgs Boson Tale - Measurements of Higgs Boson Production at High Energy in Decays to Bottom Quarks and Their Interpretations with the ATLAS Experiment at the LHC". Presented 04 Mar 2022. 2021. URL: https://cds.cern.ch/record/2803776.

[37] S Heinemeyer et al. *Handbook of LHC Higgs Cross Sections: 3. Higgs Properties: Report of the LHC Higgs Cross Section Working Group*. Ed. by S Heinemeyer. CERN Yellow Reports: Monographs. Comments: 404 pages, 139 figures, to be submitted to CERN Report. July 2013. DOI: 10.5170/CERN-2013-004. URL: https://twiki.cern.ch/twiki/bin/view/LHCPhysics/CrossSections.

[38] *Measurements of WH and ZH production in the $H \to b\bar{b}$ decay channel in pp collisions at 13 TeV with the ATLAS detector*. Tech. rep. All figures including auxiliary figures are available at https://atlas.web.cern.ch/Atlas/GROUPS/PHYSICS/CONFNOTES/ATLAS-CONF-2020-006. Geneva: CERN, Apr. 2020. URL: https://cds.cern.ch/record/2714885.

[39] The ATLAS Collaboration. "Measurement of the associated production of a Higgs boson decaying into b-quarks with a vector boson at high transverse momentum in pp collisions at $\sqrt{s} = 13$ TeV with the ATLAS detector". In: *Physics Letters B* 816 (May 2021), p. 136204. DOI: 10.1016/j.physletb.2021.136204. URL: https://doi.org/10.1016%2Fj.physletb.2021.136204.

[40] *Combination of measurements of Higgs boson production in association with a W or Z boson in the $b\bar{b}$ decay channel with the ATLAS experiment at $\sqrt{s} = 13$ TeV*. Tech. rep. All figures including auxiliary figures are available at https://atlas.web.cern.ch/Atlas/GROUPS/PHYSICS/CONFNOTES/ATLAS-CONF-2021-051. Geneva: CERN, Sept. 2021. URL: https://cds.cern.ch/record/2782535.

[41] B. Grzadkowski et al. "Dimension-six terms in the Standard Model Lagrangian". In: *Journal of High Energy Physics* 2010.10 (Oct. 2010). DOI: 10.1007/jhep10(2010)085. URL: https://doi.org/10.1007%2Fjhep10%282010%29085.

[42] Johann Brehmer et al. “Benchmarking simplified template cross sections in WH production”. In: *Journal of High Energy Physics* 2019.11 (Nov. 2019). DOI: 10.1007/jhep11(2019)034. URL: https://doi.org/10.1007%2Fjhep11%282019%29034.

[43] Giulia Di Gregorio. “Search for the Higgs boson produced in association with a vector boson and decaying into a pair of b-quarks using large-R jets with the ATLAS detector”. Presented 23 Mar 2021. Dec. 2020. URL: https://cds.cern.ch/record/2759132.

[44] Johan Alwall et al. “MadGraph 5: going beyond”. In: *Journal of High Energy Physics* 2011.6 (June 2011). DOI: 10.1007/jhep06(2011)128. URL: https://doi.org/10.1007%2Fjhep06%282011%29128.

[45] Ilaria Brivio, Yun Jiang, and Michael Trott. “The SMEFTsim package, theory and tools”. In: *Journal of High Energy Physics* 2017.12 (Dec. 2017). DOI: 10.1007/jhep12(2017)070. URL: https://doi.org/10.1007%2Fjhep12%282017%29070.

[46] Torbjörn Sjöstrand et al. “An introduction to PYTHIA 8.2”. In: *Computer Physics Communications* 191 (June 2015), pp. 159–177. DOI: 10.1016/j.cpc.2015.01.024. URL: https://doi.org/10.1016%2Fj.cpc.2015.01.024.

[47] Christian Bierlich et al. “Robust Independent Validation of Experiment and Theory: Rivet version 3”. In: *SciPost Physics* 8.2 (Feb. 2020). DOI: 10.21468/scipostphys.8.2.026. URL: https://doi.org/10.21468%2Fscipostphys.8.2.026.

[48] *Methodology for EFT interpretation of Higgs boson Simplified Template Cross-section results in ATLAS*. Tech. rep. All figures including auxiliary figures are available at https://atlas.web.cern.ch/Atlas/GROUPS/PHYSICS/PUBNOTES/ATL-PHYS-PUB-2019-042. Geneva: CERN, Oct. 2019. URL: https://cds.cern.ch/record/2694284.

[49] *Combined measurements of Higgs boson production and decay using up to* 139 *fb*$^{-1}$ *of proton-proton collision data at* $\sqrt{s} = 13$ *TeV collected with the ATLAS experiment*. Tech. rep. All figures including auxiliary figures are available at https://atlas.web.cern.ch/Atlas/GROUPS/PHYSICS/CONFNOTES/ATLAS-CONF-2021-053. Geneva: CERN, Nov. 2021. URL: https://cds.cern.ch/record/2789544.

[50] Kerstin Lantzsch. *Beam pipe heaters trend (ATLAS Log-book)*. CERN Internal. Feb. 2022. URL: https://atlasop.cern.ch/elisa/display/441799?logbook=ATLAS.

A Appendix

A.1 Safety contributions

Bake-Out	O_COL_BeamPipe_VJA_CoolingSwitch	O_COL_BeamPipe_VJC_CoolingSwitch	O_COL_IBL_CO2_PlantA_WarmMode_FCTIR00092	O_COL_IBL_CO2_PlantA_WaterInterlock_FCK0013	O_COL_IBL_CO2_PlantB_WarmMode_FCTIR00093	O_COL_IBL_CO2_PlantB_WaterInterlock_FCK0013	O_COL_IBL_CO2_Vacuum_PumpInterlock_FCTIR00	O_COL_IDE_PlantFCTIR00038_STOP	O_COL_IDE_PlantFCTIR00038_Standby	O_INF_BakeOut_Interlock_Y6023X0	O_INF_PIX_IBL_Power_Y2407A2	O_INF_PIX_Power_Y0414S2	O_INF_PIX_Power_Y1114A2	O_INF_PIX_Power_Y1314A2	O_INF_PIX_Power_Y1514A2	O_INF_Power_EXD203
AL_COL_BeamPipe_VA_ChillerFailure										0						
AL_COL_BeamPipe_VJA_ChillerFailure	0															
AL_COL_BeamPipe_VJA_CoolingNotRunning										0						
AL_COL_BeamPipe_VJC_ChillerFailure		0														
AL_COL_BeamPipe_VJC_CoolingNotRunning										0						
AL_COL_Cables_CoolingFailure																
AL_COL_IBL_CO2_CoolingNotReady										0						
AL_COL_IBL_CO2_CoolingNotRunning										0						
AL_COL_IBL_CO2_PlantA_NOTinBakeOutMode										0						
AL_COL_IBL_CO2_PlantB_NOTinBakeOutMode										0						
AL_Emergency_ATLAS_OFF			0		0				0	0	300	0	0	0	0	10
AL_INF_BakeOut_EmergencyStop										0						
AL_INF_Power_US15_EOD2_UPSFailure									0							
AL_INF_Power_US15_ESS107_UPSonBattery									0							
AL_INF_Power_USA15_EOD2_UPSFailure									0							
AL_INF_Power_USA15_UPSonBattery									0							
AL_INF_RackCoolingFailure_US15												600				
AL_INF_RackCoolingFailure_USA15														600		
AL_INF_Smoke_US15_2ofLevels0_1_3									0			300				
AL_INF_Smoke_US15_Level2_Ceiling									0			300				
AL_INF_Smoke_US15_Level2_Floor									0			300				
AL_INF_Smoke_USA15L1_CVRoom								0								
AL_INF_Smoke_USA15L1_RackRoomSideC									0							
AL_INF_Smoke_USA15L2_RackRoom			0		0				0		300		300	300	300	
AL_INF_Smoke_USA15L3_CVArea			0		0					0						
AL_INF_Smoke_USA15_2Areas			0		0			360	0	0	600		300	300	300	
AL_INF_Smoke_UX15			0		0		300		0	0						10
AL_INF_US15_Flooding								360	0	0		300				
AL_INF_USA15andUX15_Flooding			0		0			360	0	0	600	300	300	300	300	10
AL_INF_WaterLeak_IBL_CO2Cooling_PlantA				0												
AL_INF_WaterLeak_IBL_CO2Cooling_PlantB						0										
AL_LUC_TempTooHigh_SideA										0						
AL_LUC_TempTooHigh_SideC										0						
AL_MAG_BT_VesselVacuumFailure									0							
AL_MAG_ECTA_VesselVacuumFailure									0							
AL_MAG_ECTC_VesselVacuumFailure									0							
AL_PIX_IBL_Temperature_Interlock										0						
AL_PIX_Temperature_Interlock										0						
AL_SN2_Smoke_InnerDetectorA									0	0						
AL_SN2_Smoke_InnerDetectorC									0	0						
AL_SN3_FG_EIL4_SW_2Alarms									0							
AL_SN3_Smoke_BWA_and_BWC									0	0						10
AL_SN3_Smoke_CentralTrench									0	0						10
AL_SN3_Smoke_InnerArea_and_BWA									0	0						10
AL_SN3_Smoke_InnerArea_and_BWC									0	0						10
AL_SN3_Smoke_InnerArea_and_MuonBarrel									0	0						10
AL_SN3_Smoke_InnerDetector									0	0						
AL_SN3_Smoke_MUN_MuonBarrel_InnerArea									0							
AL_SN3_Smoke_MacroArea_BWA_2alarms									0	0						10
AL_SN3_Smoke_MacroArea_BWC_2alarms									0	0						10
AL_SN3_Smoke_MacroArea_InnerArea									0							
AL_SN3_Smoke_MacroArea_InnerArea_2alarms									0	0						10
AL_SN3_Smoke_MacroArea_MuonBarrel									0							
AL_SN3_Smoke_MacroArea_MuonBarrel_2alarms									0	0						10
AL_SN3_Smoke_MuonBarrel_and_BWA									0	0						10
AL_SN3_Smoke_MuonBarrel_and_BWC									0	0						10
AL_SN3_Smoke_PixelBoxes_PP2																
AL_Smoke_IDE_Y2721A2									0							
AL_Smoke_IDE_Y2821A1									0							
AL_Smoke_MUN_Y3723X0																10
AL_Smoke_MUN_Y3823X0																10
AL_Smoke_MUN_Y5023X0																10
AL_Smoke_MUN_Y5123X0																10
AL_Smoke_MUN_Y5823X0																10
AL_Smoke_PIX_Y0314S2												0				
AL_Smoke_PIX_Y0414S2												0				
AL_Smoke_PIX_Y1314A2														0	0	
AL_Smoke_PIX_Y1414A2														0	0	
AL_Smoke_PIX_Y1514A2															0	

Table 5: Default DSS AAM cropped to represent the systems relevant for the beam pipe bake-out, showing the alarms ("AL") and the associated action ("O"), with the delay in seconds. The changes for the bake-out are marked in red.

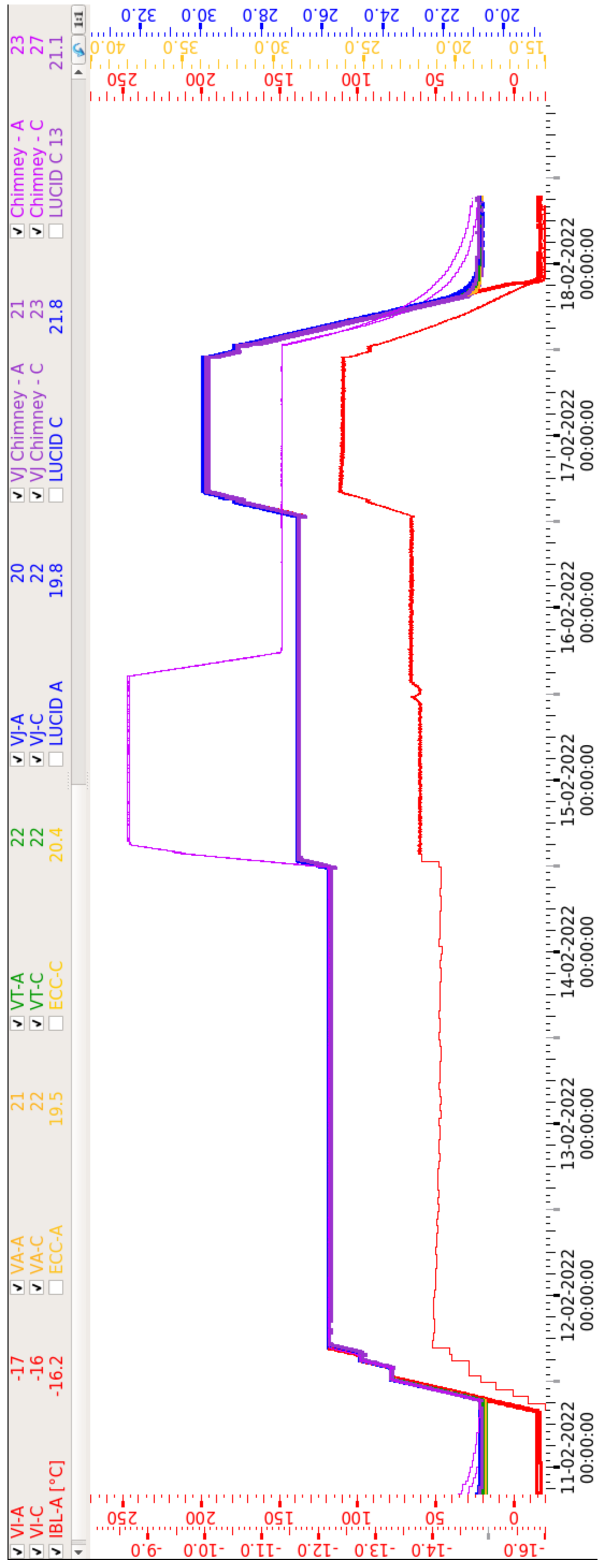

Figure 31: Beam pipe heaters trend. Modified from [50].

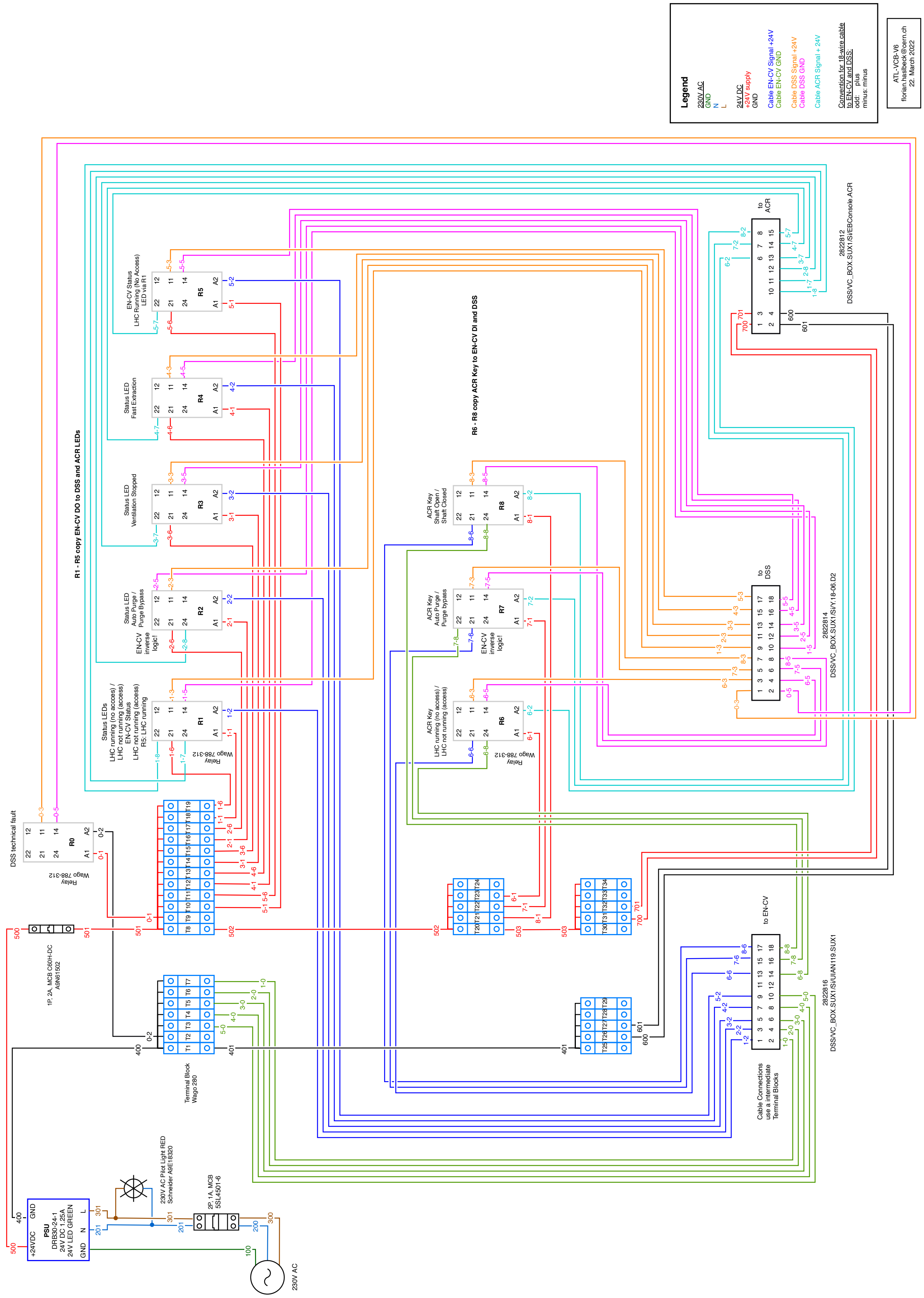

Figure 32: Electric schematics for the signal handling switch board (VCB).

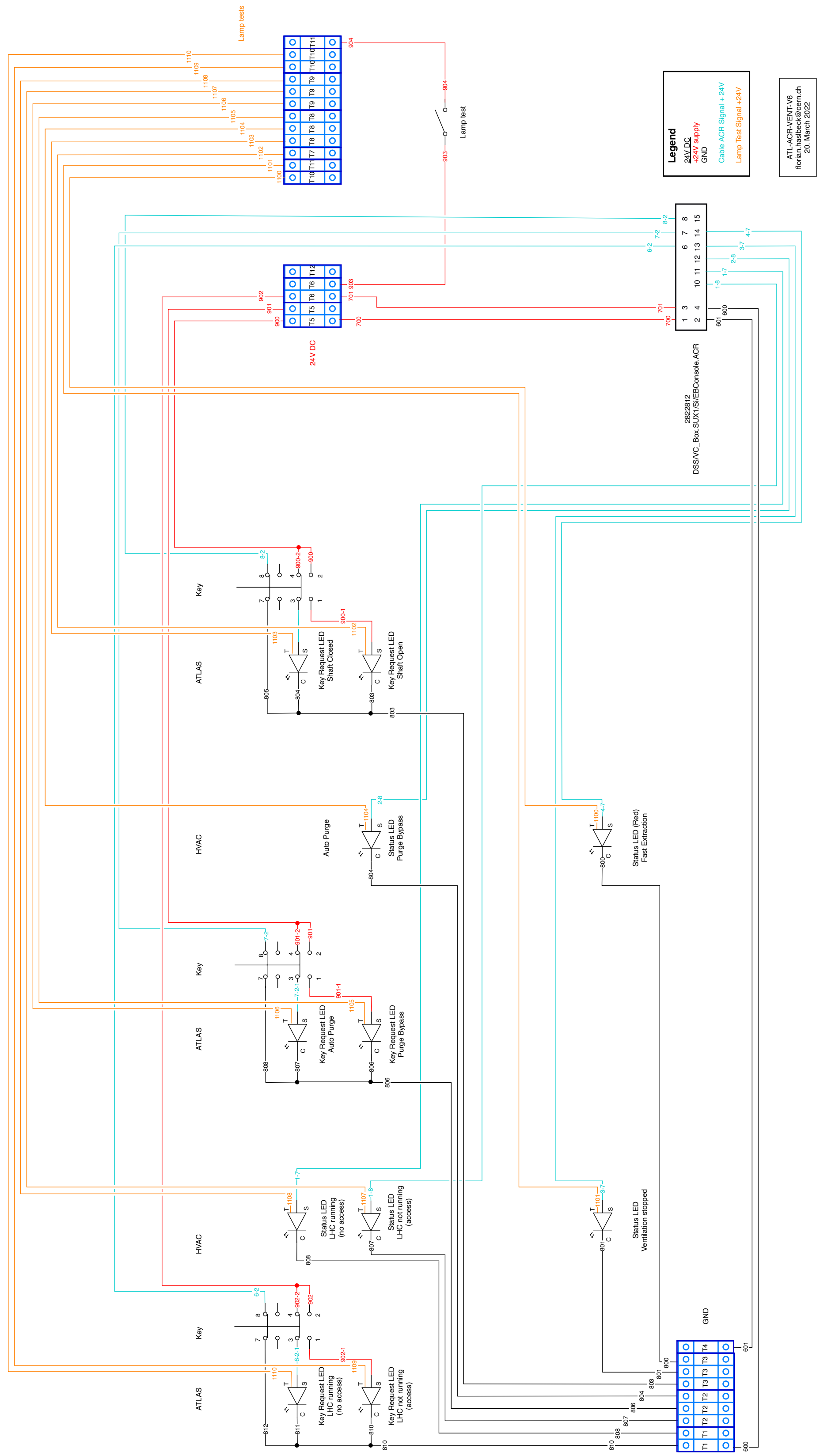

Figure 33: Electric schematic for the ACR ventilation panel.

Figure 34: ACR SLIMOS hardware panel, showing the emergency buttons, MAD, PAD, patrol kets and the new ventilation panel.

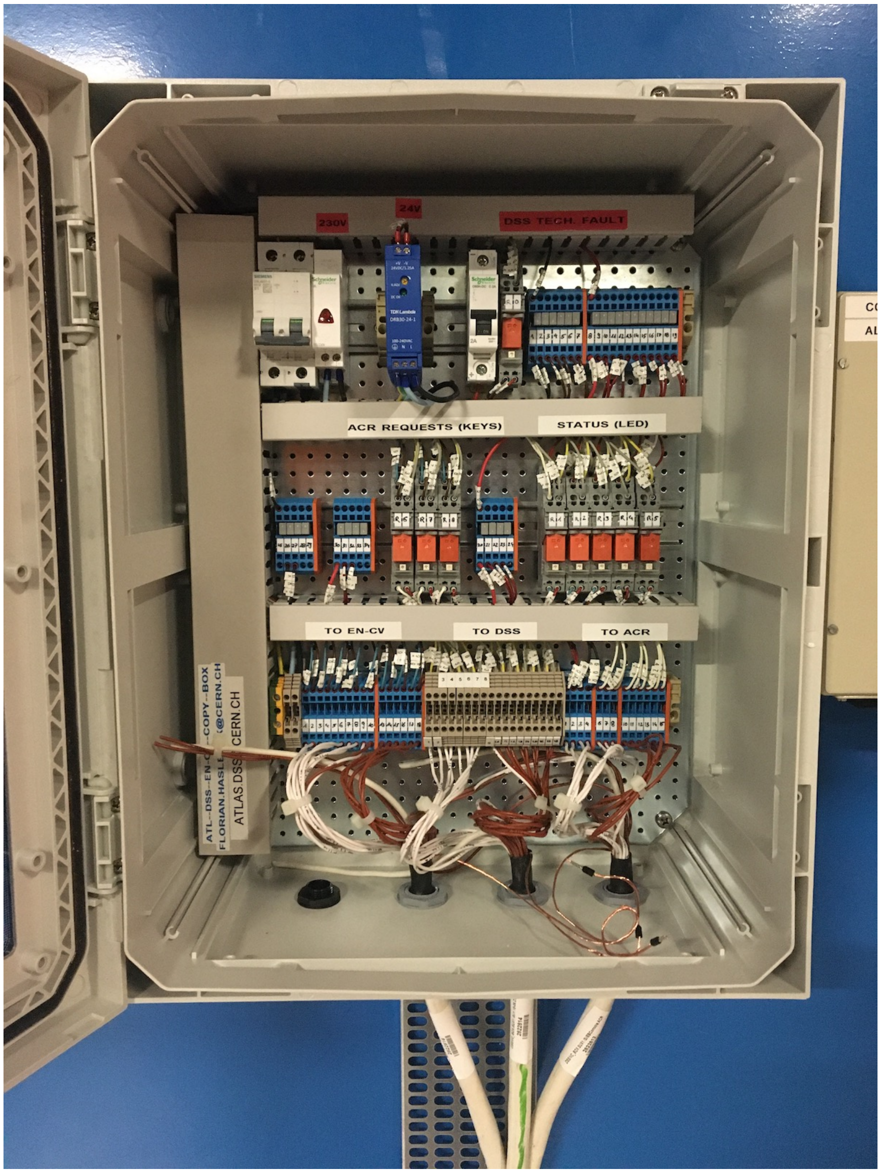

Figure 35: Switch board VCB mounted on the wall of 3182/R-002.

A.2 Combined SMEFT interpretation

A.2.1 VH VZ

	linear		quadratic		linear		quadratic	
	b1	b2	b1	b2	b1	b2	b1	b2
	$c_{Hq}^{(3)}$				$c_{Hq}^{(1)}$			
WH	8.3	23	20	205				
ZH	7.6	20	19	179	-0.9434	-3.8900	18	180
WZ	2.2	4.7	4.4	37	0.1646	0.1580	0.0196	0.0183
ZZ	0.4463	0.3997	0.0505	0.0524	0.1565	0.1314	0.0306	0.0270
WBB	0.1162	0.1227	0.0036	0.0036				
ZBB	0.1328	0.1121	0.0049	0.0042	0.1273	0.1044	0.0052	0.0043
	c_{Hu}				c_{Hd}			
WH								
ZH	1.8	5.0	11	118	-0.5731	-1.4670	7.4	61
WZ			0.0147	0.0147	-0.0223	-0.0214	0.0049	0.0047
ZZ	0.0107	0.0111	0.0022	0.0023	-0.0244	-0.0248	0.0054	0.0051
WBB								
ZBB	0.0025	0.0040	0.0002	0.0003	-0.0234	-0.0201	0.0046	0.0043
	c_{HDD}				c_{HWB}			
WH	-0.0305	-0.0317						
ZH	0.0120	0.0153	0.0048	0.0046	0.4929	0.517	0.2218	0.546
WZ	0.0253	0.0235	0.0152	0.0140	0.1263	0.1309	0.0167	0.0364
ZZ	0.0255	0.0228	0.0053	0.0054	0.1570	0.1431	0.0120	0.0104
WBB								
ZBB	-0.0232	-0.0236	0.0036	0.0024	0.0377	0.0352	0.0044	0.0037
	$c_{Hl}^{(1)}$				$c_{Hl}^{(3)}$			
WH					-0.2405	-0.2330	0.0159	0.0171
ZH	-0.0347	-0.0372	0.0064	0.0078	-0.2317	-0.2386	0.0163	0.0164
WZ					-0.3757	-0.3312	0.0337	0.0310
ZZ	-0.0351	-0.0263	0.0050	0.0046	-0.3486	-0.3571	0.0338	0.0356
WBB					-0.1203	-0.1089	0.0036	0.0036
ZBB	-0.0343	-0.0266	0.0050	0.0041	-0.1195	-0.1256	0.0043	0.0032

	linear		quadratic		linear		quadratic	
	b1	b2	b1	b2	b1	b2	b1	b2
		c'_{ll}						
WH	0.1854	0.1883	0.0084	0.0083				
ZH	0.1835	0.1895	0.0082	0.0086				
WZ	0.2351	0.2100	0.0143	0.0132				
ZZ	0.2435	0.2230	0.0152	0.0143				
WBB	0.1198	0.1152	0.0036	0.0036				
ZBB	0.1156	0.0835	0.0038	0.0029				

Table 6: Linear and quadratic parametrisation. b1 : $p_T^V \in [250, 400]$ GeV, b2 : $p_T^V \in [400, \infty)$ GeV

Process	MadGraph commands				diagram filter
WH	$pp \to H\, l^+\nu$		$pp > H\, l^-\bar{\nu}$		
ZH	$qq \to H\, l^+l^-$	$/\gamma$	$qq \to H\, \nu\bar{\nu}$	$/\gamma$	
WZ	$pp \to ZW^+ \to l^+\nu\, b\bar{b}$		$pp \to ZW^- \to l^-\bar{\nu}\, b\bar{b}$		
ZZ	$pp \to ZZ \to l^+l^-\, b\bar{b}$	$/\gamma H$	$pp \to ZZ \to \nu\bar{\nu}\, b\bar{b}$	$/\gamma H$	✓
$W{+}b\bar{b}$	$pp \to l^+\nu\, b\bar{b}$	$/\gamma H Z t$	$pp \to l^-\bar{\nu}\, b\bar{b}$	$/\gamma H Z t$	
$Z{+}b\bar{b}$	$pp \to l^+l^-\, b\bar{b}$	$/\gamma H$	$pp \to \nu\bar{\nu} b\bar{b}$	$/\gamma H$	✓

Table 7: MadGraph commands used for the event generation.

	WH		ZH		WZ		ZZ		W+Jets		Z+Jets	
	σ [nb]	$\frac{\sigma_{int}}{\sigma_{SM}}$ [%]	σ [nb]	$\frac{\sigma_{int}}{\sigma_{SM}}$ %	σ [nb]	$\frac{\sigma_{int}}{\sigma_{SM}}$ [%]	σ [nb]	$\frac{\sigma_{int}}{\sigma_{SM}}$ [%]	σ [nb]	$\frac{\sigma_{int}}{\sigma_{SM}}$ [%]	σ [nb]	$\frac{\sigma_{int}}{\sigma_{SM}}$ [%]
SM	393		190		174		119		1133		9966	
$\mathcal{O}_{HDD}$	-1.19	-0.30	0.25	0.1	0.42	0.2	0.27	0.2			-23.5	-0.2
$\mathcal{O}_{Hl}^{(3)}$	-9.49	-2.42	-4.53	-2.4	-6.42	-3.7	-4.29	-3.6	-13.7	-1.2	-115.8	-1.2
$\mathcal{O}_{Hq}^{(3)}$	75.7	19.27	35.2	18.5	9.60	5.5	5.28	4.4	13.7	1.2	136.8	1.4
O'_{ll}	7.14	1.82	3.46	1.8	4.17	2.4	2.90	2.4	13.7	1.2	119.5	1.2
$\mathcal{O}_{HWB}$			7.37	3.9	1.68	1.0	1.83	1.5			38.6	0.4
$\mathcal{O}_{Hl}^{(1)}$			-0.69	-0.4	-0.0029	0.0	-0.43	-0.4			-35.6	-0.4
$\mathcal{O}_{Hq}^{(1)}$			-2.69	-1.4	3.01	1.7	2.16	1.8			131.1	1.3
$\mathcal{O}_{Hu}$			7.98	4.2			0.12	0.1			1.20	0.0
$\mathcal{O}_{Hd}$			-2.84	-1.5	-0.40	-0.2	-0.29	-0.2			-23.1	-0.2

Table 8: Average cross section for various operators for the linear interaction term and the SM process. The average is taken from 20 independent generations of each 10000 events generated with MadGraph and Pythia. One vector boson always decays leptonically, for two, the Z decays to to two b-quarks. The Higgs does not decay as the small width approximation is applied. Jets means two b-quarks.

Wilson coefficient	Linear parametrisation χ^2 fit	Log-likelihood fit
	68% confidence limit	
$c_{Hq}^{(3)}$	[-0.035, 0.014]	[-0.031, 0.024]
c_{Hu}	[-0.34, -0.015]	[-0.34, 0.0094
$c_{Hq}^{(1)}$	[0.005, 0.44]	[-0.038, 0.56]
c_{Hd}	[0.06, 1.14]	[-0.01, 1.2]
c_{HWB}	[-2.5, -0.22]	[-3.1, -0.017]
$c_{Hl}^{(3)}$	[-0.26, 2.9]	[-0.9, 2.8]
c'_{ll}	[-3.7, 0.34]	[-3.6, 1.2]
$c_{Hl}^{(1)}$	[3.3, 34]	[0.82, 25]
c_{HDD}	[-26, 8.6]	[-27, 11]
	95% confidence limit	
$c_{Hq}^{(3)}$	[-0.058, 0.037]	[-0.055, 0.055]
c_{Hu}	[-0.49, 0.14]	[-0.51, 0.21
$c_{Hq}^{(1)}$	[-0.21, 0.65]	[-0.38, 0.85]
c_{Hd}	[-0.47, 1.7]	[-0.69, 1.7]
c_{HWB}	[-3.5, 0.8]	[-4.2, 2]
$c_{Hl}^{(3)}$	[-1.8, 4.5]	[-3.2, 4.2]
c'_{ll}	[-5.7, 2.3]	[-5.5, 4.1]
$c_{Hl}^{(1)}$	[-11.7, 50]	[-14, 38]
c_{HDD}	[-43, 26]	[-47, 33]

Table 9: Comparison of the 68% and 95% confidence intervals from with a χ^2 fit and LLH fit for a linear parametrisation for VH for $p_T^V \in \{[250, 400), [400, \infty)\}$ GeV. The STXS bins LLH result are taken from Reference [39].

Wilson coefficient	Linear + quadratic parametrisation χ^2 fit	Log-likelihood fit
	68% confidence interval	
$c_{Hq}^{(3)}$	[-0.135, -0.066] $\cup$ [-0.039, 0.001]	[-0.14, -0.084] $\cup$ [-0.02, 0.006]
$c_{Hq}^{(1)}$	[-0.035, 0.06]	[-0.044, 0.07]
c_{Hu}	[-0.085, 0.033]	[-0.1, 0.043]
c_{Hd}	[-0.07, 0.1]	[-0.081 ,0.11]
c_{HWB}	[-1.4, 0.131]	[-2, 0.41]
c_{HDD}	[-7, 5]	[-8.6, 6.3]
$c_{Hl}^{(3)}$	[0.1, 3.7] $\cup$ [10.5, 15]	[-0.78, 3.7] $\cup$ [22, 27]
$c_{Hl}^{(1)}$	[-3, 8]	[-3, 10]
c'_{ll}	[-22, -18] $\cup$ [-4.7, 0.3]	[-4.4, 1.1]
	95% confidence interval	
$c_{Hq}^{(3)}$	[-0.15, 0.027]	[-0.16, 0.038]
$c_{Hq}^{(1)}$	[-0.067, 0.091]	[-0.085, 0.11]
c_{Hu}	[-0.12, 0.073]	[-0.15, 0.097]
c_{Hd}	[-0.12, 0.15]	[-0.15, 0.18]
c_{HWB}	[-2, 0.7]	[-7.1, 3.3]
c_{HDD}	[-12, 10]	[-14, 13]
$c_{Hl}^{(3)}$	[-1.5, 16]	[-2.7, 16] $\cup$ [17, 29]
$c_{Hl}^{(1)}$	[-7, 12]	[-8, 15]
c'_{ll}	[-24, 2.1]	[-16, -12] $\cup$ [-10, 3.7]

Table 10: Comparison of the 68% and 95% confidence intervals from with a χ^2 fit and LLH fit for a linear + quadratic parametrisation for VH for $p_T^V \in \{[250, 400), [400, \infty)\}$ GeV. The STXS bins LLH result are taken from Reference [39].

Linear parametrisation					
	VH		VH + VZ		
Name	c_i	68% CI	c_i	68% CI	RD CI
$c_{Hq}^{(3)}$	-0.010	[-0.034, 0.014]	-0.0096	[-0.033, 0.014]	1.5 %
$c_{Hq}^{(1)}$	0.23	[0.017, 0.45]	0.19	[-0.018, 0.40]	3.5 %
c_{Hu}	-0.19	[-0.35, -0.025]	-0.17	[-0.32, -0.0082]	1.4 %
c_{Hd}	0.64	[0.097, 1.2]	0.58	[0.048, 1.1]	1.0 %
c_{HWB}	-1.5	[-2.6, -0.35]	-1.3	[-2.3, -0.30]	10 %
c_{HDD}	-11	[-28, 7]	-5	[-14, 3.8]	49 %
$c_{Hl}^{(3)}$	1.4	[-0.24, 2.9]	0.48	[-0.22, 1.2]	56 %
$c_{Hl}^{(1)}$	20	[4.9, 36]	10	[1.6, 19]	46 %
c'_{ll}	-1.7	[-3.7, 0.32]	-0.77	[-1.8, 0.25]	49 %
	VH		VH + VZ		
Name	c_i	95% CI	c_i	95% CI	RD CI
$c_{Hq}^{(3)}$	-0.010	[-0.058, 0.037]	-0.0096	[-0.056, 0.037]	1.5 %
$c_{Hq}^{(1)}$	0.23	[-0.19, 0.66]	0.19	[-0.22, 0.61]	3.5 %
c_{Hu}	-0.19	[-0.50, 0.13]	-0.17	[-0.48, 0.15]	1.5 %
c_{Hd}	0.64	[-0.43, 1.7]	0.58	[-0.47, 1.6]	1.0 %
c_{HWB}	-1.5	[-3.6, 0.73]	-1.3	[-3.3, 0.67]	10 %
c_{HDD}	-11	[-45, 24]	-5	[-23, 12]	49 %
$c_{Hl}^{(3)}$	1.4	[-1.8, 4.5]	0.48	[-0.90, 1.9]	56 %
$c_{Hl}^{(1)}$	20	[-10, 51]	10	[-7, 27]	45 %
c'_{ll}	-1.7	[-6, 2.3]	-0.77	[-2.8, 1.2]	49 %

Table 11: χ^2-fit results for the linear parametrisation model for VH and $VH{+}VZ$ for $p_T^V{\in}[250, 400), [400, \infty)$ [GeV]. RD is the CI's relative difference $\mathrm{RD} = 1 - \frac{(VH+VZ)}{VH}$.

Linear + quadratic parametrisation					
	VH		VH + VZ		
Name	c_i	68% CI	c_i	68% CI	RD CL
$c_{Hq}^{(3)}$	-0.11	[-0.14, -0.071] $\cup$ [-0.032, -0.0003]	-0.11	[-0.13, -0.067] $\cup$ [-0.042, 0.0047]	-17 %
$c_{Hq}^{(1)}$	0.013	[-0.034, 0.058]	0.012	[-0.036, 0.059]	-2.3 %
c_{Hu}	-0.029	[-0.084, 0.031]	-0.028	[-0.085, 0.033]	-2.4 %
c_{Hd}	0.016	[-0.063, 0.093]	0.016	[-0.065, 0.095]	-2.2 %
c_{HWB}	-0.69	[-1.4, 0.10]	-0.71	[-1.4, 0.055]	4.2 %
c_{HDD}	-1.4	[-7, 4.7]	-1.4	[-6, 2.9]	25 %
$c_{Hl}^{(3)}$	13	[0.020, 3.6] $\cup$ [10, 15]	0.51	[-0.22, 1.4]	80 %
$c_{Hl}^{(1)}$	2.6	[-2.8, 8]	2.9	[-1.6, 7]	15 %
c'_{ll}	-1.8	[-22, -18] $\cup$ [-4.7, 0.30]	-0.81	[-2.1, 0.25]	76 %
	VH		VH + VZ		
Name	c_i	95% CI	c_i	95% CI	RD CL
$c_{Hq}^{(3)}$	-0.11	[-0.15, 0.027]	-0.11	[-0.15, 0.027]	0 %
$c_{Hq}^{(1)}$	0.013	[-0.066, 0.090]	0.012	[-0.068, 0.091]	-1.2 %
c_{Hu}	-0.029	[-0.12, 0.072]	-0.028	[-0.12, 0.074]	-1.2 %
c_{Hd}	0.016	[-0.12, 0.15]	0.016	[-0.12, 0.15]	-1.2 %
c_{HWB}	-0.69	[-2.0, 0.67]	-0.71	[-1.9, 0.63]	2.9 %
c_{HDD}	-1.4	[-12, 10]	-1.4	[-10, 6]	27 %
$c_{Hl}^{(3)}$	13	[-1.5, 16]	0.51	[-0.84, 2.4] $\cup$ [8, 11]	66 %
$c_{Hl}^{(1)}$	2.6	[-7, 12]	2.9	[-4.8, 11]	17 %
c'_{ll}	-1.8	[-24, 2.1]	-0.81	[-17, -14] $\cup$ [-3.5, 1.2]	70 %

Table 12: χ^2-fit results for the linear + quadratic parametrisation model for VH and $VH{+}VZ$ for $p_T^V \in [250, 400), [400, \infty)$ [GeV]. RD is the CI's relative difference $\mathrm{RD} = 1 - \frac{(VH+VZ)}{VH}$.

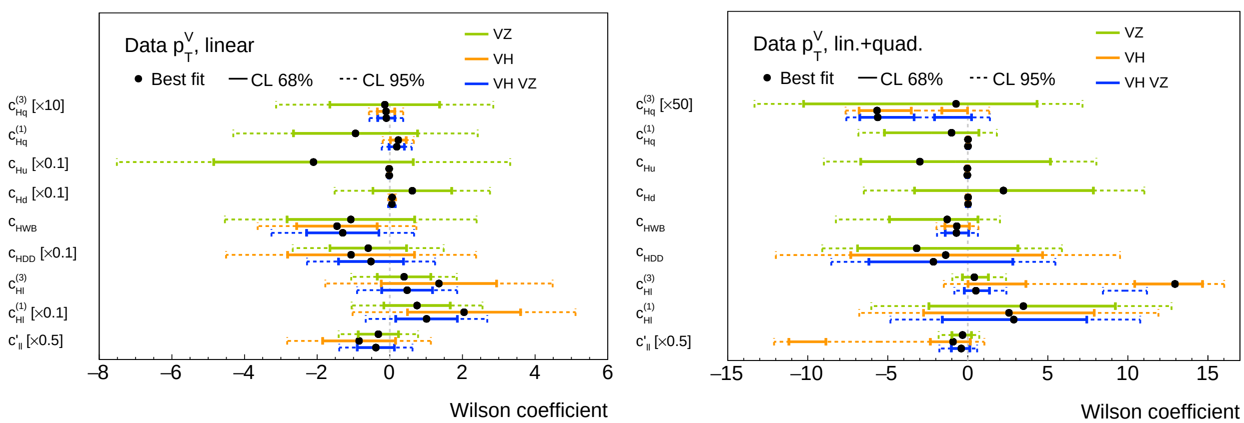

Figure 36: Comparison of χ^2 fit result for a linear (top) and linear + quadratic (bottom) parametrisation for VH and VZ and VH+VZ.

A.2.2 VH VZ VH+hf

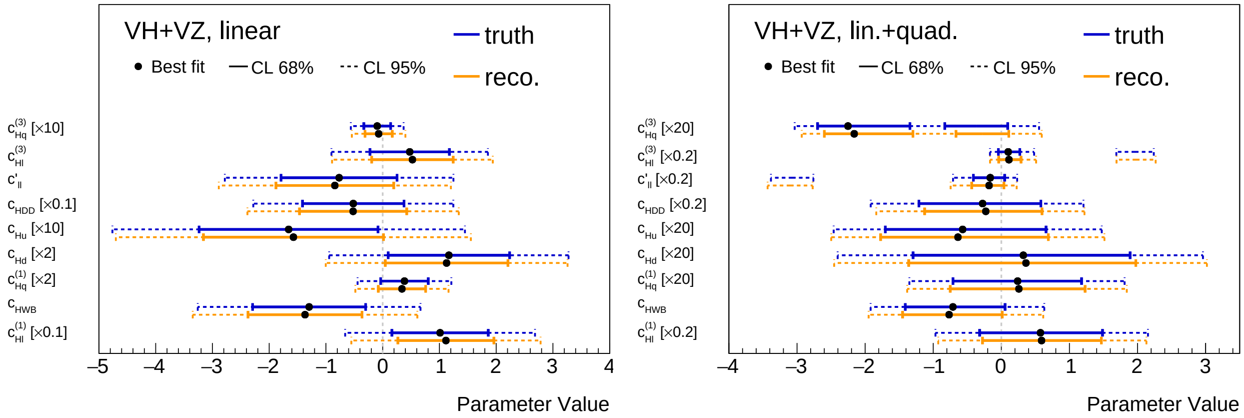

Figure 37: Comparison of χ^2 fit result for a linear (top) and linear + quadratic parametrisation (bottom) for $VH + VZ$ for the normalised cross-sections measured on truth and reconstruction level.

Linear parametrisation								
	Best fit c_i		68% confidence limit			95% confidence limit		
Name	Truth	Reco	Truth	Reco	RD	Truth	Reco	RD
$c_{Hq}^{(3)}$	-0.0096	-0.0071	[-0.033, 0.014]	[-0.031, 0.017]	-1.5 %	[-0.056, 0.037]	[-0.054, 0.040]	-1.6 %
$c_{Hl}^{(3)}$	0.48	0.52	[-0.22, 1.2]	[-0.19, 1.2]	-2.6 %	[-0.90, 1.9]	[-0.89, 1.9]	-2.7 %
c_{ll}'	-0.77	-0.84	[-1.8, 0.25]	[-1.9, 0.19]	-1.5 %	[-2.8, 1.2]	[-2.9, 1.2]	-1.5 %
c_{HDD}	-5	-5	[-14, 3.8]	[-15, 4.2]	-6 %	[-23, 12]	[-24, 13]	-6 %
c_{Hu}	-0.17	-0.16	[-0.32, -0.0082]	[-0.32, 0.0014]	-0.63 %	[-0.48, 0.15]	[-0.47, 0.16]	-0.71 %
c_{Hd}	0.58	0.56	[0.048, 1.1]	[0.023, 1.1]	-1.0 %	[-0.47, 1.6]	[-0.50, 1.6]	-1.0 %
$c_{Hq}^{(1)}$	0.19	0.17	[-0.018, 0.40]	[-0.039, 0.38]	0.57 %	[-0.22, 0.61]	[-0.24, 0.58]	0.63 %
c_{HWB}	-1.3	-1.4	[-2.3, -0.30]	[-2.4, -0.36]	-0.91 %	[-3.3, 0.67]	[-3.3, 0.61]	-0.82 %
$c_{Hl}^{(1)}$	10	11	[1.6, 19]	[2.7, 20]	0.32 %	[-7, 27]	[-6, 28]	0.33 %

Linear + quadratic parametrisation								
	Best fit c_i		68% confidence limit			95% confidence limit		
Name	Truth	Reco	Truth	Reco	RD	Truth	Reco	RD
$c_{Hq}^{(3)}$	-0.11	-0.11	[-0.13, -0.067] ∪ [-0.042, 0.0047]	[-0.13, -0.065] ∪ [-0.033, 0.0055]	9 %	[-0.15, 0.028]	[-0.15, 0.030]	1.8 %
$c_{Hl}^{(3)}$	0.51	0.56	[-0.22, 1.4]	[-0.19, 1.4]	-3.9 %	[-0.84, 2.4] ∪ [8, 11]	[-0.83, 2.6] ∪ [8 , 11]	-4.4 %
c_{ll}'	-0.81	-0.90	[-2.1, 0.25]	[-2.2, 0.19]	-2.8 %	[-17, -14] ∪ [-3.5, 1.2]	[-17, -14] ∪ [-3.7 , 1.1]	-4.2 %
c_{HDD}	-1.4	-1.1	[-6, 2.9]	[-6, 3.0]	3.8 %	[-10, 6]	[-9, 6]	2.2 %
c_{Hu}	-0.028	-0.032	[-0.085, 0.033]	[-0.089, 0.035]	-4.4 %	[-0.12, 0.074]	[-0.12, 0.076]	-1.9 %
c_{Hd}	0.016	0.018	[-0.065, 0.095]	[-0.068, 0.099]	-4.6 %	[-0.12, 0.15]	[-0.12, 0.15]	-2.0 %
$c_{Hq}^{(1)}$	0.012	0.013	[-0.036, 0.059]	[-0.038, 0.062]	-4.9 %	[-0.068, 0.091]	[-0.069, 0.092]	-2.0 %
c_{HWB}	-0.71	-0.77	[-1.4, 0.055]	[-1.5, 0.013]	0.11 %	[-1.9, 0.63]	[-1.9, 0.62]	-0.53 %
$c_{Hl}^{(1)}$	2.9	3.0	[-1.6, 7]	[-1.4, 7]	3.3 %	[-4.8, 11]	[-4.6, 11]	2.1 %

Table 13: Comparison of the χ^2-fit results for the linear + quadratic parametrisation model for $VH + VZ$ based on normalised cross sections measured on truth and reconstruction level. The relative difference (RD) of the size of the CLs is defined as $\text{RD} = 1 - \frac{\text{reco}}{\text{truth}}$.

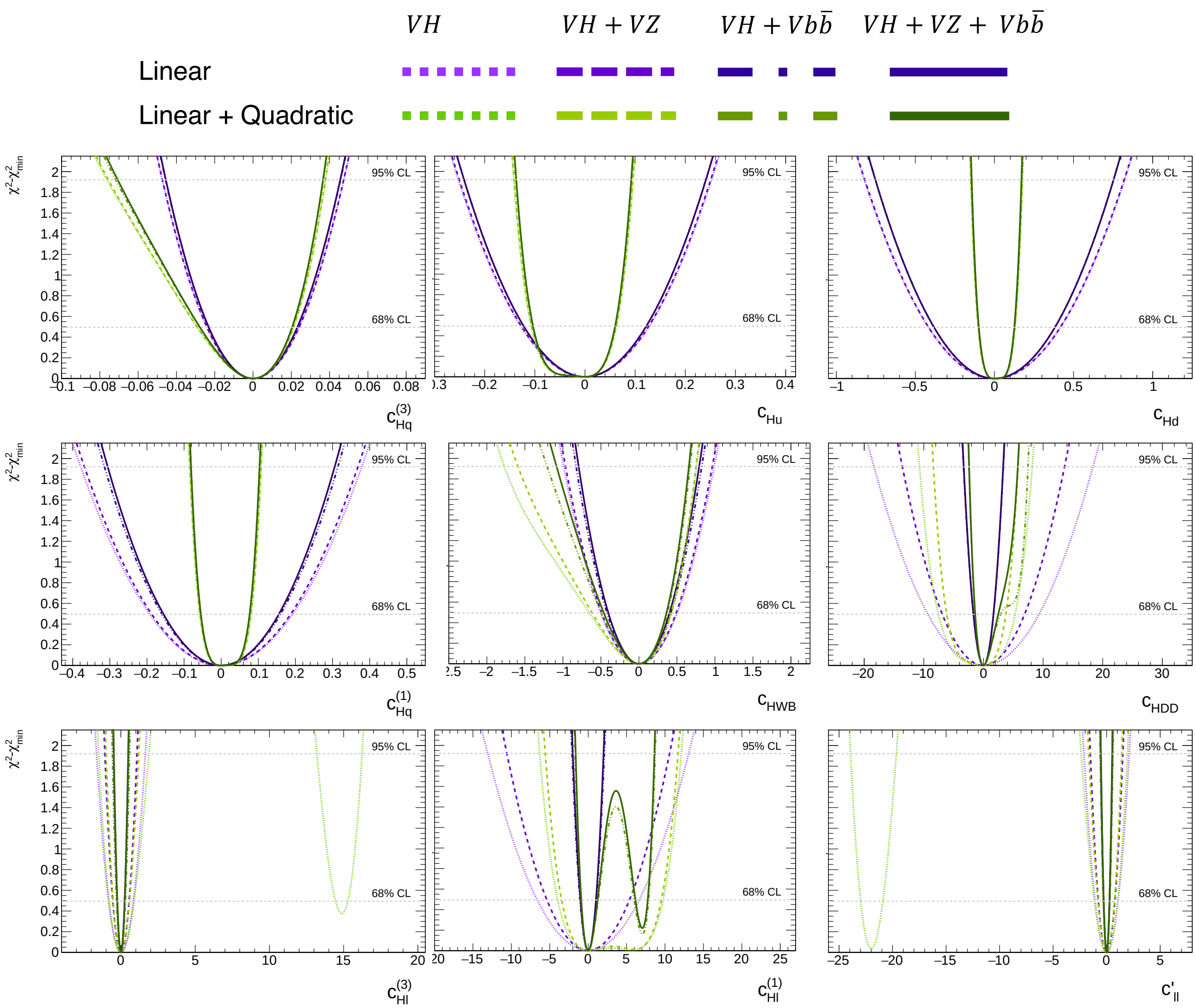

Figure 38: Comparison of the fits to VH vs. VH+VZ, VH+V+$b\bar{b}$, VH+VZ+V+$b\bar{b}$ for the linear and linear + quadratic parametrisation model for Asimov data.

Linear parametrisation							
	Expected 68% confidence intervals				Relative difference wrt. VH		
Name	VH	VH+VZ	VH+V+$b\bar{b}$	VH+VZ+V+$b\bar{b}$	VH+VZ	VH+V+$b\bar{b}$	VH+VZ+V+$b\bar{b}$
$c_{Hq}^{(3)}$	[-0.024, 0.024]	[-0.024, 0.024]	[-0.023, 0.023]	[-0.023, 0.023]	0.12 %	4.0 %	3.9 %
$c_{Hq}^{(1)}$	[-0.19, 0.19]	[-0.19, 0.19]	[-0.16, 0.16]	[-0.16, 0.16]	2.8 %	17 %	19 %
c_{Hu}	[-0.13, 0.13]	[-0.13, 0.13]	[-0.12, 0.12]	[-0.12, 0.12]	0.62 %	4.7 %	4.6 %
c_{Hd}	[-0.42, 0.42]	[-0.42, 0.42]	[-0.38, 0.38]	[-0.38, 0.38]	0.38 %	9 %	8 %
c_{HWB}	[-0.50, 0.50]	[-0.49, 0.49]	[-0.42, 0.42]	[-0.40, 0.40]	2.1 %	16 %	20 %
c_{HDD}	[-9, 9]	[-7, 7]	[-1.7, 1.7]	[-1.7, 1.7]	26 %	82 %	82 %
$c_{Hl}^{(3)}$	[-0.83, 0.83]	[-0.55, 0.55]	[-0.29, 0.29]	[-0.25, 0.25]	34 %	66 %	70 %
$c_{Hl}^{(1)}$	[-7, 7]	[-5, 5]	[-1.1, 1.1]	[-1.0, 1.0]	19 %	84 %	85 %
c'_{ll}	[-1.1, 1.1]	[-0.77, 0.77]	[-0.30, 0.30]	[-0.27, 0.27]	28 %	72 %	75 %
	Expected 95% confidence intervals				Relative difference wrt. VH		
Name	VH	VH+VZ	VH+V+$b\bar{b}$	VH+VZ+V+$b\bar{b}$	VH+VZ	VH+V+$b\bar{b}$	VH+VZ+V+$b\bar{b}$
$c_{Hq}^{(3)}$	[-0.047, 0.047]	[-0.047, 0.047]	[-0.046, 0.046]	[-0.046, 0.046]	0.13 %	3.6 %	3.9 %
$c_{Hq}^{(1)}$	[-0.38, 0.38]	[-0.37, 0.37]	[-0.31, 0.31]	[-0.31, 0.31]	2.7 %	17 %	19 %
c_{Hu}	[-0.25, 0.25]	[-0.25, 0.25]	[-0.24, 0.24]	[-0.24, 0.24]	0.79 %	4.6 %	4.5 %
c_{Hd}	[-0.82, 0.82]	[-0.82, 0.82]	[-0.75, 0.75]	[-0.75, 0.75]	0.39 %	9 %	9 %
c_{HWB}	[-0.99, 0.99]	[-0.96, 0.97]	[-0.83, 0.83]	[-0.79, 0.79]	2.4 %	16 %	20 %
c_{HDD}	[-18, 18]	[-14, 14]	[-3.3, 3.3]	[-3.3, 3.3]	26 %	82 %	82 %
$c_{Hl}^{(3)}$	[-1.6, 1.6]	[-1.1, 1.1]	[-0.57, 0.57]	[-0.49, 0.49]	34 %	66 %	70 %
$c_{Hl}^{(1)}$	[-13, 13]	[-11, 11]	[-2.1, 2.1]	[-2.0, 2.0]	19 %	84 %	85 %
c'_{ll}	[-2.1, 2.1]	[-1.5, 1.5]	[-0.58, 0.58]	[-0.53, 0.53]	28 %	72 %	75 %

Table 14: Comparison of the expected χ^2-fit results for the linear parametrisation model for VH and VH+VZ and VH+VZ+V+$b\bar{b}$ based on Asimov data.

Linear + quadratic parametrisation							
	Expected 68% confidence limits				Relative difference wrt. VH		
Name	VH	$VH+VZ$	$VH+V{+}b\bar{b}$	$VH+VZ+V{+}b\bar{b}$	$VH+VZ$	$VH+V{+}b\bar{b}$	$VH+VZ+V{+}b\bar{b}$
$c_{Hq}^{(3)}$	[-0.029, 0.021]	[-0.029, 0.021]	[-0.028, 0.021]	[-0.028, 0.020]	0.24 %	3.8 %	4.3 %
$c_{Hq}^{(1)}$	[-0.058, 0.080]	[-0.057, 0.080]	[-0.055, 0.077]	[-0.055, 0.077]	0.58 %	4.6 %	4.9 %
c_{Hu}	[-0.11, 0.063]	[-0.11, 0.062]	[-0.10, 0.060]	[-0.10, 0.060]	0.45 %	3.3 %	3.5 %
c_{Hd}	[-0.10, 0.13]	[-0.10, 0.13]	[-0.099, 0.13]	[-0.099, 0.13]	0.69 %	3.8 %	3.7 %
c_{HWB}	[-0.65, 0.43]	[-0.61, 0.42]	[-0.49, 0.37]	[-0.46, 0.36]	4.0 %	20 %	24 %
c_{HDD}	[-8, 5]	[-6, 3.8]	[-1.4, 2.9]	[-1.4, 2.5]	23 %	67 %	70 %
$c_{Hl}^{(3)}$	[-0.79 , 0.89] ∪ [14 , 15]	[-0.53, 0.57]	[-0.28, 0.29]	[-0.25, 0.25]	56 %	77 %	80 %
$c_{Hl}^{(1)}$	[-4.0, 10]	[-3.5, 10]	[-0.94 , 1.3] ∪ [6 , 8]	[-0.90 , 1.2] ∪ [6 , 8]	5 %	70 %	73 %
c'_{ll}	[-23 , -21] ∪ [-1.1 , 1.0]	[-0.80, 0.74]	[-0.30, 0.29]	[-0.27, 0.27]	64 %	86 %	87 %
	Expected 95% confidence limits				Relative difference wrt. VH		
Name	VH	$VH+VZ$	$VH+V{+}b\bar{b}$	$VH+VZ+V{+}b\bar{b}$	$VH+VZ$	$VH+Vb\bar{b}$	$VH+VZ+V{+}b\bar{b}$
$c_{Hq}^{(3)}$	[-0.076, 0.038]	[-0.076, 0.038]	[-0.072, 0.037]	[-0.071, 0.037]	0.60 %	5.0 %	6 %
$c_{Hq}^{(1)}$	[-0.085, 0.11]	[-0.084, 0.11]	[-0.081, 0.10]	[-0.081, 0.10]	0.58 %	4.1 %	4.3 %
c_{Hu}	[-0.14, 0.096]	[-0.14, 0.095]	[-0.14, 0.092]	[-0.14, 0.092]	0.57 %	3.7 %	3.7 %
c_{Hd}	[-0.15, 0.18]	[-0.15, 0.18]	[-0.14, 0.17]	[-0.14, 0.17]	0.54 %	3.6 %	3.7 %
c_{HWB}	[-1.8, 0.76]	[-1.6, 0.75]	[-1.2, 0.67]	[-1.1, 0.66]	7 %	26 %	31 %
c_{HDD}	[-11, 8]	[-8, 6]	[-2.4, 7]	[-2.4, 6]	25 %	48 %	57 %
$c_{Hl}^{(3)}$	[-1.5 , 1.9] ∪ [13 , 16]	[-1.00, 1.2]	[-0.55, 0.58]	[-0.48, 0.50]	66 %	82 %	85 %
$c_{Hl}^{(1)}$	[-6, 12]	[-6, 12]	[-1.7, 9]	[-1.6, 9]	6 %	43 %	44 %
c'_{ll}	[-24 , -20] ∪ [-2.4 , 1.9]	[-1.7, 1.4]	[-0.60, 0.57]	[-0.55, 0.53]	64 %	86 %	88 %

Table 15: Comparison of the expected χ^2-fit results for the linear + quadratic parametrisation model for VH and $VH{+}VZ$ and $VH{+}VZ{+}V{+}b\bar{b}$ based on Asimov data.

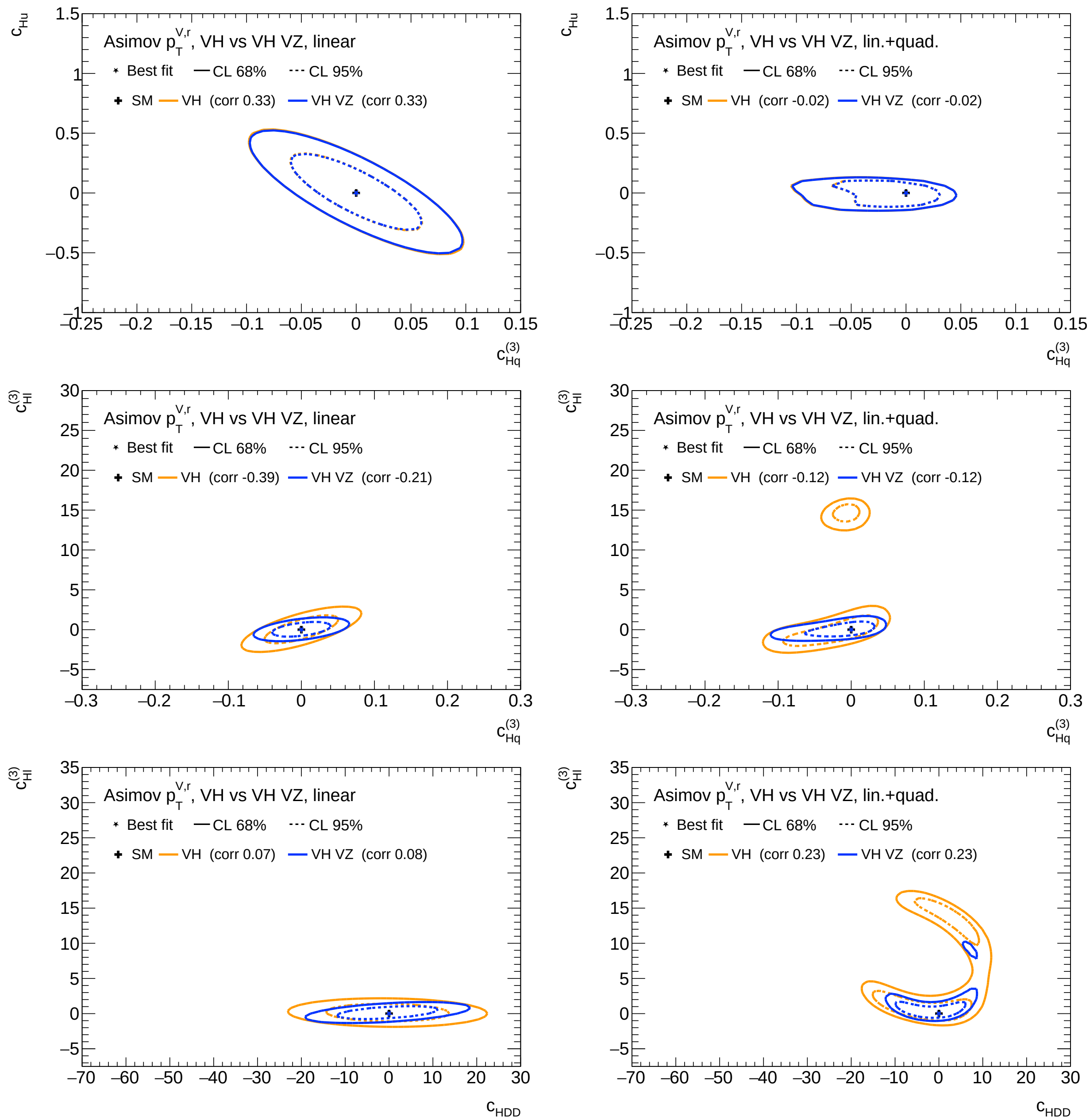

Figure 39: 68% and 95% CLs for the simultaneous fit of two operators at a time for VH and $VH{+}VZ$ for the linear (left) and linear + quadratic (right) parametrisation model based on Asimov data on reconstruction level. The axes are the same for the same operator pair (same row).

Acknowledgements

This thesis would have not been possible if not for the help and support of many fantastic colleagues. I am very excited to continue to collaborate with many of you in the coming years!
First of all, I would like to express my deepest gratitude to Tristan for introducing me to the $VH, H\to b\bar{b}$ analysis and its SMEFT interpretation, and for his guidance through my research and my grant application.
I would like to thank Flavia for igniting my curiosity for new physics beyond the Standard Model in her lecture and for kindly agreeing to be my second examiner.
Next, I would like to thank Geoffrey for his supervision of my daily work. We enjoyed many great discussions, always with the next step and the overarching picture in mind.
I am very grateful for Volkert van der Willingen's support that allowed me to spend several months at CERN during the restart of the LHC, which is truly the most exciting time for a particle physics student, and to contribute to the safety of the ATLAS detector.
Brian, thank you for all your fantastic help with the EFT framework and exceptional knowledge of the $VH, H\to b\bar{b}$ analysis and physics in general. It is a true pleasure not only working, but also skiing with you!
I am also beyond grateful to Carlos. You sparked my fascination for particle physics back in 2016, especially as it pertains to the technical side of ATLAS. Thank you so much for your mentorship and supervision far beyond the daily work!
Thank you Hannah and Jordy for sharing insightful discussions regarding my research and my thesis.
I was very lucky to write my master thesis as member of the fantastic Nikhef ATLAS group. Thank you for all the fun we shared!
Once at CERN, I was welcomed by a great technical operation and safety team. I would like to especially thank Ignacio and Gustavo for their help with the Expert system and Nico for his help with the electronics and the assembly of the new ventilation panel.
Last but not least, thank you, Carlos, Valerio, Wouter, Brian and Tristan for your fantastic support during my PhD application process.